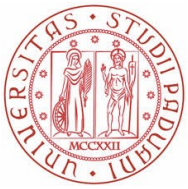

UNIVERSITÀ DEGLI STUDI DI PADOVA

DIPARTIMENTO DI SCIENZE CHIMICHE

CORSO DI LAUREA MAGISTRALE IN CHIMICA

TESI DI LAUREA MAGISTRALE

Polymer brush-supported photoredox catalysis

Relatore: Prof. Luca Dell'Amico

Correlatore: Prof. Edmondo Maria Benetti

Controrelatore: Prof.ssa Marilena Di Valentin

Laureanda: Elena Avanzini

ANNO ACCADEMICO 2023/2024

Contents

Summary of the project

Recently, organic compounds that show thermally activated delayed fluorescence (TADF) have been increasingly applied as photocatalysts. Despite their advantages, challenges such as product contamination and the disposal of photocatalysts pose significant limitations in homogeneous catalytic systems. To address these issues, this project focuses on developing photocatalytic systems supported by polymer brush-functionalized silica micro- or nanoparticles. This approach facilitates the efficient recovery and recycling of the photocatalysts through straightforward centrifugation or separation methods. By integrating polymeric substrates with small photocatalysts, the project aims to create functional materials that combine the advantages of both homogeneous and heterogeneous photocatalysis.

The first part of the project focused on the design, synthesis, and characterisation of a photocatalyst that can be incorporated within a poly(acrylate) through controlled radical (co)polymerization. This relies on the modification of a cyanoarene-based core, using 1,2,3,5-tetrakis(carbazol-9-yl)-4,6-dicyanobenzene (4CzIPN) and an acrylate function yielding 3CzIPN-A, a catalytically active co-monomer. Activators regenerated by electron transfer atom transfer radical polymerization (ARGET ATRP)—namely a controlled radical polymerization technique—provided the free copolymer in solution.
The ability of the copolymer p(OEGA-*co*-3czIPN-A) of catalysing photoreactions was demonstrated with high yields (~80%) by testing a Giese-type radical addition (radical decarboxylation and addition to a Michael acceptor) irradiating with a blue light (λ_{max}= 427 nm) for 3.5h. The polymer showed a good separation from the reaction mixture through precipitation; however it was not possible to reuse under these conditions. Hence, another photoreaction was tested (Povarov-type cyclization) showing, with a yield around 40%, a good recyclability for several cycles.

The last part of the project involved the synthesis of core-copolymer shell particles exploiting surface-initiated ARGET ATRP. Core-shell particles with the photocatalyst integrated in the brush-shell were obtained. The latter were just tested in a Giese-type reaction showing an easy separation at the end of the reaction through simple centrifugation, providing a yield of 30% of the desired product.

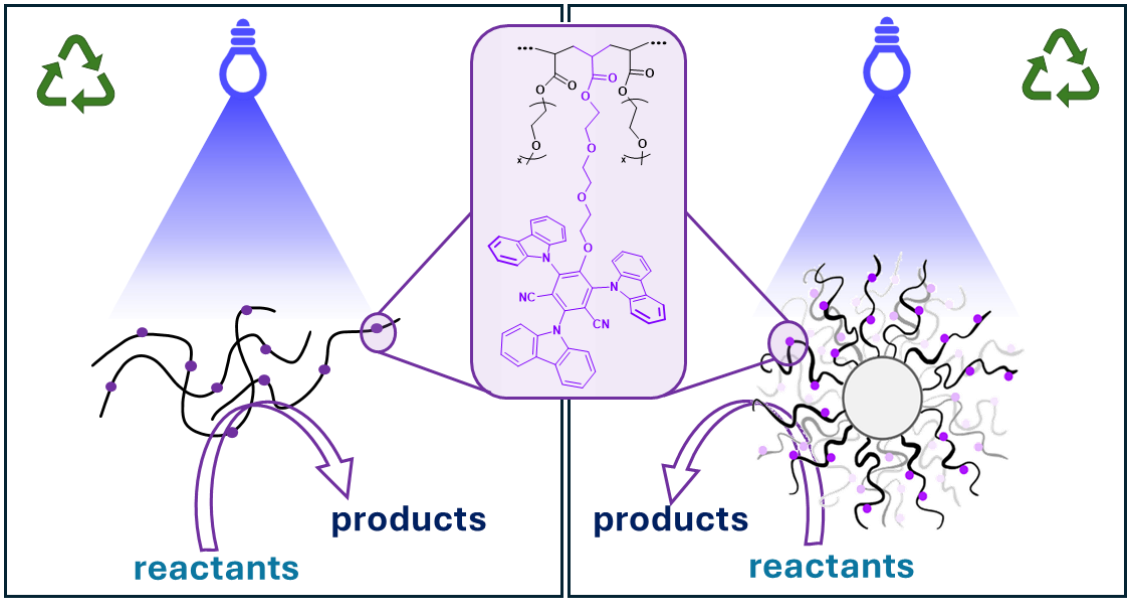

***Figure 1**: On the left the copolymer p(OEGA-co-3CzIPN-A) is represented in solution while on the left, the same copolymer constitute the shell of a silica particle. The picture represents the two main ideas behind the project. First testing the photoactive copolymer in photoreaction and try its recyclability and second translate this condition using a more complicated system where the polymer is grafted from a spherical surface.*

Riassunto del progetto

I composti organici che mostrano fluorescenza ritardata attivata termicamente (TADF) hanno trovato un crescente utilizzo come fotocatalizzatori. Nonostante i loro vantaggi, la contaminazione del prodotto e l'impossibilità di riutilizzo dei fotocatalizzatori pongono limitazioni significative nei sistemi catalitici omogenei. Per affrontare queste problematiche, questo progetto si concentra sullo sviluppo di sistemi fotocatalitici supportati da micro- o nanoparticelle di silice funzionalizzate con *polymer brushes*. Questo approccio facilita il recupero e il riciclo efficiente dei fotocatalizzatori attraverso semplici metodi di centrifugazione o separazione. Integrando substrati polimerici con fotocatalizzatori, il progetto mira a creare materiali funzionali che combinino i vantaggi della fotocatalisi omogenea ed eterogenea.

La prima parte del progetto si è concentrata sulla progettazione, sintesi e caratterizzazione di un fotocatalizzatore che potesse essere incorporato all'interno di un poli(acrilato) mediante (co)polimerizzazione radicalica controllata. Questo si basa sulla modifica della struttura del 1,2,3,5-tetrakis(carbazol-9-il)-4,6-dicianobenzene (4CzIPN) inserendo una catena terminata da una funzione acrilica polimerizzabile che porta alla formazione del 3CzIPN-A, un co-monomero cataliticamente attivo. L'*activator regenerated by electron transfer atom transfer radical polymerization* (ARGET ATRP) ha permesso di ottenere il copolimero in soluzione. La capacità del copolimero p(OEGA-*co*-3czIPN-A) di catalizzare fotoreazioni è stata dimostrata con alte rese (~80%) in un'addizione radicalica di tipo Giese (decarbossilazione radicalica e addizione a un accettore di Michael) irradiando con luce blu (λ_{max} = 427 nm) per 3.5 ore. Il polimero ha mostrato una buona separazione dalla miscela di reazione tramite precipitazione, tuttavia non è stato possibile riutilizzarlo in queste condizioni. Pertanto, è stata testata un'altra fotoreazione (ciclizzazione di tipo Povarov) mostrando, con una resa di circa il 40%, una buona riciclabilità per diversi cicli.

L'ultima parte del progetto ha riguardato l'ottimizzazione della modifica superficiale, sfruttando la *surface initiated* ARGET ATRP. Sono state ottenute particelle *core-shell* con il fotocatalizzatore integrato all'interno dello *shell* polimerico. Queste ultime sono state testate in una reazione di tipo Giese mostrando una facile separazione alla fine della reazione tramite semplice centrifugazione e ottenendo una resa del 30% del prodotto desiderato.

Abbreviations

S_0	Singlet ground state	**PCET**	Proton-coupled electron transfer
S_1	Singlet lower excited state	**SOMO**	Single occupied molecular orbital
T_1	Triplet lower excited state	**D**	Donor
IC	Internal conversion	**A**	Acceptor
ISC	Intersystem crossing	**sub**	Substrate
RISC	Reverse intersystem crossing	**DFT**	Density functional theory
TADF	Thermally activated delayed fluorescence	**4CzIPN**	1,2,3,5-Tetrakis(carbazol-9-yl)-4,6-dicyanobenzene
PC	photocatalyst	**CDCBs**	carbazolyl dicyanobenzenes
PC*	Excited photocatalyst	**CRP**	Controlled radical polymerization
CT	charge transfer	**σ**	grafting density
LE	Locally excited	***Đ***	Dispersity
HAT	Hydrogen atom transfer	**RDRP**	Reversible deactivation radical polymerization
EnT	Energy transfer	**SI-RDRP**	Surface initiated-reversible deactivation radical polymerization
ET	Electron transfer	**RAFT**	Reversible addition-fragmentation chain-transfer

ATRP	Atom transfer radical polymerization	**NMP**	Nitroxide mediated polymerization
SARA	Supplemental activation reducing agent	**PIMP**	Photoiniferter mediated polymerization
ARGET	Activator regenerated by electron transfer	**$Sn(EH)_2$ or $Sn(oct)_2$**	Tin(II) 2-ethylhexanoate
ICAR	Initiators for continuous activator regeneration	**SI-ATRP**	Surface initiated-atom transfer radical polymerization
CTA	Chain transfer agent	**NP**	Nanoparticle
L	Ligand	**IPN**	Isophthalonitrile
OEGA	(oligoethylene glycol) methyl ether acrylate	**SCE**	Saturated calomel electrode
3CzIPN-A	1,3,5-Trikis(carbazol-9-yl)-2 triethylenglycol acrylate-4,6 dicyanobenzene	**ACN**	acetonitrile
3CzIPN-TEG	1,3,5-Trikis(carbazol-9-yl)-2 hydroxy triethylenglycol-4,6 dicyanobenzene	**DMF**	Dimethyl formamide
3CzIPN-red	1,3,5-Trikis(carbazol-9-yl)-2 isobutyryl triethylenglycol-4,6 dicyanobenzene	**DMSO**	Dimethyl sulphoxide
TCSPC	Time correlated single proton counting	**EtOAc**	Ethyl acetate
MSC	Multi-channel scaling	**Et_2O**	Diethyl ether
τ_p	Lifetime of prompt fluorescence	**DCM**	Dichloromethane
τ_d	Lifetime of delayed fluorescence	**EtOH**	ethanol
EBiB	ethyl α-bromoisobutyrate	**APTES**	(3-aminopropyl) triethoxysilane

Me_6TREN	Tris[2-(dimethylamino)ethyl]amine	**TEA**	Triethyl amine
M_w	Weight average molecular weight	**SEM**	Scanning electron mycroscopy
M_n	Number average molecular weight	**TGA**	Thermogravimetric analysis
BiBB	α-bromoisobutyryl bromide	**GPC**	Gel permeation chromatography
TEM	Transmission electron microscopy	**STEM**	Scanning transmission electron microscopy
XAT	Halogen atom transfer	***S.I.***	Supporting information

1. Introduction

1.1. Photochemistry

Photochemistry is a sustainable approach that uses light to drive chemical reactions. Photocatalysis presents an alternative to traditional thermal catalysis providing new reaction pathways[1] (**Figure 1.1**) through the formation of reactive intermediates that cannot be achieved by thermal conditions.[2,3]

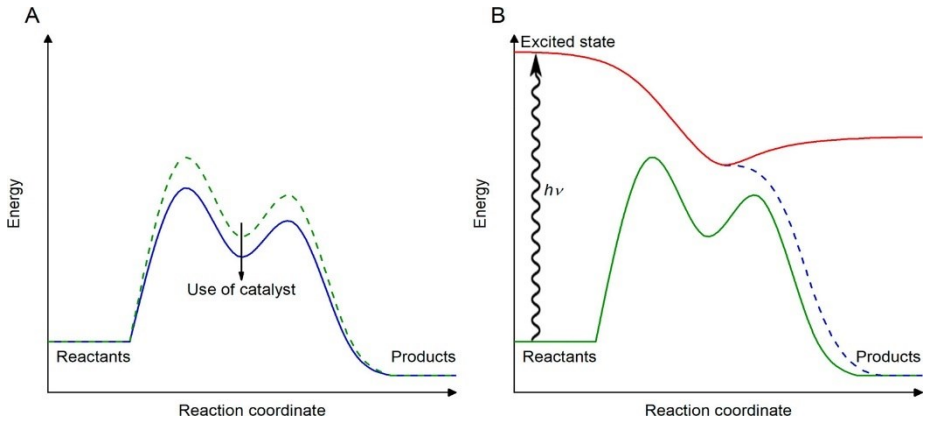

***Figure 1.1**: Thermal reaction vs photochemical reaction energy diagram. Reproduced from [1].*

Early papers on the use of light for chemical reaction date back to the beginning of the 20th century. Particularly, 1908 is considered a revolutionary year for photochemistry mainly thanks to the work of Giacomo Ciamician.[4] Ciamician, conducted extensive experiments that demonstrated the power of light in driving chemical reactions, independent of heat. His research documented a variety of light-induced reactions, establishing that these processes were initiated solely by light energy rather than thermal energy. [5] His work not only advanced scientific knowledge but also paved the way for future developments in the use of light in chemical synthesis and catalysis.

Some years later Neiber introduced the term *photocatalysis* reporting the bleaching of Prussian blue in the presence of ZnO under light irradiation.[6]

Looking at the number of publications for the keyword “photocatalysis” on Elsevier Scopus (**Figure 1.2**) it is clear the exponential growth of this field in the last two decades.

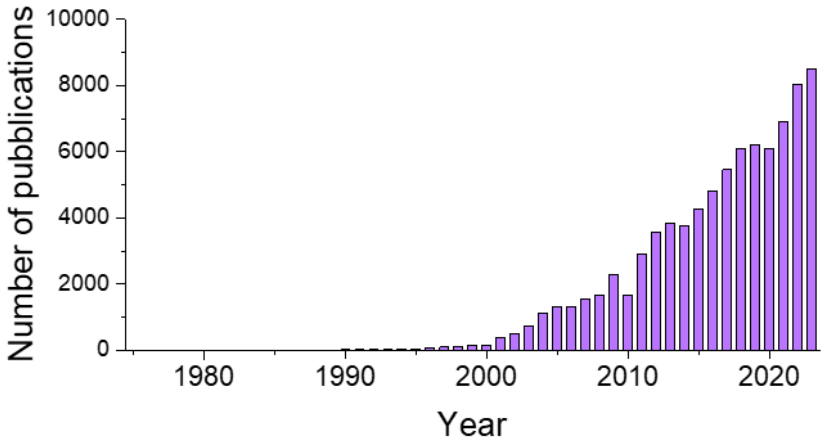

***Figure 1.2**: Number of publications between 1975 and 2023. Search term “photocatalysis” on Elsevier Scopus.*

The growing interest in photocatalysis is driven by its potential to shorten synthetic processes under mild conditions while facilitating the formation of complex or highly functionalized structures through photochemical steps. These transformations provide new possibilities for accessing product families or libraries that are difficult or impossible to obtain otherwise.[7–9]

1.1.1 General concepts of photophysics

When a compound in its ground state S_0 absorbs light, it reaches one of the excited singlet states S_n. How it is depicted in the Jablonski diagram (**Figure 1.3**) the molecule can undergo different decays to restore its ground state. The fastest process at this point is the internal relaxation (IC) that generally occurs in a picoseconds scale and brings the molecule to the lowest vibrational state S_1. Hence, one can consider that the relaxion to the ground state will always happen from S_1 that will be the only populated excited state after the fast IC, according to Kasha’s rule.[10]

The formation of the excited state depends on the spin conservation and the initial and final state of the vibrational and electronic wavefunctions following the Frank-Condon principle. According to IUPAC-Compendium of Chemical Terminology,

2nd Edition (1997), *the Franck–Condon principle is the approximation that an electronic transition is most likely to occur without changes in the positions of the nuclei in the molecular entity and its environment*. In other words, the probability of the electronic transition is linked to the overlap between the vibrational wavefunctions of the ground and excited-state defined by the Franck-Condon factor F:[11]

$$F = \left|\langle \Psi_{vibr,f} | \Psi_{vibr,i} \rangle\right|^2$$

Where $\Psi_{vibr,f}$ and $\Psi_{vibr,i}$ are respectively the excited state and ground state vibrational wavefunctions.

The compound in its excited state S_1 can go back to the ground state through different pathways, as shown in the in the Jablonski diagram in **Figure 1.3**.

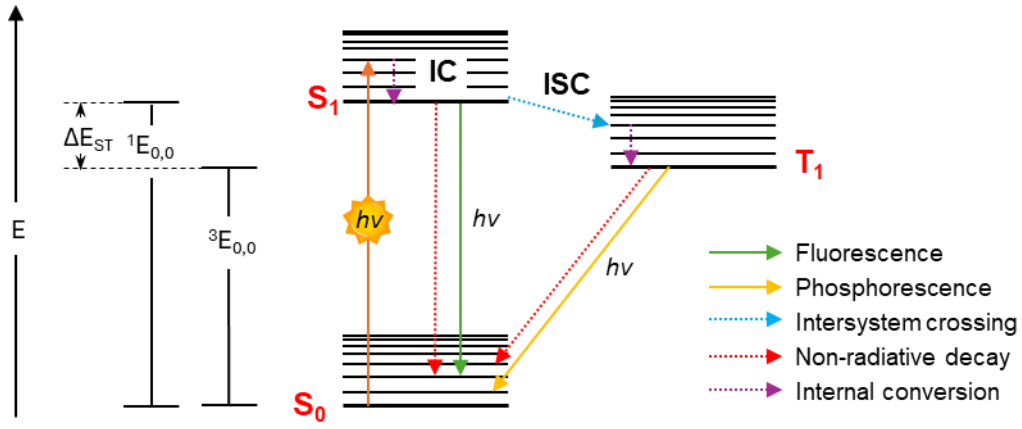

***Figure 1.3**: Jablonski diagram.*

It can experience the non-radiative decay or the radiative one: fluorescence. Nevertheless, one competitive pathway is the relaxation to the triplet T_1 (lower energy) through intersystem crossing (ISC). This process involves changing the spin of one electron and is therefore a spin forbidden transition. However, it is possible when spin-orbit coupling (SOC)[12] occurs and a change in the total spin angular momentum $\vec{S}$ is compensated by a change in the total orbital angular momentum $\vec{L}$.

1.1.2 Direct photochemistry and photocatalysis

Photochemistry can be divided into two main fields: direct photochemistry and photocatalysis. In direct photochemistry one of the reactants absorbs light and consequently it is directly excited.[13,14] In contrast, in photocatalysis when a molecule cannot directly absorb light, a photocatalyst serves as a crucial intermediary. The photocatalyst absorbs light energy and transitions to an excited state, where it gains the ability to transfer energy or electrons to the reactants. These processes enable the reactants to reach the necessary activation state, driving the chemical reaction forward even under milder conditions. The earliest examples of photochemical transformations involved the direct irradiation of substrates such as the *syn–anti* isomerization of oximes reported by Ciamician and Silber (**Scheme 1.1**).[5]

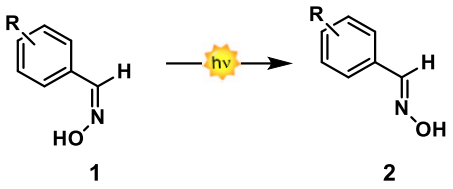

1 2

***Scheme 1.1**: Photoinduced syn-anti isomerization ox oximes.*

Another important contribution at the beginning of direct photochemistry is from Emanuele Paternò e George Büchi with the Paternò-Büchi reaction[15]. This reaction, is a [2+2]-photocycloaddition between an alkene (**4**) and the excited state of a carbonyl compound (**3**) to give the corresponding oxetane **5** (**Scheme 1.2**). Mechanistic studies of the reaction have revealed that once the carbonyl in the ground state has been photoexcited, either a singlet or triplet state may be formed. When the electronic transition occurs ($n \rightarrow \pi^*$ or $\pi \rightarrow \pi^*$) a diradical intermediate is formed leading to the formation of the cyclic compound through σ-bonds formation. Finally, the breaking of the new σ-bonds requires more energy than the first step so that the reverse reaction is not possible using same light frequency.

This reaction was firstly reported in 1909, but it is still used nowadays.[16]

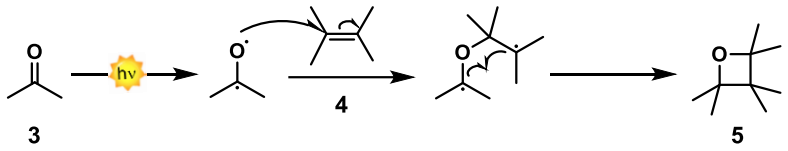

***Scheme 1.2**: Paternò- Büchi reaction mechanism.*

The term photocatalysis was firstly introduced in 1912, nevertheless it saw its real development from 2008 thanks to the works of MacMillan, Yoon and Stephenson who demonstrated the capability of photoactive organometallic compounds to mediate organic transformations.[17–20]

At the beginning catalysts were mainly metal-based exploiting Ruthenium, Iridium and other rare earths metals which have proven to be suitable photocatalysts for a lot of transformations.[21] However, they present some drawbacks. They are made from scarce and expensive elements that often require not sustainable and energy-intensive extraction processes. They are generally not biocompatible, and toxicity is often a concern while their synthesis and disposal are associated with significant environmental damage and pollution. In contrast to the latter, visible light organo-photoredox catalysts have recently demonstrated their enormous potential for enabling challenging chemical reactions while being a cheaper and greener alternative to transition metal-based catalysts.[22] Moreover, they offer greater chemical tunability. Their structures can be easily modified to adjust properties like light absorption, redox potential, and solubility, allowing for precise control over catalytic activity. The use of organic molecules that feature all the advantages of well-established metal-based PCs represents a decisive advance towards sustainability and cost efficiency in photocatalysis. Notable examples include fluorescein,[23] eosin Y,[24] acridinium salts,[25,26] rose Bengal[27] and many others.

These two classes of catalysts can also differ from each other by the “type of excited state” that can be divided between charge transfer (CT) and locally excited (LE). In the CT mechanism the electron density is displaced from one part of the molecule (donor moiety) to another (acceptor moiety) and it is the typical excited state of metal-based photocatalysts. Purely organic compounds undergo both mechanisms, where in the LE the electron density is retained in the same

area of the molecule during the transition π→π* (better orbital overlapping).[28] LE states are typically shorter-lived than CT states according to Fermi's golden rule [29] stating that the transition's rate depends upon the strength of the coupling between the initial and final state and upon the density of the final states of the system. Specifically, the relaxation rate is given by the following formula:

$$W_{fi} = \frac{2\pi}{\hbar} | \langle f | \hat{\mathrm{H}}_{int} | i \rangle |^2 \rho(E_f)$$

Where:

- $\hbar$ is the reduced Planck constant,
- *f* and *i* are the wavefunctions of the initial and final sates,
- $\hat{\mathrm{H}}_{int}$ is the interaction Hamiltonian responsible for the transition,
- $| \langle f | \hat{\mathrm{H}}_{int} | i \rangle |$ is the matrix element representing the overlap between the initial and final states,
- $\rho(E_f)$ is the density of final states available at energy E_f.

Since in LE states the excitation is localized within a specific part of the molecule the matrix element tends to be large because the transition involves a localized change, making it easier for the molecule to relax back to the ground state. In CT states, the excitation involves a significant separation of charge, where an electron is transferred from one part of the molecule to another making the matrix element smaller. It results in a longer lifetime of the CT excited state since its decay turns out to be slower.

1.1.3 Mechanistic pathways in photocatalysis

It is possible to individuate five main different mechanisms: hydrogen atom transfer (HAT) and halogen-atom transfer (XAT), energy transfer (EnT), electron transfer (ET) and proton-coupled electron transfer (PCET). [30]

In the HAT process the activation of the substate pass through the transfer of a hydrogen atom $H^{\bullet}$. The excited PC* abstracts a hydrogen atom from the

substrate. The protonated form of the PC (PC-H) can consequently donate the H• to another substrate closing the photocatalytic cycle (**Scheme 1.3**). [31]

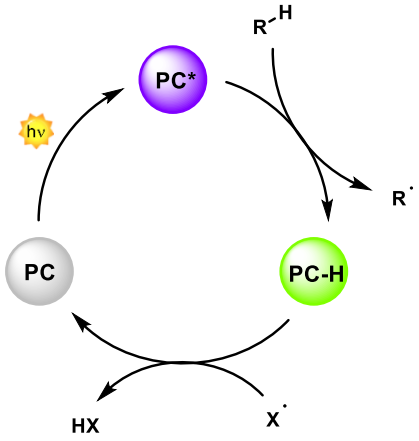

***Scheme 1.3**: Hydrogen atom transfer mechanism.*

If the starting organic substrate is a halogenated compound (R-X) and the interaction with the PC* brings to the cleave of the C-X bond, the process is referred to as the halogen atom transfer (XAT) mechanism (**Scheme 1.4**). In this mechanism, a carbon-centered radical is formed (R•) and the photocatalyst forms a PC-X species, which can then transfer the halogen atom (X•) to another substrate, thereby regenerating the photocatalyst. Halogen-atom transfer (XAT) is a fundamental step in radical reactions to generate carbon-based radical intermediates from alkyl and aryl halides efficiently.[32]

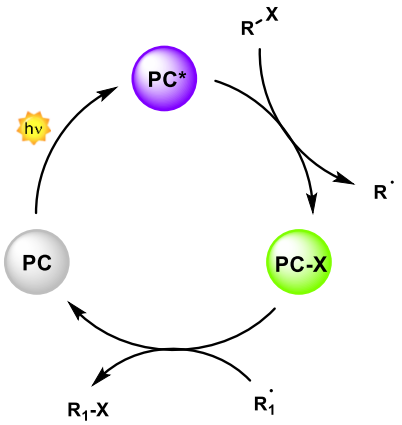

***Scheme 1.4:** Halogen atom transfer mechanism.*

The EnT generally works from the triplet excited state. Once the catalyst reaches the excited S_1 state, it undergoes ISC accessing the triplet T_1 from where it

transfers energy to the substrate R that reaches its triplet excited state (**Scheme 1.5**). This process is possible if the triplet energy of the compound involved in the reaction is lower than T^1 energy of the photocatalyst.[33]

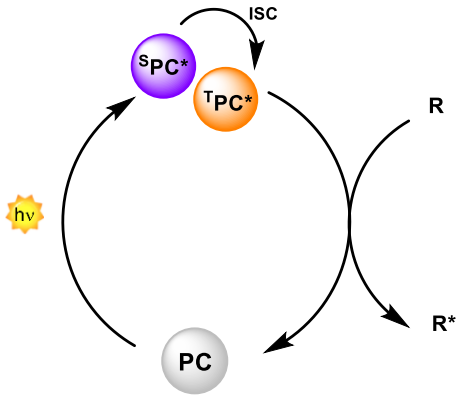

***Scheme 1.5**: Energy transfer mechanism.*

It is possible to distinguish two different EnT processes: Förster resonance energy transfer (FRET)[34] or Dexter exchange.[35] FRET is a non-radiative energy transfer process that occurs via dipole-dipole interactions between molecules, leading to the transfer of energy from the donor's excited state to the acceptor. [36] Similarly, Dexter exchange is a non-radiative process, in this case the process involves a simultaneous intermolecular exchange of two electrons. The excited photocatalyst donates an electron to the LUMO of the substate, while simultaneously, the substrate donates an electron to the HOMO of the PC. This results in the substrate being excited, and the photocatalyst returning to its ground state.

The ET process in most cases works directly from the excited singlet state. In this mechanism the PC in the excited state is more reductant and more oxidating. Indeed, when an electron is excited from the highest occupied molecular orbital (HOMO) to the lowest unoccupied molecular orbital (LUMO) brings to the formation of two single occupied molecular orbitals (SOMO, **Figure 1.4**). The lowest in energy is more stabilized with respect to the HOMO of the ground state form, resulting in a higher oxidative power of the PC*, on the contrary, the highest SOMO is more destabilized with respect to the LUMO of the ground state, resulting in an enhanced reductive power of the PC*.

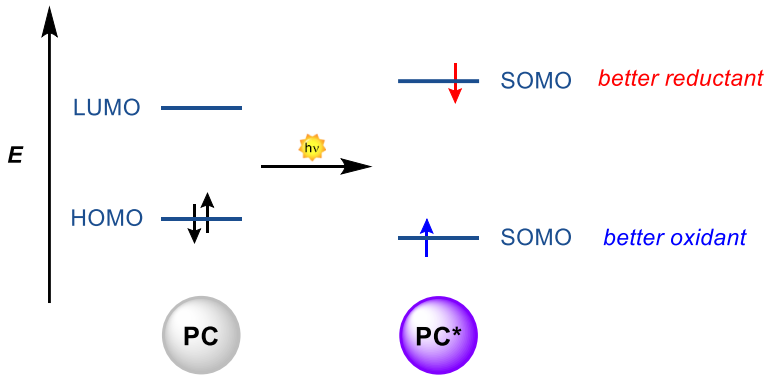

***Figure 1.4**: Energy level comparison between ground state and excited state of a PC.*

From this situation the compound can both donate or accept an electron to or from an organic substrate giving access to two different pathways: the reductive quenching and the oxidative one depending on the oxidation state of the catalyst (**Scheme 1.6**).[37]

Reductive quenching: the excited photocatalyst in the presence of an electron rich donor (D) gets one electron forming the radical anion $PC^{\bullet -}$. At this point the ground state of the PC is restored thanks to the presence of an electron poor molecule (acceptor A). In this cycle the PC gets reduced promoting the oxidation of the substrate that generally represents the donor moiety.

Oxidative quenching: in this case the PC* donate an electron to the acceptor molecule A forming the radical cation $PC^{\bullet +}$. The ground state will be restored by a donor D. Inversely from the reductive quenching, the PC is here oxidated promoting the reduction of the substrate.

When the PC is back to its ground state it can be re-excited to PC* and starting a new catalytic cycle.

The pathway that occurs depends on the redox potentials of the PC* and the substrate.

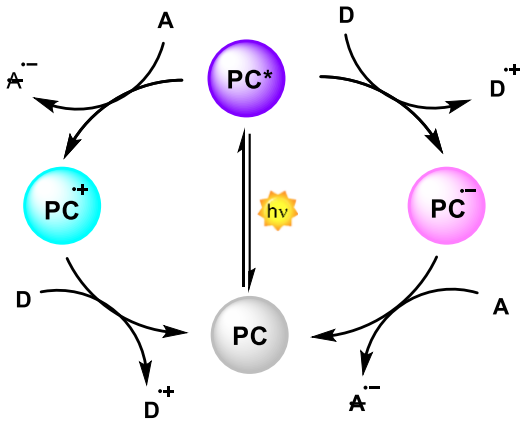

***Scheme 1.6**: Electron transfer mechanism.*

Finally, another mechanism that combines two of the previous ones, is the proton-coupled electron transfer (PCET). Here the PC* transfer both an electron and a hydrogen atom at the same time generating the radical species of the substrate. Also, in this case the oxidative and reductive quenching can be distinguished (**Scheme 1.7**).[38]

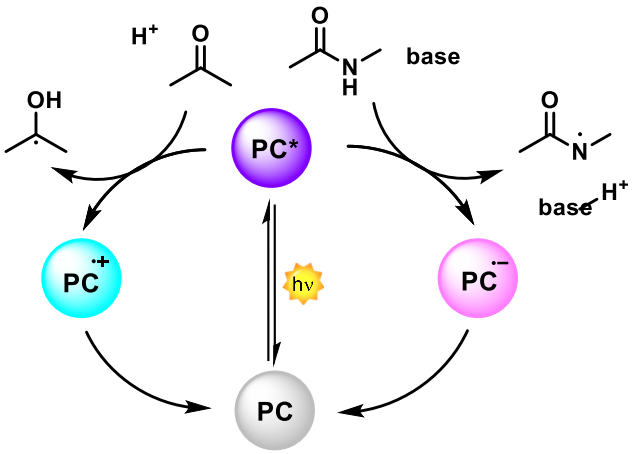

***Scheme 1.7**: Proton-coupled electron transfer mechanism.*

To determine whether PC* will react from the triplet state (primarily an energy transfer process) or the singlet state (primarily an electron transfer mechanism), several factors must be considered. Firstly, for energy transfer (EnT) to occur, the substrate must have a lower triplet energy compared to the photocatalyst. If both mechanisms are possible, the diffusion constant (k_{diff}) for the formation of the encounter complex (PC* + substrate) must be considered, as this is the first step in a photophysical process. According to the Jablonski diagram (**Figure 1.5**), if

the rate constant of the intersystem crossing process (k_{ISC}) is lower than k_{diff}, the singlet state (^{1}PC*) will form the complex. Conversely, if k_{ISC} is higher, the triplet state (^{3}PC*) will form the complex.

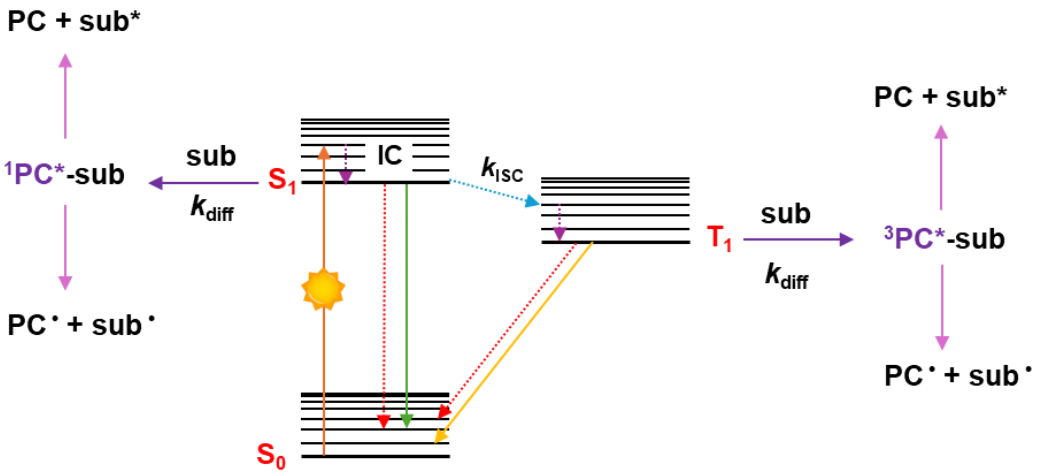

***Figure 1.5**: Jablonski diagram reporting the formation of the encounter complex between the excited state of the catalyst (PC*) and the substrate (sub).*

1.1.4 Thermally activated delayed fluorescence (TADF) compounds as bimodal photocatalysts

In recent years, organic molecules that show thermally activated delayed fluorescence (TADF), known as emitters in organic light emitting diodes (OLEDs), have found increasing use as photocatalysts.[39,40]

Recalling the Jablonski diagram (**Figure 1.3**), upon excitation, a molecule transitions to its S_1 state. From there, it can return to the ground state through various pathways, either non-radiatively or radiatively via fluorescence. Alternatively, the molecule may relax to the lower-energy triplet state (T_1) through intersystem crossing. For the photocatalyst before mentioned, such as acridinium salts, flavins, fluorescein etc. the S_1 state typically has a lifetime of a few nanoseconds at most before relaxing. If the S_1 lifetime is shorter than 1 ns, the molecule is generally ineffective as a photocatalyst, as it is likely to fluoresce before it can diffuse to the substrate. Conversely, a longer S_1 lifetime enhances the photocatalyst's efficiency.

A unique feature of TADF photocatalysts is their very long lifetime of the excited state. This is possible because S_1 and T_1 are really close in energy: the energy gap ΔE_{S1T1} is less than 0.3 eV. For this reason the triplet state is very high in

energy and once it gets populated, after the intersystem crossing, the compound doesn't phosphoresce because of a too big ΔE_{S0T1}. At this stage, a new process takes place: reverse intersystem crossing (RISC). This phenomenon extends the excited state lifetime of TADF catalysts to microseconds in the best cases. These prolonged excited state lifetimes enhance the efficiency of the photocatalysts by increasing the probability of interactions between the excited photocatalyst (PC*) and the reactant. ΔE_{S1T1} is the parameter to control to obtain a catalyst with this characteristic because is the one that governs the states' mixing. Indeed, it is directly proportional to the exchange integer (J) between S_1 and T_1:

$$\iint \Phi(r_1)\Psi(r_2)\left(\frac{e^2}{r_2 - r_1}\right)\Phi(r_2)\Psi(r_1)dr_1dr_2$$

Where $\Phi(\mathrm{r})$ and $\Psi(\mathrm{r})$ are the wavefunctions of HOMO and LUMO orbitals.

Briefly, the exchange integer depends on the overlap of the molecular frontier orbital involved in the transition $S_1 \rightarrow T_1$. Now it is clear that minimising the overlap between HOMO and LUMO we will observe a smaller J and, consequently, a smaller ΔE_{S1T1}.[41]

The strategy for the synthesis of TADF compounds involves creating spatially separated and electronically decoupled donor-acceptor structures, where the HOMO is localized on the donor unit and the LUMO on the acceptor unit. For instance, a widely studied TADF compound is 1,2,3,5-Tetrakis(carbazol-9-yl)-4,6-dicyanobenzene (4CzIPN, **6**).[42] The 4CzIPN belongs to the carbazolyl dicyanobenzene (CDCBs), namely, a derivative of cyanoarenes. The first testimony of this compounds used as photocatalysts date back to 2016 in a paper by Luo and Zhang[43] while they were already described as TADF compounds since 2012 by Adachi and coworkers.[44] 4CzIPN is composed of an electron poor aromatic core (acceptor part) and four carbazoles that represents the electron rich part of the molecule (donator moieties). As shown from the DFT calculations in **Figure 1.6** the HOMO is localized on the substituents while the LUMO on the centre of the molecule and steric hindrance generally intensifies this separation. In other words, the same compound can act both as oxidating and reducing agent

acting as a *bimodal photocatalysts* and this behaviour is not common among organic photocatalysis.[45]

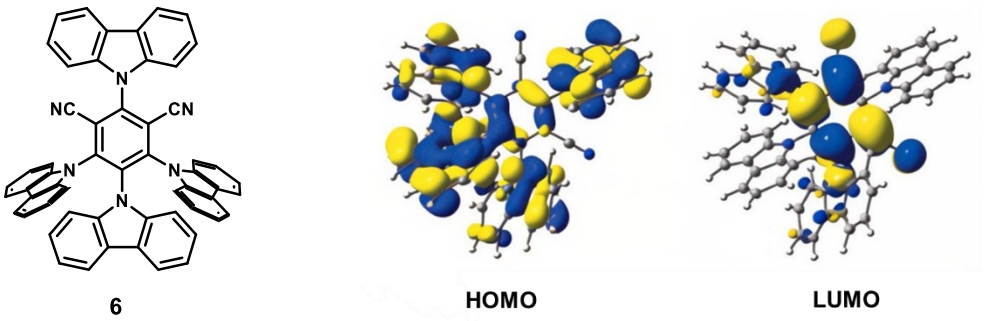

***Figure 1.6**: Representation of 4CzIPN (**6**) on the left and its HOMO and LUMO orbitals on the right (reproduced from [44]).*

Considering HOMO and LUMO as spatially separated, the reduction and oxidation power of the PC can be adjusted almost independently through modifications to either the donor or acceptor parts. In the ground state, emphasizing the electron donating capability of the system, the HOMO is raised bringing to an increase in the reduction potential ($E_{1/2}$ ($PC^{\bullet+}$/PC)). Inversely, accentuating the electron accepting ability will lower the LUMO giving higher oxidation potentials ($E_{1/2}$ ($PC^{\bullet-}$/PC)) as reported in **Figure 1.7** for the 4CzIPN (**6**).[46]

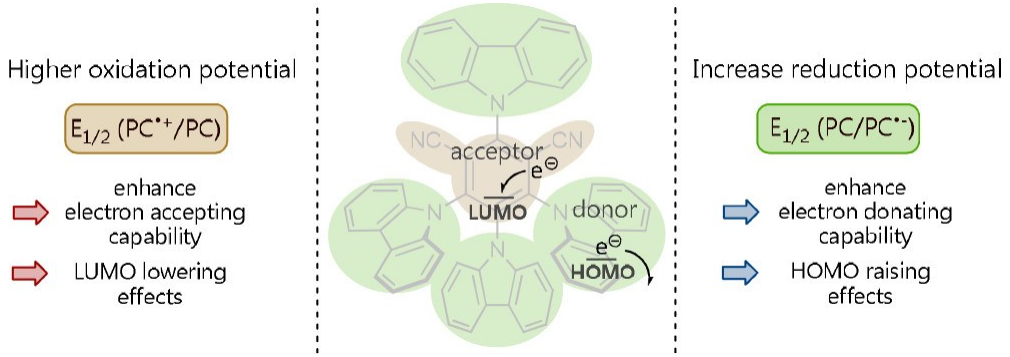

***Figure 1.7**: Correlation of redox potentials and the impact of donor/acceptor strength and modifications (Reproduced from [40]).*

We conclude that the excited state energy is evenly distributed between the oxidation and reduction potentials, creating both a strong oxidant and a strong reductant upon light irradiation generating a bimodal mode of action.

Among bimodal PCs it is important to mention dicyanopyrazines (DPz, **8**), naphthochromenones (NTCs, **7**) and carbazolyl dicyanobenzenes (CDCBs, **9**). This latter class has been particularly significant in this context.[47]

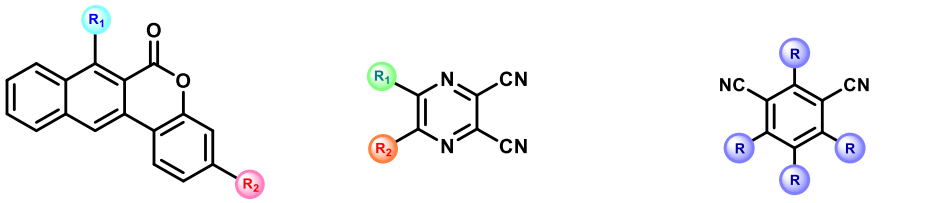

naphthochromenones (NCTs) **7**

dicyanopyraziones (DPs) **8**

carbazolyl dicyanobenzenes (CDCBs) **9**

***Figure 1.8**: Structures of the most common bimodal photocatalysts are shown. Note that for CDCBs, the cyano groups can be positioned differently on the aromatic ring, and in some cases, the R substituents may vary from one another.*

1.1.5 Open challenges

Recently, CDCSs (Carbazole-Dicyanobenzene-Based Catalysts, **9**) have gained significant attention, largely due to their charge transfer (CT) excited states and extended lifetimes, which enable them to mimic the behaviour of metal-based catalysts. Despite their promising performance, challenges remain regarding their stability and recyclability. The recyclability of photocatalysts (PCs) is a critical factor that, while often overlooked in academic research, is likely to become essential for scaling up to industrial applications. To enhance the reusability of these photocatalysts, one approach is to immobilize them on solid particles, ensuring that their catalytic properties are preserved while minimizing light scattering.[48]

Controlled radical polymerizations (CRPs) are particularly valuable in this context, as they allow for the precise growth of polymer brushes, either from or to surfaces, that contain photocatalytic moieties. This method effectively creates supported photocatalysts that are not only efficient but also easy to recover and reuse, addressing key concerns in both sustainability and practical application.

1.2 Polymer brushes

Polymer brushes, first introduced in the 1980s, are defined as *polymer assemblies in which the individual polymer chains are tethered by one chain-end to a solid substrate.* [49][50] As such, polymer brushes have raised substantial interest as functional coatings for a variety of applications (sensor[51], lubricants[52], biomaterials, and many others). [53,54]

Two major approaches can be distinguished for tethering polymer chains to a substrate: *grafting to*[55] and *grafting from.*[56] The former is a top-down technique consisting in the preliminary synthesis of polymer chains comprising an end functionality that enables their grafting onto a surface. Conversely, the *grafting from* approach is a bottom-up method as the chain growth occurs directly from a surface presenting initiator functions that can stimulate polymerization processes (**Figure 1.9**).

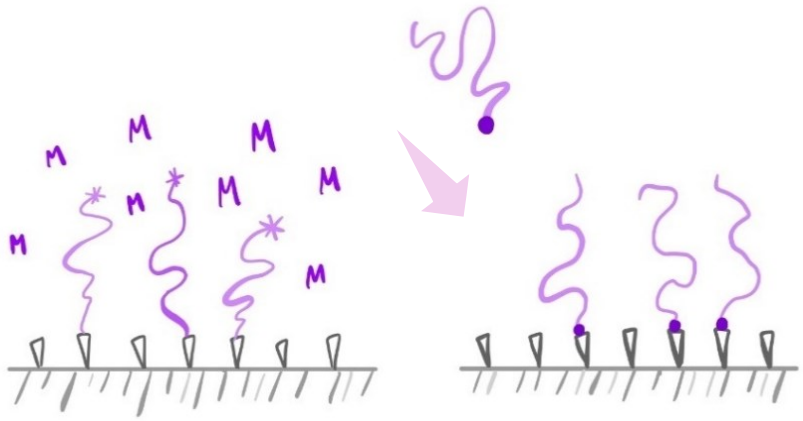

***Figure 1.9**: Representation of grafting from approach (left) and grafting to (right).*

Generally, *grafting from* techniques are preferred because they give access to better control over molar mass, grafting density and dispersity of brushes (**Figure 1.11**).

In *grafting from* approaches, the **molar mass**[57] of polymer brushes is generally described in terms of the thickness of the obtained polymer film. The desired thickness is closely related to their application. For example, just few nanometres are typically sufficient for generating lubricious surfaces (about 10 nm)[58], while

for providing antifouling properties to surfaces relatively high brush thickness should be achieved.[59]

The **grafting density**[60] (σ) principally affects the conformation of the brushes. For elevated grafting densities, polymer chains are physically constrained into a stretched conformation known as *brush* regime. For relatively low values of σ, different morphologies can occur: the so-called *mushroom* morphology arises when the interaction between the chains and the surface is relatively weak. Conversely, for strong interactions a *pancake* morphology is obtained (**Figure 1.10**).[61,62] We should refer to polymer brushes just for the high-grafting-density case. However, we should also consider that for very high grafting densities the polymer brushes are less stable and more prone to de-graft when exposed to thermal stimuli or solvents.[63]

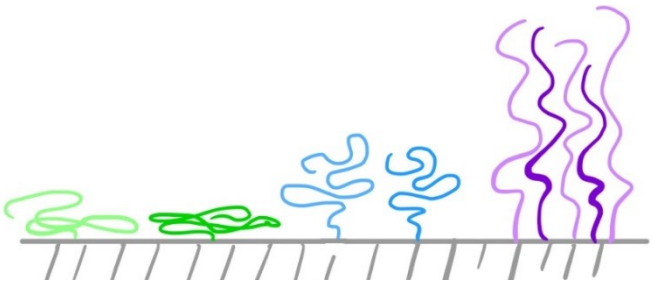

***Figure 1.10**: From left to right the three regimes: pancake, mushroom and brush.*

Finally, the **dispersity** (*Đ*) of grafted chains influence the interfacial properties.[64] Synthetic polymers are intrinsically polydisperse, meaning that different chains possess different lengths. This feature is particularly evident for polymers obtained through free radical polymerization. In the last decades, big effort was spend trying to develop polymerization processes that give access to polymers with narrow distribution of molecular weight, *i.e.,* low *Đ*. Indeed, polymers presenting a low dispersity are reported to present well-defined properties. Usually, a polymer is considered to have low dispersity if $Đ < 1.5$.

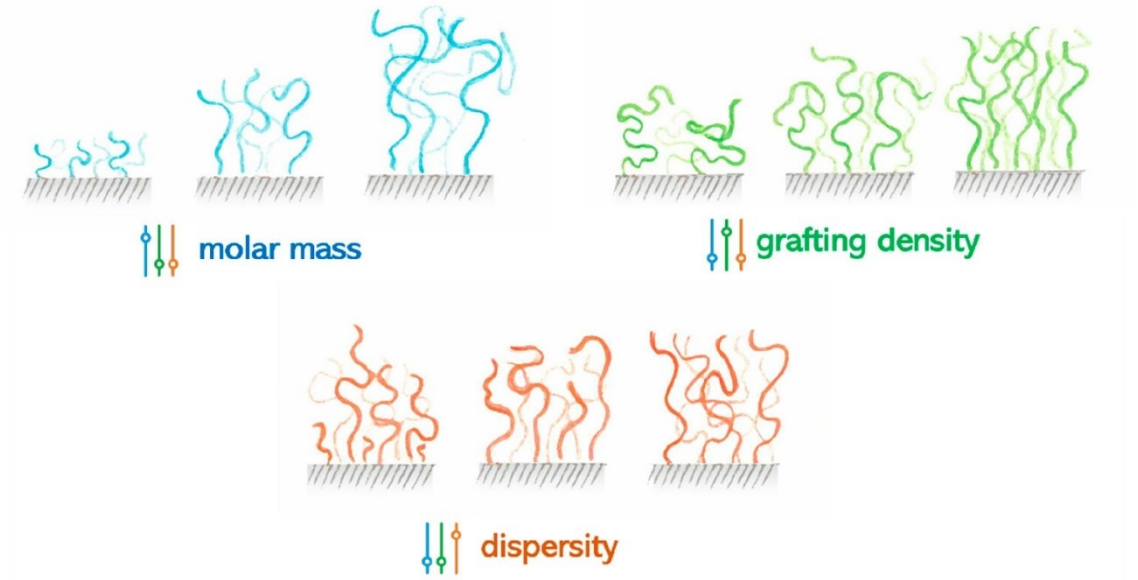

***Figure 1.11**: The main structural parameters of polymer brushes: molar mass, grafting density (σ) and dispersity (Đ).*

The most common way to achieve control over these key parameters of polymer brushes is exploiting surface-initiated reversible deactivation radical polymerization (SI-RDRP) methods. The progress in polymer brushes has been possible thanks to advancements in these surface-initiated controlled polymerization techniques.[65][56]

1.2.1 Reversible deactivation radical polymerizations

Reversible deactivation radical polymerizations (RDRPs) differ from free radical polymerizations. Although they proceed through a radical mechanism, they possess distinct features that resemble living ionic polymerizations[66]. In RDRPs, terminations of propagating chains and other side reactions are minimized by keeping low the concentration of radicals (typically 10^{-8}-10^{-9} M) throughout the polymerization process. Under optimized RDRP conditions all the chains are initiated at the same time, and grow uniformly. However, differently from living ionic polymerizations, irreversible termination reactions among radicals cannot be completely avoided. Thus, the main goal of an RDRP is to elongate the lifetime of radical species that, for free radical processes, is about 1 second before termination occurs. To achieve that, RDRPs are based on an equilibrium between

propagating radicals and their corresponding *dormant species.* The polymer chains remain in a dormant state for most of the polymerization process, thereby avoiding premature radical recombination and disproportionation.

The most employed RDRPs are reversible addition-fragmentation chain-transfer (RAFT) polymerization, nitroxide-mediated polymerization (NMP), photoiniferter-mediated polymerization (PIMP), and atom transfer radical polymerization (ATRP).

RAFT polymerization[67] operates via a radical source (initiator) and a chain transfer agent (CTA), typically a thiocarbonylthio compound containing an easily cleavable S-C bond. When the initiator is activated and adds to a monomer molecule, the resulting radical species then add to the CTA. The CTA generally has a functional R fragment, that is homolytically cleaved, releasing $R^{\bullet}$ into the solution which can propagate by adding to monomer molecules. The resulting radicals add again to the CTA and the RAFT equilibrium of addition-fragmentation of growing chains and CTA is established.

The number of chains bearing the thiocarbonylthio end-group remains constant throughout the polymerization, regardless of the extent of termination. Consequently, the number of dead chains in a RAFT process can be predicted in advance and controlled by varying the number of radicals generated into the system.

Nitroxide-mediated polymerizations (**NMP**)[68] are a type of controlled radical polymerization technique where a stable nitroxide radical serves as a mediator. This process allows for precise control over molecular weight and polymer architecture by reversibly capping the growing polymer chain end with a nitroxide radical, thus regulating the polymerization rate and minimizing termination reactions.

In photoiniferter-mediated polymerization (**PIMP**)[69] an *iniferter* (initiator-transfer agent-terminator) compound is activated under light irradiation to generate radicals. These radicals initiate the polymerization, and the iniferter's ability to

transfer and terminate chain growth ensures controlled polymerization. The use of light as a trigger enables on-demand initiation and halting of the process.

One of the most employed RDRP is atom transfer radical polymerization (**ATRP**).[70] In this thesis work, all polymer brushes were synthesized using this technique that is described in the following section.

1.2.1.1 Atom transfer radical polymerization

ATRP was incepted in 1995 thanks to the independent works of Matyjaszewski[71] and Sawamoto.[72] This technique usually employs a transition metal complex as the catalyst with an alkyl halide (R-X) as initiator. The process relies on an activation-deactivation equilibrium between halogen-capped dormant species and propagating radicals. The latter are generated by activation of the initiator or dormant species by the transition metal complex (Mt^n\L). The activation occurs via the reductive cleavage of a C-X bond by the activator complex, forming a propagating radical and the corresponding oxidized complex X-Mt^{n+1}\L, which then acts as deactivator. The reaction between the deactivator and the radical species revert them back to the dormant state. The deactivation rate constant k_{deact} is generally bigger than the activation one (k_{act}), thus the ATRP equilibrium is shifted toward dormant species. This is key for the control as the radical's concentration is kept low, minimizing termination processes. The transition metals used in ATRP are many (Fe, Cu, Mo etc.), but in most cases Cu is the most effective[73].

In a typical ATRP, a Cu(I) complex is employed (Cu(I) /L, where L is a polydentate amine ligand), which is responsible for the cleavage of the C-X bond forming propagating radicals while turning into a Cu(II) complex, namely Cu(II)X/L that will act as the deactivator (**Scheme 1.8a**).

However, several ATRP mechanisms have been developed with the aim of employing a Cu(II) complex that is reduced in situ in the polymerization mixture, rather than a Cu(I) complex that requires strictly inert atmospheres.[74] Among these, the most common are initiators for continuous activator regeneration (**ICAR**) ATRP[75], supplemental activation reducing agent (**SARA**) ATRP[76],

photochemically mediated ATRP (*photo*ATRP),[77] electrochemically mediated ATRP (**eATRP**),[78] and activator regenerated by electron transfer (**ARGET**) ATRP.[79]

In ICAR ATRP, a source of free radicals is used to slowly and continuously regenerate the Cu(I) activator, which would otherwise be depleted by termination reactions. For SARA ATRP, Cu(0) is introduced and serves as both a supplemental activator and a reducing agent via comproportionation with Cu(II) species. This results in the generation of a Cu(I) species that is the primary activator of the dormant alkyl halides. PhotoATRP and *e*ATRP are more environmentally friendly procedures employing light irradiation and electrical stimuli, respectively, for controlling the activation/deactivation equilibrium.

Finally, in ARGET ATRP a reducing agent is added, which is responsible for the continuous regeneration of the active oxidation state of the metal complex (**Scheme 1.8b**).

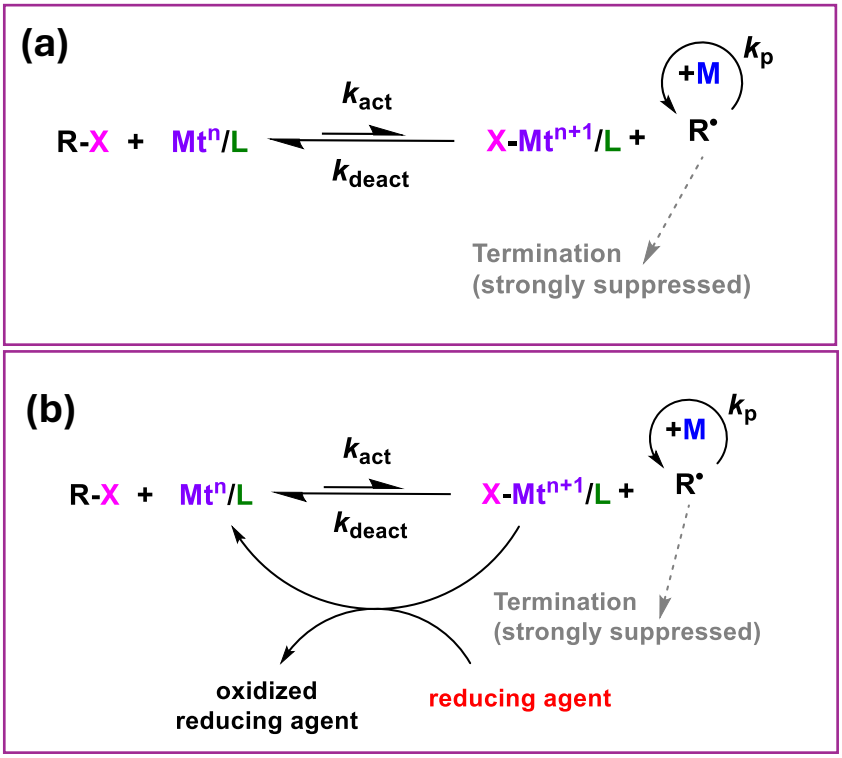

***Scheme 1.8**: Generalized mechanism of a) normal ATRP and b) ARGET ATRP.*

ARGET ATRP can be considered a greener alternative to the normal ATRP, since the amount of the metal catalyst needed is much lower. This is possible because the activator is continuously reformed thanks to a reducing agent such as tin(II) 2-ethylhexanoate ($Sn(EH)_2$), glucose, ascorbic acid, sodium ascorbate, silver metal etc. Another advantage is that the rate of polymerization can be controlled by adjusting the type and amount of reducing agent or by slowly or intermittently feeding it into the polymerization mixture. Nevertheless, one must be careful in selecting the reducing agent, considering not only its redox activity but also to prevent any potential side reactions that translate into a loss of control. Finally, the oxygen sensitivity of the polymerization, that represents the main drawback of ATRP, is decreased in ARGET ATRP owing to the presence of excess reducing agent relative to the catalyst, which can reduce the Cu(II) species that can be formed by reaction between the activator and adventitious oxygen.[80–83]

1.2.2 Polymer brushes by ATRP

ATRP is one of the most used techniques for the growth of brushes from initiator-functionalized substates.[84,85]

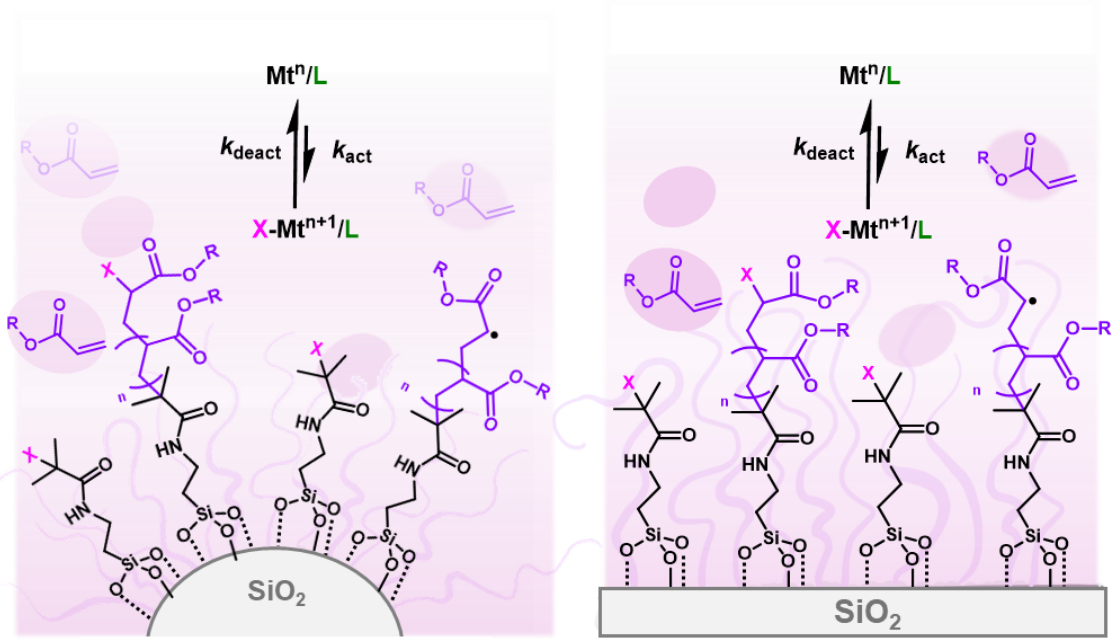

***Figure 1.12**: Graphic representation of brush growth through SI-ATRP from initiator-functionalized flat and spherical surfaces.*

If the alkyl halide initiator is immobilized on a surface instead of being used in solution, then ATRP techniques can be used for surface modification[86]. The two most common types of modified surfaces are flat surfaces and spherical particles (**Figure 1.12**), nevertheless SI-ATRP has been applied to a broad variety of substrates, including porous and nanostructured materials.

The growth of brushes from inorganic supports lead gives access to hybrid materials characterized by a multifunctional character and tunable properties. In this work, I will specifically focus on the functionalization of spherical particles.

Growing polymer brushes from inorganic particles provides hybrid particles with a polymeric shell and an inorganic core of different sizes, including nanoparticles (NPs) that show applications in a large variety of fields. In biomedicine,[87] for example, when NPs are used for drug delivery, the fabrication of a brush shell can improve their biocompatibility, provide control over the release of drugs[88] and increase the colloidal stability in physiological environments.[89] Additionally, they can be used as biosensor[90] where the brushes enhance the selectivity and sensitivity thanks to the presence of specific binding sites for target biomolecules. In composite materials, functional NPs are exploited to improve mechanical properties or thermal stability. They also find application in the field of batteries where functionalized nanoparticles are developed as flame retardant,[91] or again, they are used for capturing and/or degrading pollutants in water.[92]

Inorganic particles presenting polymer brush-shells have enormous potential and one of the emerging applications is their use as support for catalytic systems.

1.2.3 Supported catalytic systems

In recent years, the concept of supporting (photo)catalysts on materials has gained popularity for two main reasons. First, it allows for combining the benefits of (photo)catalysis with the properties of the support material.[93] The polymer can be tailored to meet specific requirements, such as improving thermal and chemical stability,[94] addressing solubility issues,[95] or facilitating selective interactions.[96] Additionally, supported catalysts typically offer a longer lifespan

and extended operational life.[97] However, what has most captured the attention of the scientific community is the opportunity to increase the sustainability of catalytic processes.[98] For several years now, the field of (photo)catalysis has been moving towards more sustainable chemistries by replacing rare earth metal-based catalysts with purely organic compounds. Nonetheless, there are several aspects that need improvement to make this field even more sustainable, the first among them is the reuse of catalysts. This aspect, which can be crucial for industrial scalability, is generally ignored due to challenging and costly purification processes, and poor stability of catalytic compounds.

The development of supported catalytic systems can overcome these issues, facilitating the separation of catalysts from the reaction mixture, and enabling their recovery and reuse.

Polymers represents a valid option to be used for supporting catalysts.[99] The main advantages in the use of polymers are their low price and ease of synthesis. Furthermore, these materials can be endowed with a wide variety of functionalities, enabling the properties to be easily adjusted to meet specific application requirements.

There are two main approaches that can be followed to incorporate photocatalysts: (i) the first one is based on the attachment of the photocatalyst to a pre-synthesized functional polymer by post-polymerization modifications;[100,101] (ii) the other and most used strategy consists of the modification of the catalytically active molecule so that it can be (co)polymerized.[102–104] This second approach enables a more controlled integration of the catalyst into a large range of structures. Practically, one needs to design a monomer bearing the desired catalytic moiety, starting from the scaffold of existing catalysts and modifying them to add a polymerizable functionality. However, it is important to preserve as much as possible the original structure of the catalyst not to alter its catalytic activity. This approach makes the insertion of the photocatalyst within polymer chains less demanding and controllable, especially using RDRP techniques. Indeed, the use of RDRPs facilitates the regulation of critical parameters such as the degree of incorporation and the position of the catalytic moieties along the chains. Initially, we could consider creating a homopolymer of the photocatalytic

monomer. However, this approach is less desirable because it would not integrate the properties of a chosen polymer with the photocatalyst, and auto-quenching would likely be a significant issue. Therefore, copolymers are generally preferred. A copolymer is a polymer made by linking two or more different monomers together. Depending on the choice of monomers and the strategies used, we can produce various types of copolymers, including statistical, gradient, alternating, or block copolymers. Statistical copolymers, also known as random copolymers, has a random distribution of the monomers along the polymer chain. Statistical copolymers, or random copolymers, have a random arrangement of monomers along the polymer chain. Gradient copolymers feature a gradual transition in monomer composition, whereas alternating copolymers have a regular sequence of monomers, such as ABAB. Finally block copolymers consists of long sequences (blocks) of two or more different monomers linked together in a linear arrangement.

In the specific case of incorporating a photocatalyst, the resulting (co)polymer could be used for several light-mediated reactions, it should be recovered and reused. In addition, by engineering the polymer structure and its composition, the polymeric environment has the potential to enhance the activity, selectivity, and stability of the photoactive species.[105]

The (co)polymer can be used under homogeneous conditions, meaning in solvents where the copolymer is soluble and easily accessible by the reacting substrates. Importantly, the judicious selection of the copolymer composition can enable to perform homogenous catalysis in solvents where the photocatalyst itself is not soluble. This condition generally leads to highly effective photocatalytic materials, nevertheless, reactions where the photocatalyst-embedding copolymers are not soluble, thus forming heterogeneous systems, were also reported.[101][106]

These copolymers can be tailored for specific needs such as solvent compatibility, light transmittance, or the positioning of the photocatalyst. Their properties, mostly dictated by the choice of comonomers, can be tailored to achieve the desired outcome, giving access to a highly adaptable platform. The monomer that is copolymerized with the monomer incorporating the photocatalyst

usually represents the major molar fraction, and it is often chosen solely based on the desired characteristics of the material. Indeed, in most reported systems, the possibility of interactions between the photoactive part and the structural part is overlooked, with the assumption that the polymer environment has no actual influence on the catalytic activity, as often observed. Very few literature examples studied the influence of polymer composition on photocatalytic properties. Kobashi and Yoo[107] covalently incorporated an Ir-based photocatalyst in copolymers combining ethyl methacrylate with styrene, *N*-isopropyl acrylamide, or benzyl methacrylate, and measured different catalytic activities. Similar effects are observed in the emerging field of artificial photoenzymes.[108] In these systems, the position of the photocatalyst within the microenvironment can largely impact the efficiency. Recently, Ferguson group[109] studied the comonomer effect for vinyl based photocatalytic polymers. They reported that with some comonomers the photophysical properties of the diphenyl benzothiadiazole photocatalyst were significantly different, while the photocatalytic efficiency was mainly dependent on the reaction conditions. Thus, based on the state-of-the-art of photocatalyst-embedding copolymers, we can generally assume that binding a photocatalyst within a polymer will not significantly affect its features. Conversely, it is well described that the photocatalyst structure and the reaction solvent can have a big impact on the catalytic performance.

Incorporating photocatlyst-bearing monomers along polymer chains can be a way to address some of the main drawbacks of photocatalysis such as solubility issues and poor recyclability. However, polymers are not always easy to separate from the reaction mixture, and it is not uncommon to lose part of the material in the separation process. Additionally, purification steps are often required before reusing the polymer, leading to further material loss and making the process sometimes tedious and time-consuming.

A more efficient approach is to combine the copolymerization of the photocatalyst with a substrate, such as nano- or microparticles, that supports the copolymer yielding core brush-shell particles.

This system consists of a substrate (particles) surrounded by a polymer brush layer that hold or support photocatalysts (**Figure 1.13**), creating a structure that combines the functional properties of both the polymer matrix and the catalytic moieties. This method retains the benefits of the polymeric material while simplifying separation. Using simple filtration or centrifugation techniques, the entire system can be recovered, and the purification steps are replaced by straightforward washes. Although limitations might include the leaching of the photocatalyst from the brush, particularly if the bonding isn't strong enough (for example easy hydrolysable functionalities), moreover the photocatalyst may be partially or fully encapsulated by the polymer brush, limiting the accessibility of reactants to the catalytic sites and reducing the overall efficiency of the photocatalytic process. Furthermore, if the photocatalysts are positioned too close together, auto-quenching in the excited state may become a drawback. By finding the right morphology to overcome the limitations of this configuration, this setup holds enormous potential.

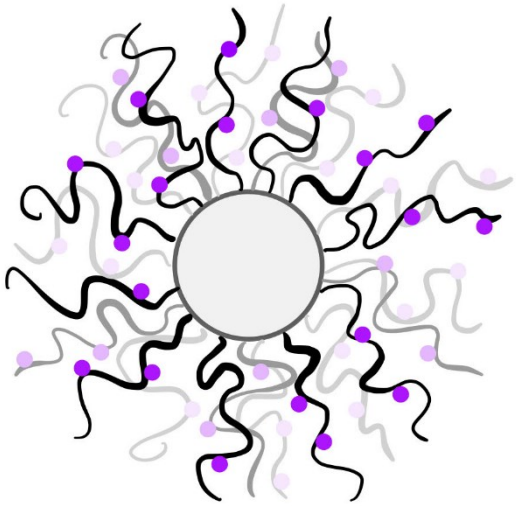

***Figure 1.13**: Graphic representation of core-shell particles with the photocatalyst integrated in the shell.*

Functionalized **particles** are highly attractive materials because they can be produced inexpensively through various synthetic routes. Similarly to polymers, the photocatalytic moiety can be incorporated either after or during polymerization. While post-modification of synthesized particles is a well-established method, designing photocatalysts that can be easily copolymerized

into polymers offers greater flexibility in terms of synthesis approach, concentration, positioning, and monomer selection.

Facilitating the recyclability is not the only advantage of this configuration. Indeed, the easy separation of the entire system allows for totally avoiding contamination of the reaction media. For this reason, examples of particles-supported photocatalysts used for water treatment are frequently reported in the literature. As recently reported by Pester *et al.*, the use of disinfecting chemicals can have environmental implications, however they can be replaced by the photocatalytic activity of organic dyes through singlet oxygen sensitization.[110] Once in its singlet state, oxygen acts as an oxidant with bactericidal effect. It is important to emphasize that this use of organic photocatalysts is only possible by overcoming the water-insolubility issue by virtue of the catalyst incorporation within a suitable material. For example, if anti-fouling properties are desired, a hydrophobic polymeric matrix would be selected. Conversely, if the objective is to improve interaction with species dissolved in water, a water-soluble polymer would be the preferred choice. The ability to efficiently disperse a photocatalytic material in water also enables a crucial aspect of a green transition: performing reactions in aqueous environment. For instance, photoreactions in water holds considerable promise for more sustainable chemical processes. However, modifying catalysts to make them water-soluble can be very challenging, also considering that such modifications may negatively impact the performance of photocatalysts.[111] Circumventing this limitation is possible incorporating a small percentage of the not water-soluble photocatalyst in a water-soluble polymer, avoiding the substantial structural modification and the loss of catalytic activity.

Two major approaches for supporting photocatalysts within polymer brushes can be identified. These can be distinguished by the type of employed support. In the first strategy, polymer brushes are linked to organic beads[103], while the second approach involves the use of inorganic particles and the fabrication of hybrid materials.[112]

The first approach implies attaching brushes to or from existing organic materials. A notable example that was an important inspiration for later researches is this field is the work of Neckers *et al.* in 1975[113], where Rose Bengal was immobilized

on particles made of Merrifield resin. In recent years, core-shell polymer nanoparticles have been created by exploiting the self-assembly of polymer chains during polymerization in selected solvents, such as through PISA RAFT polymerization.[103] PISA (Polymerization-Induced Self-Assembly) using RAFT (Reversible Addition-Fragmentation Chain Transfer) polymerization is a technique that combines polymerization with self-assembly to create structured polymer materials. PISA leverages the tendency of certain polymers to spontaneously organize into well-defined structures (particles, micelles, vesicles etc.). Combining it with RAFT polymerization is a powerful tool that merges controlled polymerization with self-assembly, enabling the creation of advanced materials such as particles with an external *brush* layer. This method allows for manipulation of both the core and the brushes. For instance, systems have been fabricated with hydrophilic brushes and a hydrophobic core, allowing the photocatalyst to be positioned in either the core or shell to simulate enzymatic substrate specificity and selectivity.[114]

In the second approach, particles may be metal-based, playing a role in catalysis or serving as a cost-effective solution for magnetophoretic separation if a paramagnetic material is used.[115] Alternatively, the core may act purely as a support, as seen with inert silica beads.[116] These methods require surface activation of the particles, and the immobilization of an initiator to start the polymerization.

The major criticisms associated with these systems can be related to the penetration of the organic substrates within the brushes and the scattering of the light due to the particle-core configuration. However, diffusion can be enhanced by either reducing the grafting density of the brushes or adjusting the position of the catalyst along the chains to avoid overly internal locations. Light scattering, on the other hand, reduces light penetration, thereby diminishing the system's effectiveness. However, the issue of light scattering can be minimized by reducing the size of the supporting particles. While very small particles (a few nanometres) are challenging to separate using conventional techniques, external triggers can facilitate this process. For example, a non-solvent or pH triggers can be added, as demonstrated by Ferguson’s group that fabricated pH-responsive polymer

photocatalyst nanoparticles. Increasing the pH of the aqueous medium caused the particles to contract, leading to aggregation/precipitation,[117] thus facilitating their removal from the reaction mixture.

However, the main problems that can occur it is linked to the chemical degradation of the catalysts. Especially when dealing with organic molecules, they are very prone to leaching, which obviously invalidates the recycling process. Recently, a study conducted by Pester's group demonstrated that light irradiation for just a few hours can lead to photobleaching of certain photocatalysts (specifically fluorescein, rose bengal, and eosin Y).[118] This phenomenon occurs whether the molecules are used in solution, directly immobilized on inert supports, or incorporated within brushes. It cannot be generally asserted that the copolymerization of photoactive units prevents their degradation, but some considerations can be made in this regard. In some instances, selecting an appropriate structure can indeed protect the photocatalytic moieties. The incorporation of photocatalytic moieties within crosslinked brushes a was reported to have a beneficial effect, whether by introducing a crosslinker[119] or by employing the catalyst itself as a crosslinker.[110] These structures appear to provide a more protective environment for the photocatalyst maybe limiting the interaction between the radical form of the PC and the radical intermediates of the reaction.

Nevertheless, there are numerous examples of catalysts such as fluorescein,[116] rose Bengal,[120] eosin Y,[102] porphyrins[110] and others being reused.

These examples highlight that there is a significant dependence of photocatalyst degradation on reaction conditions.

1.3 Aim of the project

To the best of our knowledge, photocatalysts like carbazolyl dicyanobenzenes have not been explored in the area of recyclability. Among them, a significant and interesting consists of IPN-based photocatalysts. These catalysts are distinguished by their long excited-state lifetimes and the ability to incorporate various substituents on the IPN core. This extensive range of possible structural

modifications renders the library of IPNs virtually infinite, allowing for the exploration of a broad spectrum of redox potentials.

However, IPN photocatalysts are also known for their limited stability, making their recyclability an ongoing challenge. This project aims to address this issue by employing a model IPN catalyst specifically designed for this purpose.

This work will focus on the synthesis of a polymerizable carbazolyl dicyanobenzene and its incorporation into polymeric supports using ARGET ATRP and SI-ARGET ATRP, with the goal of enabling its recovery and reuse in photocatalysis.

The first part of the project focused on the design, synthesis, and characterisation of a photocatalyst that can be incorporated within a poly(acrylate) chain through controlled radical (co)polymerization. This relies on the modification of a cyanoarene-based core, using 1,2,3,5-tetrakis(carbazol-9-yl)-4,6-dicyanobenzene (4CzIPN) and an acrylate function. Two synthetic pathways were explored: one pot synthesis and a two steps one passing through the isolation of the intermediate. This second is the one optimized for the synthesis on grams scale. Subsequently, PCs were copolymerized with (oligoethylene glycol)acrylate (OEGA) both in solution and from initiator-functionalized silica particles exploiting control radical techniques, namely (SI-) ARGET ATRP. The polymerizations were initially optimized in solution using an alkyl halide as the initiator. This was followed by optimization on flat surfaces, where the C-X terminated initiator was immobilized on the silicon substrates. These optimized conditions were then applied to initiator-functionalized silica particles, enabling the successful fabrication of the final system.

The copolymer in solution was extensively studied to demonstrate its photoactivity and, under specific conditions, its recyclability. This led to the preliminary testing of the functionalized particles as active photocatalysts.

2. Results and discussion

2.1 Development of the project

The key characteristic of photocatalysis is the efficient generation of highly reactive intermediates under mild conditions, without the need for harsh reaction conditions. This enables the activation of a wide range of substrates that are typically unreactive in under typical reaction conditions. Additionally, the diversity of compounds that can be synthesized as photocatalysts is gives access to new synthetic methodologies.

Visible light organo-photoredox catalysis has demonstrated its enormous potential for facilitating challenging chemical reactions while offering a cheaper and greener alternative to transition metal-based photocatalysts.

To date, there are numerous families of organic photocatalysts that, thanks to structural modifications provide a wide range of redox potentials. We can mention, just as examples: acridinium salts,[123] flavins,[124] phenazines,[125] phenothiazines,[126] quinones[127] or naphthocromenones[45].

Among these, a large and noteworthy family is that of IPNs (**9**). These catalysts, characterized by long excited-state lifetimes, typically consist of an electron-withdrawing unit and an electron-donating unit conjugated in more or less rigid structures. The ability to use various substituents, each of which can be structurally modified, makes the library of IPNs virtually infinite. Just few examples of the most common modifications are reported in **Figure 2.1**, but many others are reported in literature[47,128]. However, while for some families of PCs the possibility of recycling is known, for IPNs it remains a challenge. Namely, the open challenges associated with the use of IPN PCs are the overall stability, the recyclability and the implementation of these PCs in heterogeneous, supported systems. Indeed, the possibility of supporting organic PCs can generate easily recoverable catalytic systems, but it represents a complex issue, since solid supports can profoundly alter the ground and excited state properties of PCs, while introducing scattering problems[48]. Notably, one of the most studied compounds of the IPN class is the 1,2,3,5-tetrakis(carbazol-9-yl)-4,6-

dicyanobenzene, commonly referred as 4CzIPN (**6**). This molecule represents the starting point of this project.

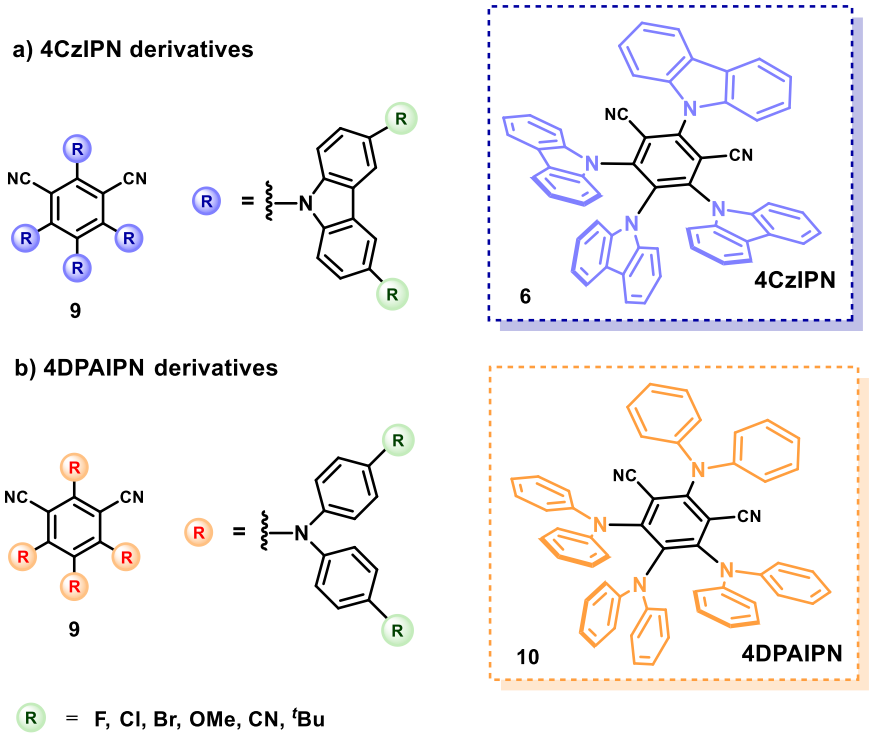

***Figure 2.1**: Common modifications to the IPN core involve substituting the aromatic core with different groups. Using carbazoles (Cz) results in 4CzIPN, while using diphenylamine (DPA) produces 4DPAIPN (1,3-Dicyano-2,4,5,6-tetrakis(diphenylamino)-benzene), a more reducing photocatalyst. Further modifications to Cz or DPA can create analogues with varying redox potentials.*

During this thesis project I designed a photocatalyst with a similar structure and activity, but presenting a polymerizable functionality, enabling the copolymerization of this photoactive moiety with an amphiphilic monomer, such as oligo(ethylene glycol)methyl ether acrylate (OEGA). Copolymerization of photocatalyst-bearing acrylate with OEGA was performed by activator regenerated by electron transfer atom transfer radical polymerization (ARGET ATRP), an RDRP technique that requires a small amount of transition metal complexes as catalyst. The photoactive compound (PC) was copolymerized with OEGA both from an initiator in solution, producing a photoactive polymer, and from initiator-functionalized silica particles (SI-ARGET ATRP), resulting in core-shell structures with the PC integrated into a polymer brush shell.

The resulting photoactive polymer was characterized in terms of photophysical properties and compared with the corresponding organic molecule. Additionally,

the polymer could be separated from the reaction system, thus allowing for testing the recyclability of the catalyst. Lastly, the amphiphilic nature of the monomer was leveraged to solubilize the photocatalyst in aqueous medium and test reactions in water.

2.2 The photocatalyst

The first part of the project focused on the design, synthesis, and characterisation of a photocatalyst that can be incorporated within a poly(acrylate) through a controlled radical copolymerization process. This relied on the modification of **6** (4CzIPN) structure by substituting the carbazole in the fourth position with a glycolic chain bearing an acrylate function at the end (3CzIPN-A , **Figure 2.2a**).

Triethylene glycol was chosen as a linker between the photocatalytic moiety and the acrylate function. The use of such a long chain was meant to avoid any potential interactions between the photoactive part and the polymer backbone, which could have altered the catalytic properties. However, it was anticipated that this structural modification would lead to changes of physicochemical properties of the entire photoactive compound. Indeed, replacing a bulky substituent like carbazole with a much less bulky chain led to a loss of structural rigidity, which impacted the final compound's properties, such as redox potentials and lifespan.

The PC-bearing monomer **11** (obtained following the procedure described in *section 4.3.1)* was subsequently characterized (*S.I.* 4.5, 4.5 and 4.7), together with a saturated version of the PC **12** (**Figure 2.2b**) that does not include the acrylic functionality. This step was necessary for a better comparison of the reduction potentials of **11** with the subsequent characterization of the copolymer **47** (*S.I.* 4.7). Indeed, once incorporated into the copolymer backbone, the monomer does not exhibit the terminal double bond.

The 3CzIPN-A **11** was fully characterized comparing its properties with the ones of 4CzIPN (**6**) used as reference.

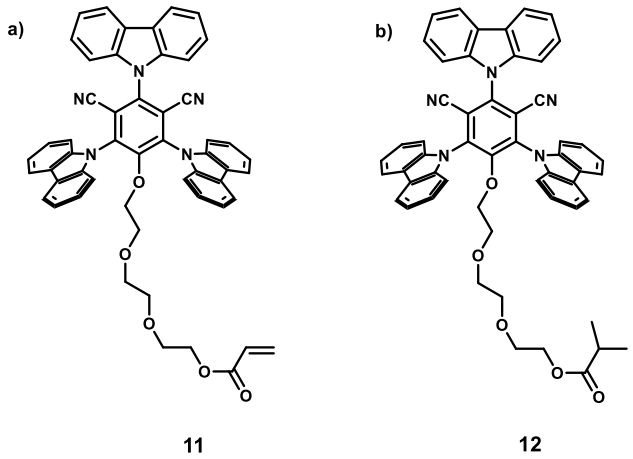

***Figure 2.2**: a) Structure of the monomer 3CzIPN-A (**11**); b) structure of the reduced version of the monomer for its redox potential characterization (**12**).*

Firstly, the lifetime of the excited state of **11** was measured for two main reasons. First, it is reported that the excited state of a photocatalyst must have a lifetime of at least 1 ns, otherwise the compound tends to emit before forming the encounter complex with the substrate.[28] Secondly, one of the most important features of **6** is its very long excited-state lifetime, which is correlated to its TADF behaviour. Measuring the lifetime was necessary to confirm that the excited state duration was sufficiently long and to determine if the compound still exhibited reverse intersystem crossing (RISC).

Two different techniques were used for this purpose. Direct fluorescence was measured using time-correlated single-photon counting (TCSPC)[129]—a technique typically employed for short lifetimes (a few nanoseconds at most). In this method, a detector converts a single photon into an electronic pulse, and the TCSPC electronics accurately measures its arrival time relative to the excitation pulse. Thousands of arrival times are recorded showing their statistical intensity at a given time, from which the decay fitting provides the lifetime (**Figure 2.3a**).

For delayed fluorescence, a more suitable method is Multi-Channel Scaling (MCS),[130] a photon counting technique generally used for measuring longer lifetimes. In MCS, multiple photons are collected in each sweep of the time window, quickly accumulating decays across timescales ranging from several hundred nanoseconds to seconds (**Figure 2.3b**).

The emission analysis proved that the synthesized compound was still showing the TADF behaviour, meaning that the fluorescence decay exhibited a double exponential behaviour:

$$I(t) = B_1 e^{-\frac{t}{\tau_1}} + B_2 e^{-\frac{t}{\tau_2}}$$

Namely, **11** showed a lifetime of 10.5 ns for the prompt fluorescence (τ_p) and 255 ns for the delayed one (τ_d).

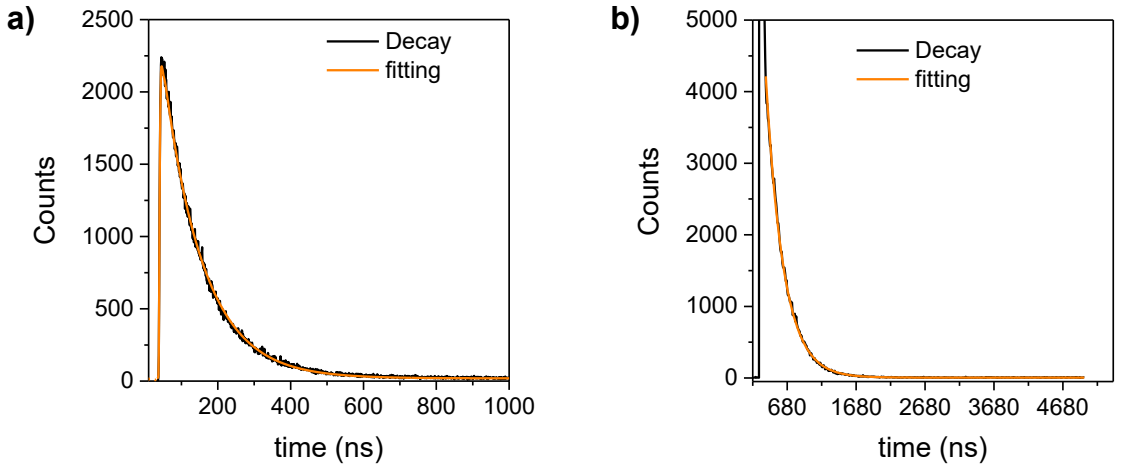

***Figure 2.3**: a) Exponential decay and fitting for lifetime measurement of direct fluorescence of 3CzIPN-A in ACN at room temperature with TCSPC technique. b) Exponential decay and fitting for lifetime measurement of delayed fluorescence of 3CzIPN-A (**11**) in ACN at room temperature with MCS technique.*

Comparing these values with lifetime measurements of **6** under the same conditions,[131] it is evident that the lifetimes of **6** are longer (**Table 2.1**), in particular for the delayed fluorescence.

***Table 2.1**: Comparison between fluorescence lifetimes of 3CzIPN-A (**11**) and 4CzIPN (**6**). 4CzIPN measurements are reported from the literature,[131] while 3CzIPN-A were measured at room temperature in ACN, by degassing the solution with N_2.*

	4CzIPN	3CzIPN-A
Prompt fluorescence	18.7 ns	10.5 ns
Delayed fluorescence	1390 ns	255 ns

We can speculate that the reason behind this result lies in the lower rigidity of **11**. In fact, it is described that bulky substituents, and consequently a sterically hindered system, exhibit longer lifetimes of the excited state. This is linked to the larger separation of HOMO and LUMO orbitals, and so to a worse overlapping of

the orbitals' wavefunctions.[132–134] In a rather simplified explanation, we can say that the electron, once in the triplet state, finds it more difficult to return to the singlet state, translating in longer reverse intersystem crossing and consequently longer delayed fluorescence.

Another very important feature to be analysed are the reduction potentials of the photoactive molecules, particularly those that are required to estimate the excited state potentials. For this purpose, the reduced version of the monomer was synthesized (3CzIPN-red, **12**). Cyclic voltammetry in ACN was performed (*S.I.* 4.7) to calculate the half-wave potential $E_{1/2}$ of the photocatalyst in its different oxidation states. For the estimation of the potentials of the excited state, the Rhem Weller formalism was applied. Experimentally, the intersection point between the normalized absorption and emission spectra is calculated, and it presented a small blue shift with respect to **6**. The wavelength of the intersection point was converted to eV finding the $E_{0,0}$ and this value subtracted or summed to the $E_{1/2}(PC/PC^{\bullet-})$ or to the peak potential of $(PC^{\bullet+}/PC)$, respectively, calculated from the CVs. The results compared to the corresponding parameters for the 4CzIPN (**6**)[135] are reported in **Table 2.2**.

***Table 2.2**: Calculated potentials (reported in V vs SCE) of **6** and 3CzIPN-red (**12**) performing CVs in ACN at room temperature using tetrabutylammonium hexafluorophosphate ($TBAPF_6$) as supporting electrolyte.*

	$E_{1/2}(PC^*/PC^{\bullet-})$ (V)	$E_p(PC^{\bullet+}/PC^*)$ (V)	$E_{1/2}(PC/PC^{\bullet-})$ (V)	$E_p(PC^{\bullet+}/PC)$ (V)	$E_{0,0}$ (eV)
4CzIPN (**6**)	+1.43	-1.18	-1.24	+1.49	2.67
3CzIPN-red (**12**)	+1.44	-1.53	-1.30	+1.21	2.74

It is evident that in terms of redox potentials, the structural modification to the pristine 4CzIPN structure did not significantly affect the compound, resulting in a very similar potential for the reductive quenching path, while the capability for the oxidative quenching path is enhanced.

2.3 Copolymerization

Once the polymerizable photocatalyst **11** was obtained, the next step was its copolymerization with the selected acrylate monomer, to study the properties after incorporation into a polymeric chain, prior to testing its catalytic activity.

2.3.1 Optimization of polymerization in solution

I initially focused on optimizing the polymerization conditions for OEGA in solution without adding 3CzIPN-A (**11**). ARGET ATRP was chosen as controlled radical polymerization technique, using EBiB (**44**) as the initiator in solution and targeting a degree of polymerization of 200. The degree of polymerization (DP) measures the number of monomer units in a polymer chain, reflecting the chain's length. A DP of 200 implies that each polymer chain consists of 200 monomers, assuming ideal conditions with 100% conversion and uniform chain length.

***Table 2.3**: optimization of OEGA polymerization in solution. $Sn(oct)_2$ is used as reducing agent in excess with respect to the copper catalyst. The reactions were followed by ^{1}H-NMR to study the kinetic and monomer conversion. The amount of metal-based catalyst was gradually diminished and the solvent was changed from DMF to DMSO. The reported M_w and M_n were obtained by GPC, calculated using a calibration curve based on PMMA standards. In the last entry, M_w, M_n and Đ were not calculated as DMSO was not compatible with the GPC columns (reported in section 4.2, Instruments).*

Entry	$Cu(Br)_2$ (mM)	Conversion (18 h)	M_w (Da)	M_n (Da)	Dispersity (Đ)	Solvent
1	9.0	20%	12000	10100	1.19	DMF
2	2.2	25%	17000	13600	1.25	DMF
4	0.45	5%	6800	5600	2.02	DMF
5	1.8	8%	11500	9300	1.23	DMF
6	0.56	14%	5000	4300	1.17	DMF
7	0.56	84%	-	-	-	DMSO

The employed transition metal catalyst was $Cu(II)Br_2$ with an excess of ligand (1:5 Cu:ligand ratio)—specifically, Tris[2-(dimethylamino)ethyl]amine (Me_6TREN), which is known to increase the rate of polymerization compared to other ligands commonly used for similar ATRP systems.[136] OEGA was chosen

as comonomer to generate PC-bearing copolymers that could catalyze reaction both in organic and aqueous media. The polymerization procedure is detailed in section 4.3, *Procedures*.

For the polymerizations reported in **Table 2.3**, $Sn^{II}(Oct)_2$ was used as reducing agent, which is a rather mild reductant often used in ARGET ATRP.[137] In all the reported polymerizations the amount of reducing agent was twice the molar amount of copper.

The dispersity (*Đ*) of the polymer chains is generally low (*Đ* < 1.5), which is expected for a controlled polymerization. However, most reactions stopped at relatively low conversions (<25%). This could indicate that termination processes were occurring, or oxygen traces were present in the polymerization mixtures, resulting in oxidation of the Cu(I) species impeding the (re)activation of dormant chains. Indeed, oxygen can be very tedious in ATRP even in small amounts. Nevertheless, by comparing Entry 6 and 7 of **Table 2.3** it is evident that DMSO aids the polymerization process.

This outcome can be attributed to two main factors. First, ATRP polymerizations tend to proceed faster with increased solvent polarity.[138,139] This is attributed to different reasons:

- solubility of catalysts and ligands: polar solvents improve the solubility of the metal catalysts and ligands, ensuring better interaction and homogeneity in the reaction mixture.
- faster activation of dormant species: polar solvents can enhance the activation of dormant polymer chains by stabilizing the active species. This stabilization leads to a higher concentration of active radicals, speeding up the polymerization process.
- reduced chain transfer and termination. In polar solvents, the likelihood of chain transfer and termination reactions can be reduced. This reduction means that more chains remain active and continue to grow, contributing to a higher rate of polymerization.

Overall, the use of polar solvents in ATRP facilitates the key steps in the polymerization mechanism and leads to faster and more controlled polymer growth.

The second reason is that DMSO enhances tolerance to oxygen. One of the main weaknesses of ATRP is the high sensitivity to oxygen, as the diradical •O-O• terminates the chains, mostly by forming peroxide species that do not undergo propagation. DMSO, being a scavenger of oxygen and diminishing the solubility of oxygen, effectively mitigates this issue.

2.3.2 Copolymerization of OEGA and 3CzIPN-A

The conditions of Entry 7 in Table 3.3 were then used for the copolymerization of OEGA with a 5 mol% of **12** yielding the copolymer p(OEGA-*co*-3CzIPN-A). The incorporation was firstly confirmed from the emission of the polymer under UV light and quantified as a 3.5 mol% using ^{1}H-NMR (*S.I.* 4.5) and a UV-Vis calibration (the calibration line was built with the monomer **11**, **Figure 2.4**).

Then, the copolymer containing the photocatalytic moiety (**47**) was characterized, showing very similar behaviour to **11** in terms of absorbance, fluorescence and redox potentials (*S.I.* 4.6 and 4.7).

Importantly, these results highlight that the active core of the photocatalyst is not interacting with the polymer backbone and its catalytic properties are not affected by the incorporation in the polymer chain.

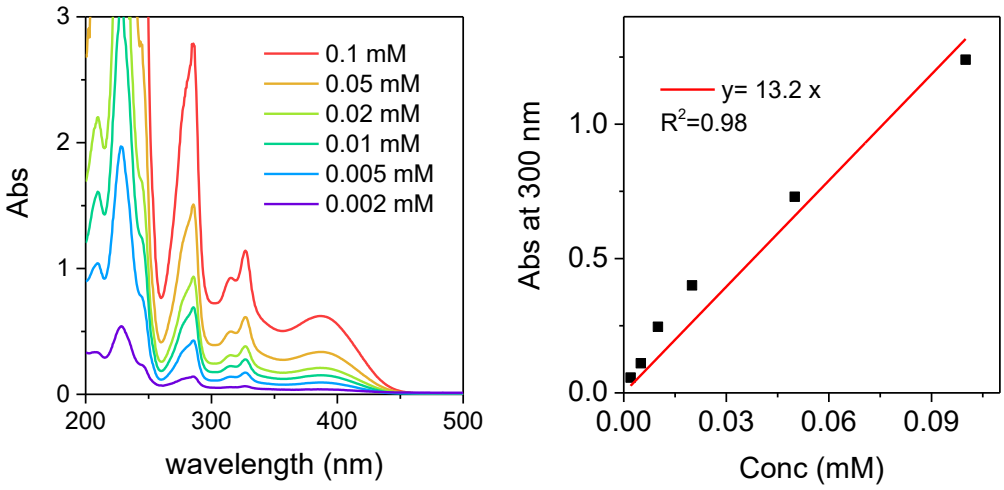

***Figure 2.4**: On the left the absorption spectra at different concentration of the monomer 3CzIPN-A (**11**) in ACN. On the right the calibratin line built taking the absorbance values at 300 nm.*

Conversely, the lifetime of the excited state changed significantly (*S.I.* 4.6.3). Indeed, for p(OEGA-*co*-3CzIPN-A) it was measured a time of 14.2 ns for the prompt fluorescence and 1450 ns for the delayed fluorescence due to the TADF behaviour. The latter is much longer than the corresponding lifetime of the monomer (**Table 2.4**).

***Table 2.4**: Lifetime of prompt fluorescence measured with TCSPC and delayed fluorescence measured with MCS technique. All the measurements reported were performed in ACN degassing the solution with N_2.*

	4CzIPN	**3CzIPN-A**	**Polymer**
Prompt fluorescence	18.7 ns	10.5 ns	14.2 ns
Delayed fluorescence	1390 ns	255 ns	1450 ns

We can hypothesize that the observed enhancement in the lifetime is associated with the structural change apported by the incorporation of the photocatalytic units within a quite hindered polymer chain. The structural modification implied a change of the HOMO and LUMO orbitals associated with the photoactive monomer, thus bringing beneficial effect on the elongation of the lifetime. Recent studies have shown that the polymerization of fluorescent monomers can extend the lifetime of the material or, in some cases, induce TADF behaviour. However, this effect is typically associated with the conjugation of the monomer within the polymer chain.[140] On the contrary, in this work the component responsible for the TADF is located in a side chain rather than being directly integrated into the polymer backbone.[134] Future DFT calculation may further support this result.
At this point, it was crucial to understand if the copolymerized photocatalyst was able to catalyse photoreactions.

2.4 Test of photocatalytic activity

The benchmark photoreaction selected for this target is a Giese-type radical addition, which involves the addition of radical intermediates to versatile Michael acceptors. Carboxylic acids are particularly attractive as radical precursors due to their availability, low cost, diversity, and sustainability. Furthermore, the corresponding nucleophilic carbon radical can be readily obtained through a favourable radical decarboxylation process, which releases CO_2 as a traceless

by-product (see **Scheme 2.1**).[141] Therefore, a proline derivative **13** was used as the radical precursor, and dimethyl maleate **15** served as the Michael acceptor (the procedure is detailed in section 4.3: *Procedures*).

Giese addition provides a viable alternative for the formation of new C-C bonds via addition to alkenes, avoiding traditional methods that generally involve the use of metal-based catalysts, often toxic, difficult to synthesize, and unstable.

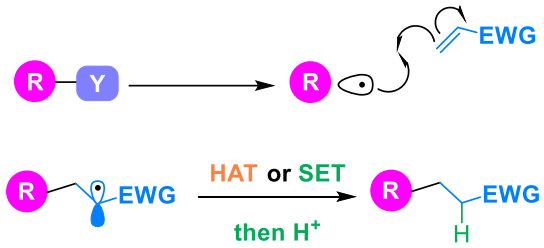

***Scheme 2.1**: General scheme of a Giese-type addition. The first step involves the formation of a radical from a precursor that will consequently add to a Michael acceptor. It is common to find carboxylic acids as precursors (R-Y where Y=COOH).*

The photocatalytic cycle of this reaction proceeds via reductive quenching for the formation of the radical precursor **14** through decarboxylation. The generated radical adds to the electron-deficient olefine **15** to generate a second radical species **16** that closes the photocatalytic cycle forming the anion **17**. The final product **18** is obtained upon protonation.

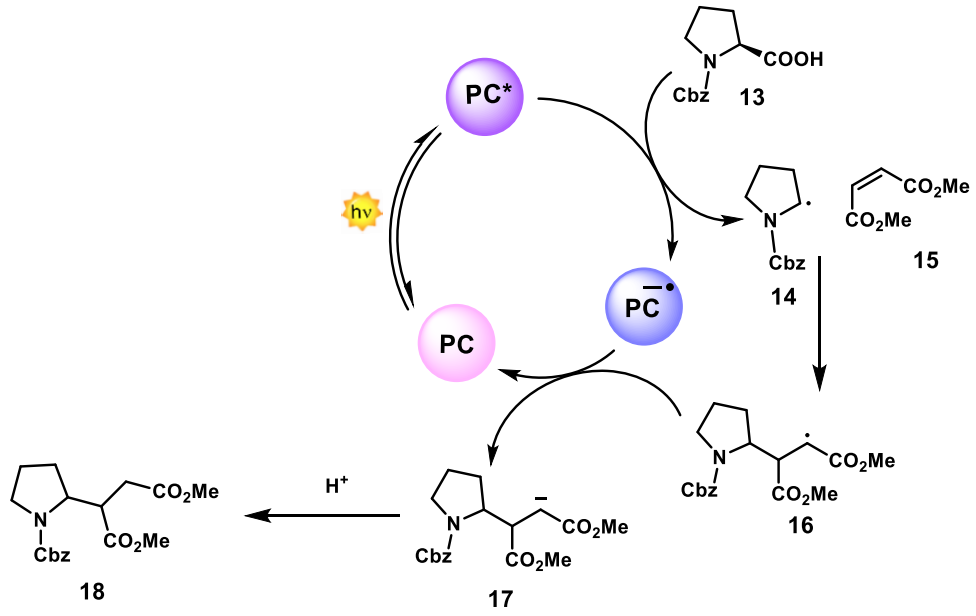

***Scheme 2.2**: Photocatalytic cycle of Giese-type radical reaction with the substrates of interest.*

This reaction was tested both with the reference photocatalyst **6** and with the potential photoactive polymer **47** in DMF, charging different loadings of the catalyst (from 1 to 5 molar %). The results are reported in **Table 2.5**.

***Table 2.5**: [1]H-NMR yields of Giese-type photoreactions calculated using trimethoxybenzene as internal standard (S.I. 4.5). The reactions were carried out overnight using a 427 nm Kessil at 100% intensity.*

PC	Catalyst loading	Solvent	NMR Yield
4CzIPN	5 mol%	Dry DMF	85%
P(**OEGA**-*co*-**3CzIPN-A**)	5 mol%	Dry DMF	90%
P(**OEGA**-*co*-**3CzIPN-A**)	2 mol%	Dry DMF	80%
P(**OEGA**-*co*-**3CzIPN-A**)	1 mol%	Dry DMF	80 %
No catalyst	0 mol%	Dry DMF	0 %

The product was not detected in the crude of a control reaction performed in the absence of a photocatalyst. This result implies that the use of the photocatalyst is crucial. Relevantly, the comparison of the copolymer with 4CzIPN **6** indicated that the change in the structure and the copolymerization did not alter the photocatalytic activity.

A similar reaction in water was tested since one of the possibility offered from this system is to solubilize the not-soluble organic photocatalyst in water giving access to a new reactivity for IPN based PCs (**9**). For this target a similar version of the previous reaction was tested (**Scheme 2.3**). The idea was to change the Michael acceptor with the respective dicarboxylic acid **19** in order to obtain all water-soluble reactants.

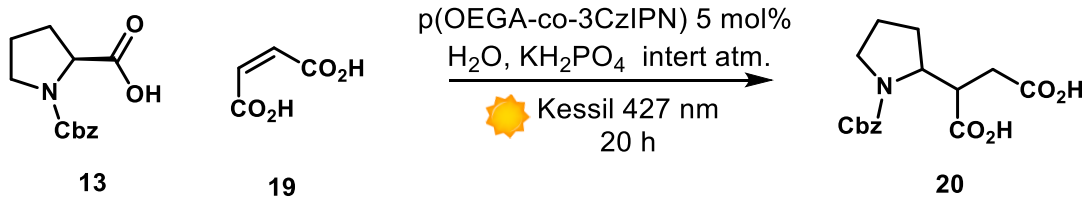

***Scheme 2.3**: Giese-type reaction using water soluble reactants. The reaction was carried out overnight (20h) and using a 5 molar% loading of the copolymer p(OEGA-co-3CzIPN-A). The detailed procedure is reported in section 4.3.*

Unfortunately, the product **20** was not detected for this reaction, just starting materials were recovered. Another reaction was tried with the formation in situ of a water soluble sulfonium salt **21** with a consequent C-C coupling with a pyrrole **22** (**Scheme 3.4**).[122] However, the reaction yield was very low.

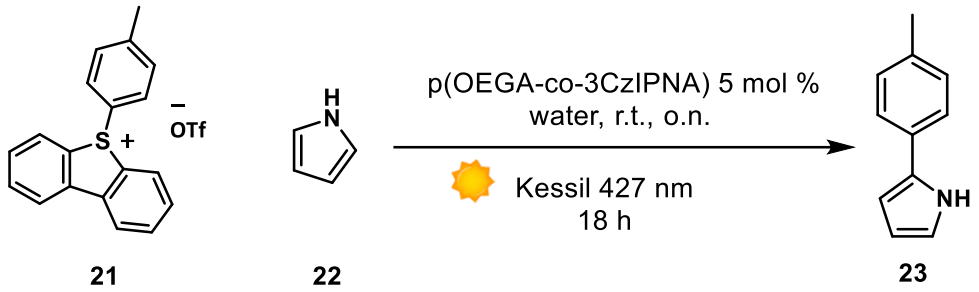

***Scheme 2.4**: Photo catalysed arene CH-CH coupling using pyrrole and a water soluble sulphonium salt (**21**). The reaction was carried out overnight (18h) and using a 5 molar% loading of the copolymer p(OEGA-co-3CzIPN-A). The detailed procedure is reported in section 4.3.*

For this reason, reactions in water have been set aside to make way for recyclability tests. Nevertheless p(OEGA-*co*-3CzIPN-A) is soluble in water, unlike 4CzIPN (**6**) and 3CzIPN-A (**11**), which, in principle, allows for working in water. Further testing will be needed in the future to fully explore its potential and assess its effectiveness in aqueous environments.

2.5 Recyclability tests

After the confirmation that the photocatalyst-incorporating copolymer was capable of catalyzing the Giese addition, the next step consisted of establishing a protocol for its recovery and testing its reuse. Firstly, the Giese-type reaction was optimized in terms of time and light intensity. The reason behind this screening was to irradiate as little as possible the photocatalyst trying to limit its degradation,[142] without compromising the reaction yield (**Table 2.6**).

***Table 2.6**: All the reactions reported were performed using 5 mol% of catalyst loading, where the PC used for the optimization is the 4CzIPN **6**. The time screening reactions are highlighted in violet, while the concentration screening in yellow. The light source used was a Kessil lamp (427 nm) positioned at a 3 cm distance from the reaction vessel. The NMR yield was calculated using trimethoxybenzene as internal standard.*

Entry	Time	Lamp intensity	^{1}H-NMR yield
1	20 h	100%	90%
2	4 h	100%	90%

3	3.5 h	100%	85%
4	2 h	100%	45%
5	1 h	100%	25%
6	3.5 h	75%	80%
7	3.5 h	50%	80%
8	3.5 h	25%	80%

The optimal conditions in terms of time and light intensity were established as 3.5 h and 25%, respectively. These conditions were then used for the recyclability tests. The reaction was performed using, p(OEGA-*co*-3CzIPN-A) as photocatalyst in two different loadings. After the reaction the polymer was precipitated, purified and reused. The results are reported in **Figure 2.5**.

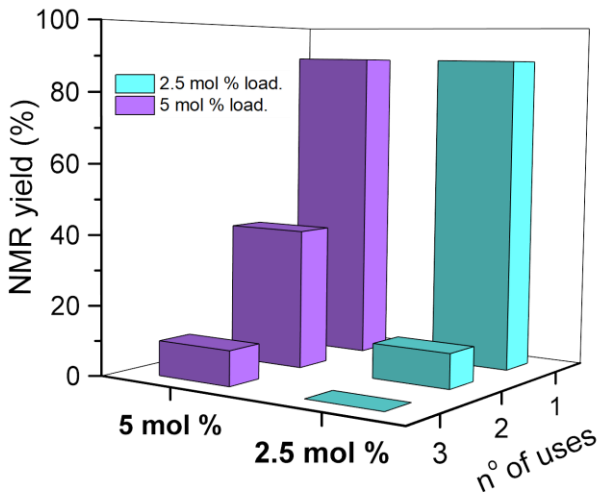

***Figure 2.5**: [1]H-NMR yields of the catalyst reuses in the Giese-type addition. The reactions were performed in the optimized condition using p(OEGA-co-3CzIPN-A) as photocatalyst. The yields were calculated using trimthoxybenzene as internal standard.*

While the product yield in the first reaction was very high, 90%, regardless of the catalyst loading, the yield dramatically decreased already at the second reutilization. The decrease was lower for higher catalyst loading. These results suggest that the photocatalyst is degrading during the reaction and this degradation hindered its activity. In order to prove the degradation, an aliquot of polymer was taken after each reaction to register the absorption spectra. It is visible in **Figure 2.6** that the spectrum shape is significantly changing after consecutive uses, showing the loss of the peak at higher wavelengths.

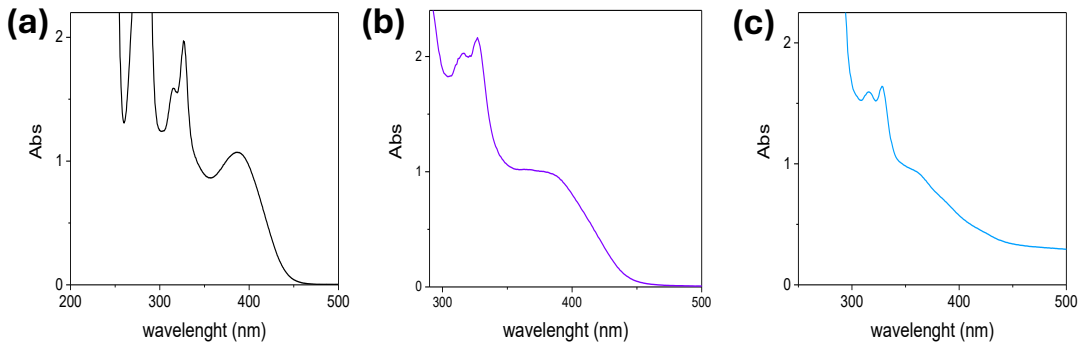

***Figure 2.6**: The spectra reported are normalized on the last maximum that they show respectively. a) UV-vis spectrum of p(OEGA-co_3CzIPN-A) before use. b) UV-Vis spectrum of the recovered polymer after one use. c) UV-vis spectrum of the recovered polymer after the second use.*

The progressive disappearance of this peak may be attributed to the substitution at the IPN core, as it was already reported by König's group, that can take place when the formation of some radicals occurs. In particular, it was determined that carboxyl radicals can replace a -CN group in the 4CzIPN.[143] Other studies about the degradation of IPN PCs (**9**) in reductive quenching processes are reported from *Zhang et al.* in 2016, Kwon's group, and Zeitlers's group in 2018.[142]

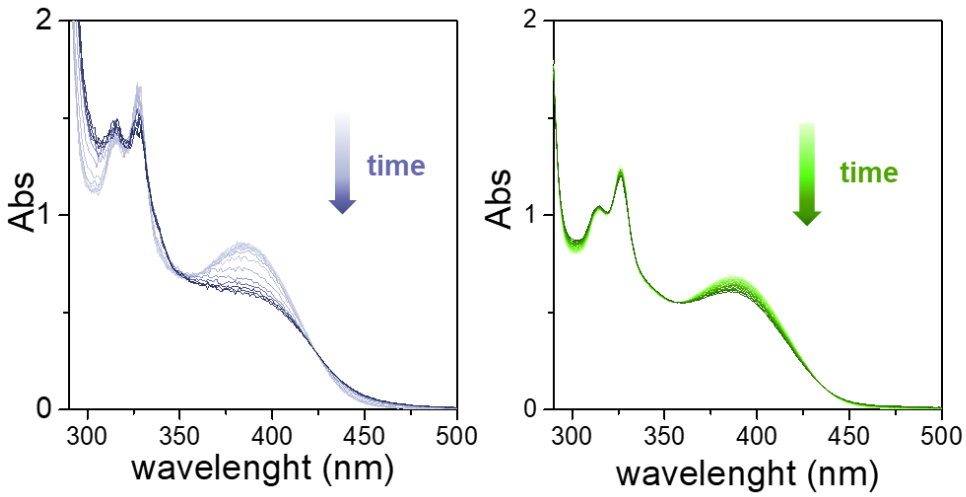

***Figure 2.7**: Degradation studies of p(OEGA-co-3CzIPN-A) dissolved in the pure solvent under light irradiation. Both kinetics were performed by irradiating the cuvette from the top with an optical fibre setting λ_{max} = 225 nm. The overall irradiation time was 3 hours taking a spectrum each 10 minutes, for a total of 18 acquisition for every test. On the left the results in DMF, on the right the degradation in ACN.*

Kinetics were performed in order to understand if the solvent was playing a role in the degradation. However, as already asserted in Section 1 (*Supported systems*), there is not a strict correlation between the behaviour of the irradiated catalyst (p(OEGA-*co*-3CzIPN-A) in this case) in pure solvent and the actual

behaviour under reaction conditions. Nevertheless, from the UV-Vis absorption kinetics we can derive that DMF is not the ideal solvent for the recyclability of the system as the catalyst degradation is very pronounced. On the other hand, the degradation was much less evident in ACN (**Figure 2.7**).

While from these studies it is not possible to anticipate the exact behaviour under reaction conditions, they emphasize that degradation can occur in very short times, especially in DMF with evident signal change in only 3 h (**Figure 2.7**).
For this reason, the optimization of the reaction time, set at 3.5 hours, is not sufficient to limit this drawback. Thus, the Giese addition reaction was repeated using ACN instead of DMF with a 5 mol% loading of the catalyst, giving a good ^{1}H-NMR yield about 80%. However the UV-Vis spectrum of the polymer after reaction showed its complete degradation (*S.I.* 4.6.1), indicating that the choice of solvent is not the sole parameter affecting the stability of the photocatalyst. A kinetic study in ACN in the presence of the Cbz-protected proline **13** and the inorganic base K_2HPO_4 confirmed that degradation occurred in these conditions (*S.I.* 4.6.1).

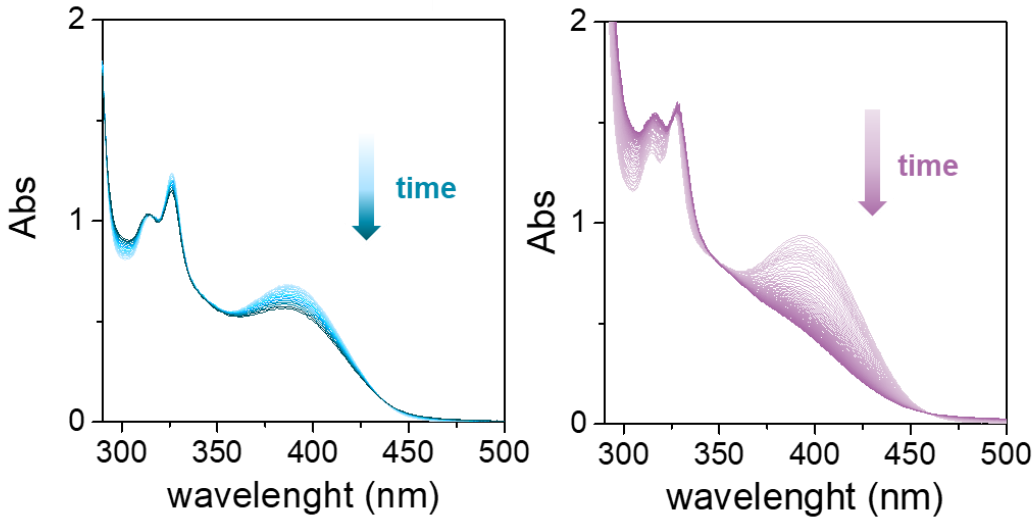

***Figure 2.8**: UV-vis degradation studies in water of p(OEGA-co-3CzIPN-A) using a 425 nm optical fibre on the top of the cuvette and taking a spectrum each 10 minutes. On the left, the irradiation of the photoactive polymer in the pure solvent (water) is showed. On the right, Cbz-Pro-OH (**13**) and HK_2PO_4 are added in the water making possible the formation of radicals. The reactants are added maintaining the same ratio used for the Giese-type reaction previously tested.*

Similarly, the behaviour of the copolymer was tested in water. In this case the kinetic was performed in 3 different situations: i) pure water, ii) water with added

K_2HPO_4 (the base used in the Giese-type addition), and iii) water with Cbz-Pro-OH (**13**) and KH_2PO_4. Results are reported in **Figure 2.8** and (*S.I.* 4.6.1)

The polymer irradiated in pure water shows relatively good stability, which is maintained when K_2HPO_4 is added to the solution (*S.I.* 4.6.1) indicating that the basic environment as minimal influence on the photocatalyst stability. However, once the base that deprotonates the carboxylic functionality and induces the formation of the radicals (**Scheme 2.2**) is added the stability is lost (**Figure 2.8**).

As mentioned above, the poor stability of IPN PCs (**9**) can be associated with the substitution of cyano groups by photogenerated radical species in solution, as reported by König. Nevertheless, those "degraded" species were determined to be still active as photocatalysts,[144] contrary to what was observed during the experiments described herein. We can suppose that one of the problems lies in the wavelength of the light used (λ_{max}=427 nm) that is slightly absorbed from the substituted form of the catalyst used in this work after degradation. This aspect will be the subject of future studies.

Another photoreaction was then investigated, in search of more suitable conditions to avoid the degradation of the catalyst.

Povarov-type reaction was chosen. It is a [4+2] cycloaddition generally starting from the formation of reactive intermediates such as iminium ions and enamine radicals, which then undergo cycloaddition to produce complex heterocyclic structures. In this specific case, the substrates chosen were the *N,N*-dimethylaniline (**24**) and *N*-phenylmaleimide (**27**).

The reaction was tested at different times, namely 4, 6, 8 and 18 hours. Similar outcomes were measured at each reaction time, with product yield of around 40% (**Figure 2.9**).

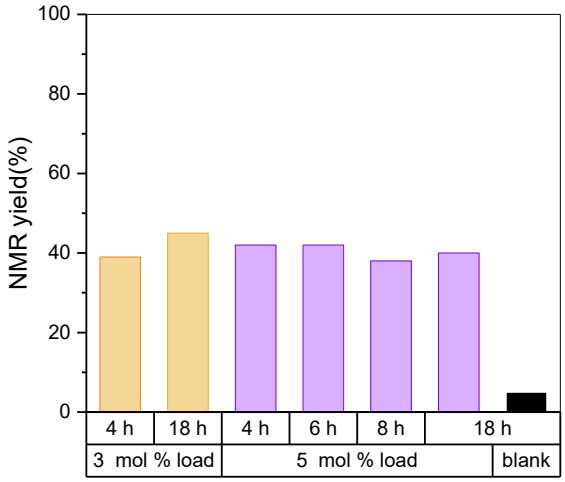

***Figure 2.9**: [1]H-NMR yields of Povarov-type reaction carried out at different times. The photoactive polymer was used as photocatalyst in 5 mol % loading (highlighted in violet) and 3 mol% (in grey). The reactions were performed in a non-degassed vial using a 427 nm Kessil at 25% intensity at 3 cm distance.*

From the crude of the reaction performed for 4, 6, or 8 h it was possible to still observe a big amount of the limiting starting material. Neverthless, running the reaction for longer times resulted in the disappearing of the starting material, without improvement in the overall yield. Initially, this problem was associated with the consumption of oxygen. Indeed, it is reported that the photocatalytic cycle in photo-Povarov type reactions requires the presence of oxygen (showed in **Scheme 2.5**). The reaction was then set up in open vials (**Figure 2.10**), or adding an oxygen balloon on top. Despite these changes, the yield remained around 40%.

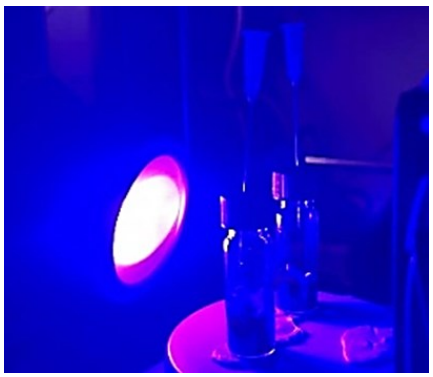

***Figure 2.10**: Set up for the Povarov-type reaction. 4 mL vials were used, placing a needle on top to allow the continuous entry of oxygen.*

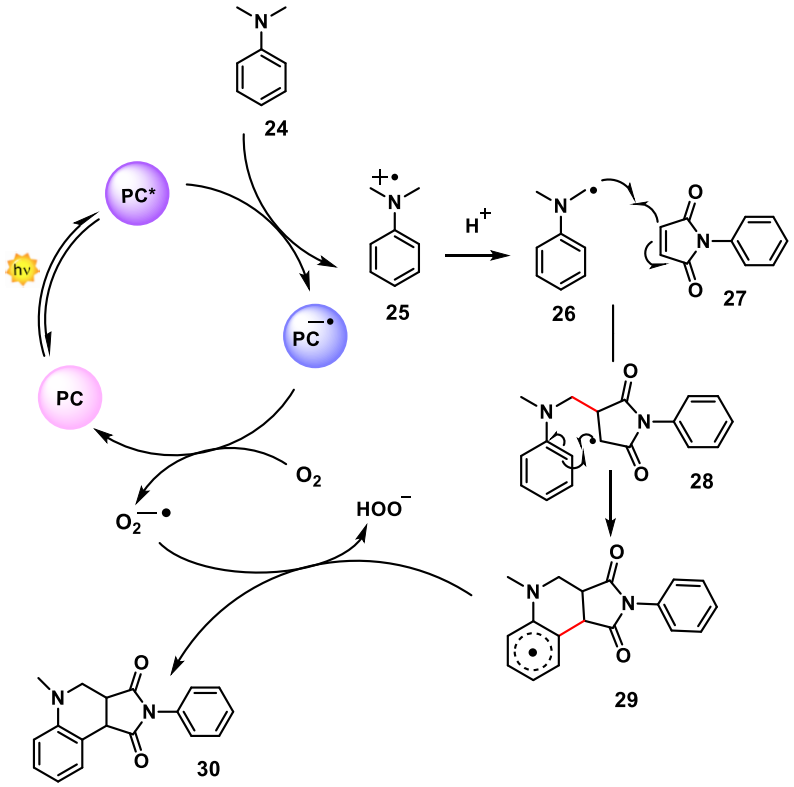

***Scheme 2.5**: Reported mechanism of Povarov reaction. The PC is restored in its ground state thanks to the presence of oxygen.*

However, recyclability of the photocatalyst was tested also for this reaction. The minimum time (4h) was chosen in order to limit the total hours of irradiation, and the catalyst loading was 3 mol%. The ^{1}H-NMR yields obtained for the several consecutive usages are reported in **Figure 2.11**.

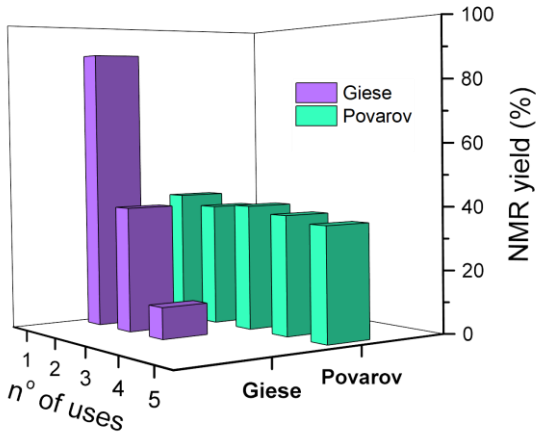

***Figure 2.11**: In green ^{1}H-NMR yields of the catalyst reuses in the Povarov-type addition. The reactions were performed in 4 h under optimized conditions using p(OEGA-co-3CzIPN-A) as photocatalyst (3 molar %). The*

yields were calculated using trimethoxybenzene as internal standard. In purple the previous results of the Giese-type reaction with 5 molar % of catalyst loading.

Very positive results have been observed since the catalytic performance of the photoactive polymer remains basically unchanged after each use for 5 consecutive reactions. It is concluded, therefore, that it is possible to find optimal conditions for the reuse of the copolymer catalyst.

Furthermore, at the end of each reaction, the absorption spectrum of the polymer was recorded. As shown in **Figure 2.12**, with exception of the first usage, this remains practically unaltered after each use. For this reason, we believe that even after the fifth cycle, the polymer would be able to continue performing efficiently even if further cycles were not tested. These results indicate that the incorporation of photocatalysts within polymer chains is an effective strategy to enable its recovery and recycling. However, it remains necessary to find better conditions to improve the yield of a Povarov reaction, and/or to establish different reactions in which the polymer shows a better performance, namely achieving high yields.

After that, to proceed towards the ultimate goal of supporting the catalyst on silica particles, it was necessary to establish the conditions for the growth of the polymer from the surface.

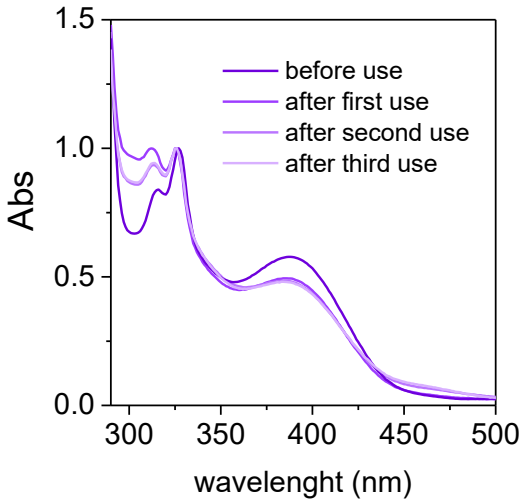

***Figure 2.12**: UV-vis spectra of the polymer before usage and after the first, second, and third usage. The spectra reported were registered in ACN. The amount of polymer used for each spectrum was not identical, and all the spectra were normalized at 325 nm.*

2.6 Surface functionalization

Surface-initiated ARGET-ATRP was the method chosen for the functionalization of the silicon surfaces with polymer brushes. Namely the grafting from technique was exploited, starting from the immobilization of the initiator on the activated surface and the subsequent growth of the polymer brushes as described in section 4.3 (*Procedures*).

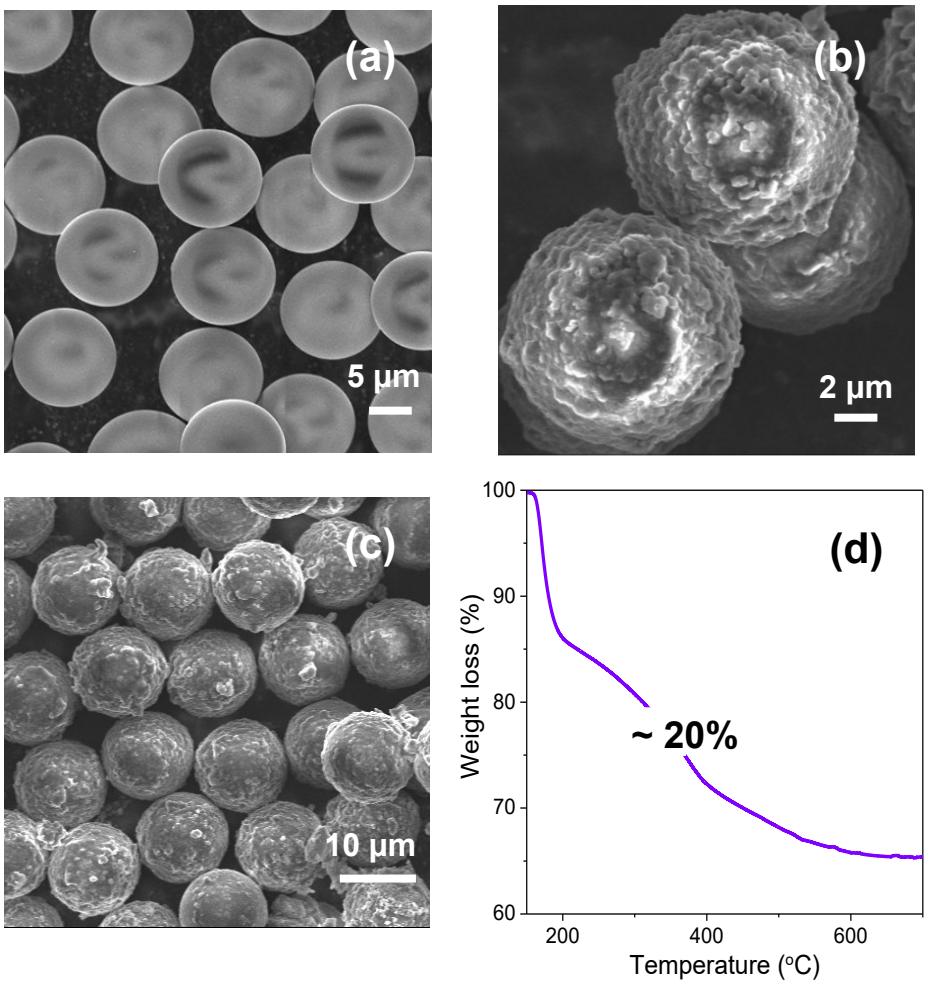

***Figure 2.13**: SEM pictures of a) the bare silica particles, before functionalization; b) POEGA-g-SiO_2 after functionalization displaying a thin shell; c) zoom out of the particles after functionalization to underline the l homogeneity; d) thermogravimetric analysis result showing a loss of weight of about 20% corresponding to the organic coating.*

Initially, 10 µm diameter, monodisperse, non-porous SiO_2 particles were functionalized with ATRP initiating sites, then used to grow brushes following the same procedure that was implemented in solution with the OEGA monomer. Micron-scale particles were chosen to facilitate the separation after use. During

the SI-ARGET-ATRP process, no free initiator in solution was added, so that polymer chains could only grow from the previously functionalized particles. The obtained particles were homogeneously functionalized as observed by scanning electron microscopy (**Figure 2.13b and 2.13c**), and they showed a weight loss of around 20% from the thermogravimetric analysis (TGA) (**Figure 2.13d**).

For this reason, the same procedure was then applied for the copolymerization of OEGA with **11** (3CzIPN-A) from the particles' surface. However, the particles functionalized with the copolymer showed a lower weight loss (around 13%) from the TGA (*S.I.* 4.9). The estimation of the mmol of photocatalyst per mg of particles by means of the emission calibration (*S.I.* 4.6.2) resulted in a very low amount of photocatalyst, namely 2.4 x 10^{-6} mmol per mg of particles. This result was not considered acceptable because it would have implied a significant loading of particles within the photoreactions to reach the typical loading employed with molecular photocatalysts, and consequently a high amount of solid support. It was concluded that this configuration is not suitable for a photoreaction as the light scattering would be too high, preventing the diffusion of light and lowering the efficiency of the system. The use of such a setup would be counterproductive for reactivity.

From this result arose the need to optimize the growth of brushes from the surface, to increase the thickness of the brush shell and consequently the amount of polymeric material comprising the photoactive moiety. If longer chains could be achieved, then the amount of photocatalytic units per milligram of particle would increase, thus the loading of solid support in photoreactions could be diminished, limiting the scattering of the light. For ease of characterization and handling, the optimization of polymer brush thickness from SiO_2 substrates was conducted on flat surfaces. It should be noted that, from a molecular point of view, a flat surface can be a good approximation for spherical particles with a diameter of 10 µm.

2.6.1 Optimization on flat silicon substrates

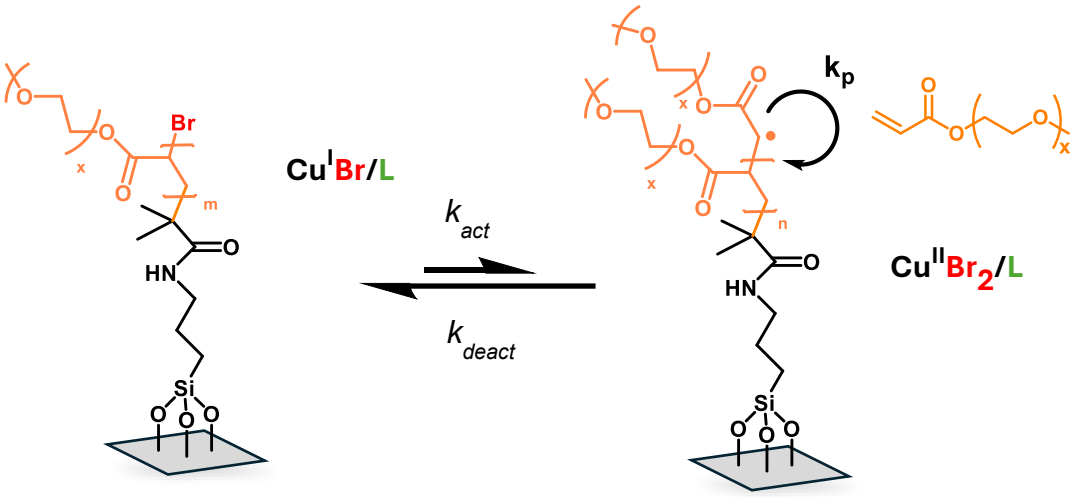

***Figure 2.14**: schematic representation of ATRP equilibrium showing the growth of the polymer (PEGA) from the initiator (APTES+BiBB) immobilized on flat silicon substrates.*

The first attempt was to reproduce the same conditions previously tested for the particles, both to verify the growth of the brushes and to identify the starting point for optimization. For this purpose, the polymerization was conducted under the exact same conditions, carefully washing and drying the substrate after polymerization, in order to measure the dry thickness by ellipsometry. The measured brush thickness was ~10 nm. The optimization of SI-ARGET ATRP conditions involved various parameters of the polymerizations. The first step was to replace the mild reducing agent, $Sn(oct)_2$, with a stronger one, specifically sodium ascorbate (NaAsc).[145–147] Secondly, a percentage of water was added, as it is a highly polar solvent that can largely enhance the rate of ATRP.[148] Finally, the amount of Cu-based catalyst was reduced, particularly adjusting its molar ratio relative to the reducing agent. The most relevant experiments are reported in **Table 2.7**.

These results showed that decreasing the amount of Cu catalysts from 0.55 mM to 0.13 mM resulted in thicker brushes. A further decrease in the catalyst amount however did not generate a further increase in the thickness. Furthermore, by keeping constant the concentration of Cu, thicker brushes were obtained when the amount of NaAsc was decreased. In particular, the use of a Cu:NaAsc ratio

of 2:1, using a Cu concentration 0.13 mM and adding 10 vol% water provided a brush coating with dry thickness of 45-55 nm.

***Table 2.7**: SI-ARGET ATRP from flat silica substrates (about 1 cm x 2 cm) previously functionalized with the initiator following the procedure detailed in section 4.2 (Procedures). All the polymerizations were carried out in a 5 mL vial using a total volume of 5 mL. The ratio solvent:monomer is 3:1 (v/v) for all the experiments, degassing with argon for 30 minutes before adding the reducing agent from a degassed stock solution in water. All the experiments were run at 65 °C and have a duration of 4h during which the system was kept under argon overpressure. In the first raw, the initial conditions using $Sn(oct)_2$ are indicated.*

Entry	Solvent	$CuBr_2$/L (mM)	Cu:NaAsc (ratio)	Thickness (nm)
1	DMSO	0.56	1:2 ($Sn(oct)_2$)	10
2	DMSO + H_2O (10 vol%)	0.56	1:1	10
3	DMSO + H_2O (5 vol%)	0.31	1:1	18
4	DMSO + H_2O (5 vol%)	0.13	1:1	27
5	DMSO + H_2O (5 vol%)	0.07	1:2	25
6	DMSO + H_2O (10 vol%)	0.13	2:1	45-55

These results can be interpreted by considering that a smaller amount of the metal-based catalyst results in a lower concentration of radicals propagating during the growth of the brushes. This effect is further increased by using a defect of reducing agent, as it implies that the amount of Cu(I) activator being (re)formed is even more limited. Thus, both a lower concentration of Cu and of reducing agent results in a slower generation of radicals, which likely improves control over the process. Indeed, termination reactions are strongly decreased, and propagation can continue, thus thicker brushes can be obtained. The balance between Cu complex concentration and reducing agent is particularly critical in

this system for two main reasons: i) the solvent mixture is highly polar and therefore the activation of dormant species is rather rapid; ii) the amount of initiator, and thus of growing chains, is very low, as the initiator is only present on the functionalized surface.

A ~50 nm thickness of the brushes was considered sufficient, particularly considering that one possible drawback of a very thick shell could be the hindered diffusion of substrates within the brushes during the photoreaction. This would translate into an obstacle for the substrates in reaching the catalytic units closer to the particles' core, and consequently, into a decrease in the catalytic efficiency of the system.

The conditions used for Entry 6 will be the ones used for the functionalization of a new batch of particles.

2.6.2 Particles functionalization

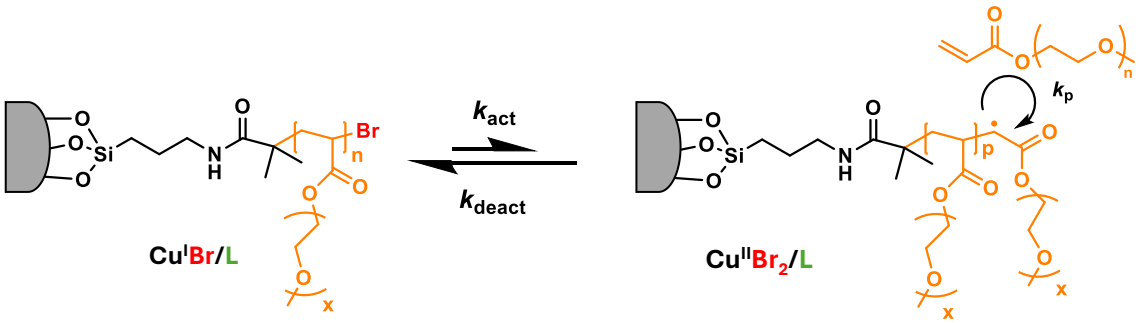

***Figure 2.15**: representation of ATRP equilibrium showing the growth of the polymer (PEGA) from the initiator (APTES+BiBB) immobilized on silica particles.*

Initially, micron-scaled particles were functionalized following the previously optimized procedure. The obtained particles were characterized with TGA and SEM (**Figure 2.16**). TGA showed a ~40% weight loss, confirming the actual optimization of the polymerization conditions to reach larger brush thickness. Additionally, SEM pictures confirmed the increment of shell thickness. However, homogeneity of the system decreased. Indeed, estimation of the functionalized particles' diameter with the software ImageJ showed particles practically without coating and others with a shell thickness that reached ~1 µm. This result was attributed to the presence of a substantial amount of water in the reaction mixture. Indeed, before functionalization the particles with the initiator are hydrophobic.

This can lead to the formation of clusters at the beginning of the process preventing the homogenous growth of the brushes.

However, since the amount of polymer grafted was elevated, the same conditions were then used for the copolymerization of OEGA with a 5 mol% of the monomer **11** (3CzIPN-A) to obtain **SiO_x**-*g*-p(**OEGA**-*co*-**3CzIPN-A**).

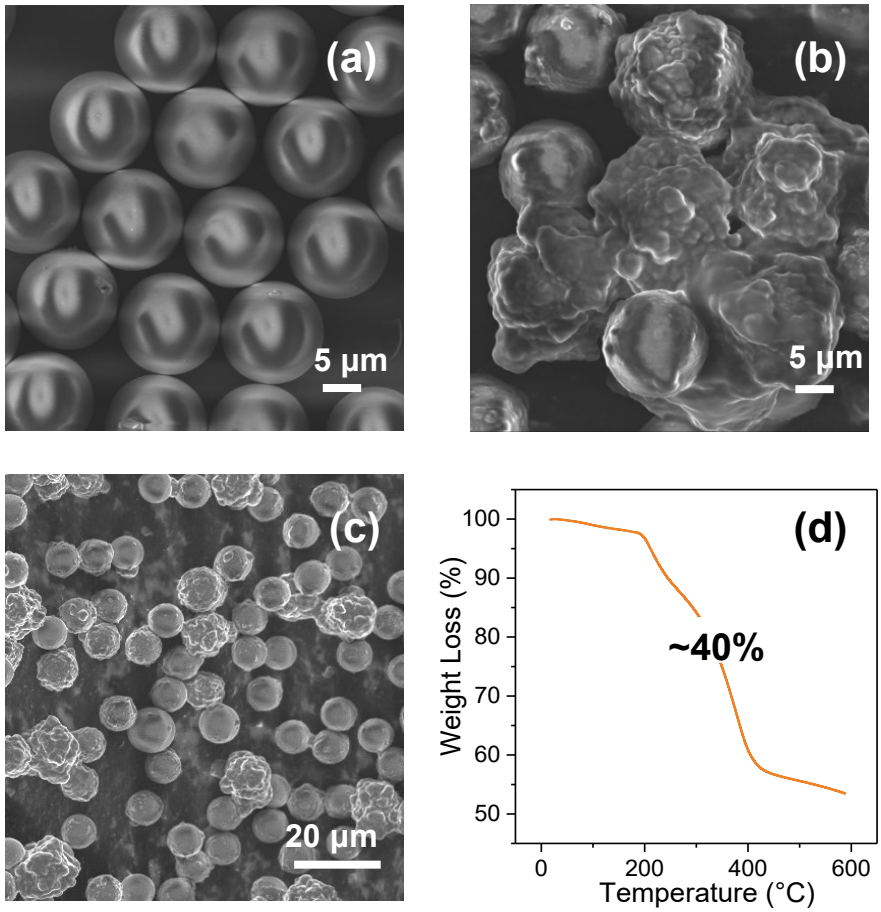

***Figure 2.16**: SEM pictures of a) the bare silica particles, before functionalization; b) POEGA-g-SiO_2 after functionalization displaying a thick shell; c) zoom out of the particles after functionalization to underline the loss of homogeneity with the new polymerization conditions; d) thermogravimetric analysis result showing a loss of weight of about 40% corresponding to the organic coating.*

In the meantime, new optimizations were carried out from flat substrates trying to avoid as much as possible the presence of water without compromising the final brush thickness. All the parameter described for previous polymerizations were maintained: the Cu catalyst, its ratio with the ligand Me_6TREN, NaAsc as reducing agent, DMSO as solvent and the total volume of 5 mL, however, a more concentrated solution of NaAsc in water was prepared as water was introduced in the system together with the reducing agent. When a 2 vol% of water was used,

a brush thickness of 46 nm could be obtained by using a polymerization solution 0.26 mM of Cu and 0.13 mM of reducing agent. Those conditions were also tested for ARGET-ATRP in solution, i.e., with EBiB **44** (as initiator and without SiO_x substrates, to check conversion and the photocatalyst incorporation, *S.I.* 4.8).

In addition, the functionalization of smaller particles was also performed using the same polymerization procedures and the last optimized conditions. Monodisperse, non-porous silica particles with a diameter of 200 nm were employed and characterized with SEM and TEM (*S.I.* 4.9) showing an homogeneous coating of all the particles. This result support the fact that the amount of water previously used was too elevated causing the formation of cluster during the synthesis.

Upon functionalization of these particles with the OEGA monomer, a weight loss of about 50% was measured by TGA (*S.I.* 4.9). This result highlights that the functionalization protocol is robust and can be applied to particles of different sizes. Moreover, the obtained core-shell particles could be easily precipitated out of reaction mixtures by centrifugation. Thus, even by employing particles with significantly reduced size, the ease of separating the system out of the reaction environment is retained.

2.7 Photocatalytic system

Once the photoactive particles were synthesized (*S.I.* 4.9), they were tested for the benchmark reaction. The amount of photocatalyst per milligram of particles was evaluated by calibrating the emission of p(OEGA-*co*-3CzIPN-A) from solution in DMF at different concentrations (*S.I.* 4.6.2). Using emission instead of absorption (as was done previously with the copolymer) became necessary because light scattering with the particles is too high to record absorption spectra, whereas emission is more suitable for this purpose as it is much less sensitive to scattering. It was estimated that for 1 mg of particles, the amount of photocatalyst was 3.6×10^{-5} mmol, that is a notable improvement compared to the first attempt resulted in 2.4×10^{-6} mmol per mg of particles. However, the amount of particles needed for a reaction under typical conditions was still very high. For this reason,

it was decided to use a low catalyst loading for the photocatalytic reaction, namely 1 mol% of photocatalyst. This amount should be sufficient since, as reported in section 2.4 (*Test of catalytic activity*), an analogous amount of the copolymer provided an 80% yield of the desired product.

55 mg of particles were inserted into the reaction environment and the reaction ran in the usual conditions (reported in section 4.3) resulting in a 30% yield, determined by ^{1}H-NMR. From this result, we can infer that the system works but with certain limitations that lead to a substantial decrease in yield. There could be multiple explanations for this. First, some of the catalytic units might be hardly accessible to the substrates because they are located too close to the particles' core. This leads to a decrease in the effective loading, which might be too low. To support this consideration, the reaction was conducted using the photoactive polymer with a loading of 0.5 mol% of photocatalytic moiety. Even in this case, a significant drop in yield was observed, decreasing to 40%. A second issue could be related to light scattering, which reduces light penetration within the system. If scattering is a problem for the system, repeating the reaction with higher particle loadings would not be beneficial, as it would significantly increase the light diffusion. For this reason, with the intention of minimizing the amount of inorganic support as much as possible, it was decided to switch to nanometric particles, specifically with a diameter of 200 nm for future tests.

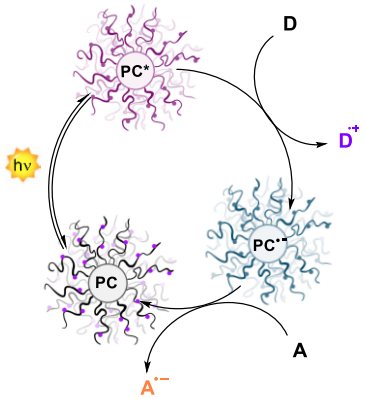

***Figure 2.17**: General graphic representation of a reductive quenching using the photocatalytic particles as photocatalyst.*

3. Conclusions and outlooks

The main goal of the research was to develop photocatalytic systems that are both easily recoverable and reusable. Specifically, the project focused on creating polymeric materials—initially in solution and then supported on inorganic particles—that incorporate photocatalytic units directly copolymerized within the polymer chains. The benchmark photocatalysts in this study are IPN-based photocatalysts, selected for their considerable versatility and their unexplored potential regarding recyclability.

A polymerizable IPN PC was synthesized and evaluated for its emission, absorption, redox potentials in the excited state, and lifetime. The analysis of lifetime was particularly noteworthy as it confirmed the compound's TADF (thermally activated delayed fluorescence) behaviour, which is characteristic of IPN PCs.

The photoactive monomer was successfully copolymerized with an amphiphilic monomer using ARGET ATRP yielding the copolymer poly(OEGA-co-3CzIPN-A). The copolymer exhibited similar behaviour to the original PC but with a significantly extended delayed fluorescence lifetime. Photocatalytic testing in two different reactions showed that the copolymer performed excellently in a Giese-type photoreaction with high product yield, although it degraded too rapidly for effective reuse. In contrast, in a Povarov-type cyclization, the copolymer produced a lower yield of about 40% but showed greater stability over multiple reuse cycles, indicating that, under favourable conditions, catalyst recycling might be achievable. Attempts to conduct reactions in water were less successful, as they did not meet the expected outcomes.

The second phase of the project focused on optimizing polymerization on silicon flat surfaces using the SI-ARGET ATRP *grafting-from* technique. These optimized conditions were successfully applied to initiator-functionalized micron-sized silica particles, leading to the development of a supported catalytic system. This system was tested in a Giese-type reaction, resulting in a 30% yield. This results, despite

the lower yield, marked a significant step toward reusable photocatalysts, key focus of this project.

Clearly, there are still several things that need to be addressed. First and foremost, it is necessary to find suitable conditions for recyclability that combine high yields with good stability of the photocatalyst. This step is not straightforward because, although there are studies on the degradation process of IPN PCs, the conditions under which degradation occurs are not well understood. Moreover, the fact that degradation is entirely dependent on the substrates and reaction environment makes this study even more complex. As has been shown, a catalyst that seems to degrade completely under irradiation in pure solvent can be stable within a certain catalytic cycle in the right conditions, and vice versa. Secondly, the final system also needs to be optimized. As shown, only one reaction attempt with the supported brushes has been made so far, and it revealed a significant decrease in the yield of the tested reaction.

Currently, the idea is to use smaller particles (200 nm in diameter) to increase the surface area and, consequently, the amount of organic content per milligram of particles. This would allow for higher catalyst loadings without increasing light scattering. Additionally, it might be possible to increase the percentage of catalyst within the brushes. If the problem of accessing the more internal catalytic units persists, an option would be to use gradient polymers with the catalytic units more concentrated toward the outer surface.

4. Supporting information

4.1 Materials

Commercial grade reagents and solvents were purchased from Sigma Aldrich, FluoroChem or BLDpharma and used as received, unless otherwise stated.

Oligo[(ethylene glycol) methyl ether acrylate] (OEGA) with M_n ~480 g mol^{-1} was purified by passing through a basic aluminium oxide column to remove the inhibitor (butylated hydroxytoluene, BHT) before use.

MilliQ water was purified with a Millipore Direct-Q 5 ultrapure water system or a Milli-Q® IQ 7003 purification system.

Surface modifications were performed on manually cut silicon wafers purchased from Si-Mat (Landsberg, Germany).

Non-porous, monodisperse silica particles of 10 µm and 200 nm diameter were purchased from Sigma Aldrich.

4.2 Instruments

NMR spectra were recorded on Bruker AVANCE Neo 400 Nanobay equipped with a BBFOATM-z grad probehead. The chemical shifts (δ) for ^{1}H and ^{13}C are given in ppm relative to residual signals of the solvents ($CHCl_3$ @7.29 ppm ^{1}H-NMR, 77.16 ppm ^{13}C-NMR, CH_2Cl_2 @5.32 ppm ^{1}H-NMR, 53.84 ppm ^{13}C-NMR, $(CH_3)_2CO$ @2.05 ppm ^{1}H-NMR, 29.84 ppm ^{13}C-NMR). Coupling constant are given in Hz. The following abbreviations are used to indicate the multiplicity; s, singlet; d, doublet; t, triplet; q, quartet; m, multiplet; bs, broad signal.

Chromatographic purification of products was accomplished using flash chromatography on silica gel (SiO_2, 0.04-0.063 mm) purchased from MacheryNagel, with the indicated solvent system according to the standard techniques. Thin-layer chromatography (TLC) analysis was performed on pre-coated Merck TLC plates (silica gel 60 GF254, 0.25 mm). Visualisation of the developed chromatography was performed by checking UV absorbance (254

nm). Organic solutions were concentrated under reduced pressure on a Büchi rotary evaporator.

Steady-state absorption spectroscopy studies were performed at room temperature on a Varian Cary 50 UV-vis double beam spectrophotometer; 10 mm and 1 mm path length Hellma Analytics 100 QS quartz cuvettes were used. Steady-state fluorescence spectra, lifetime studies were recorded on a Varian Cary Eclipse Fluorescence spectrophotometer; 10 mm path length Hellma Analytics 117.100F QS quartz cuvettes.

Thermogravimetric analysis (TGA) was carried out using SDT 650 by TA Instrument that exploits a horizontal dual-beam thermobalance and it is equipped with TRIOS software. The temperature was scanned from 200 °C with a ramp 10.00 °C/min to 600.00 °C.

Pictures of the functionalized particles were acquired with scanning electron microscopy (SEM). SEM was performed with a Zeiss Sigma HD microscope, equipped with a Schottky FEG source, one detector for backscattered electrons and two detectors for secondary electrons (InLens and Everhart Thornley). The microscope is coupled to an EDX detector (from Oxford Instruments, x-act PentaFET Precision) for X-rays microanalysis, working in energy dispersive mode. The samples were put on carbon tape for the analysis and the pictures acquired at 5 kV with in-lens detector.

Size exclusion chromatography (SEC) was performed using an Agilent Viscotek 302-TDA gel permeation chromatography equipped with a refractive index (RI) detector, a GRAM pre-colum (50x8, 10 um) and two GRAM analytical linear columns (300x8 mm, 10 um) from Agilent PSS connected in series to determine the number average molecular weight (M_n) and dispersity ($Đ$) of polymers. The column compartment and RI detector were both at 60 °C, and the eluent used was DMF containing 10 mM LiBr at a flow rate of 1 mL/min. Every sample (polymer concentration ~2 mg/mL) was prepared by filtering through neutral alumina over a PTFE membrane with a porosity of 0.20 μm. The column system was calibrated with 12 linear poly(methyl methacrylate) standards (M_n = 540–2,210,000 Da).

Thickness measurements were performed with a variable-angle spectroscopic ellipsometer from Semilab ZRt (Semilab SE2000). Ellipsometric data (*i.e.*, Ψ and Δ plotted towards beam wavelength) was recorded at an incident angle of 70° and wavelength range of 275–990 nm at room temperature. Before each analysis, polymerized wafers were rinsed with EtOH and carefully dried with nitrogen. For each substrate, a minimum of three points was taken for the measurements. The resulting spectra were fitted with the in-suite SEA software, using a four-layer Si/SiOx/polymer/air model.

Purification of the polymers was done using 12-14 kD Spectra/Por® dialysis membranes.

The potentiostate used for the calculation of the redox potentials is VIONIC powered by INTELLO software from Metrohm Autolab. The measurements were done in a 3-electrode cell. Platinum wire (99.9%) ST 0.6/40 mm was used as auxiliary electrode. The working electrode was a glassy carbon, 70 mm long and 2 mm diameter (body diameter 6 mm), and a Ag/Ag^+ non-aqueous refillable reference electrode (6 mm diameter).

The morphology and microstructure of the samples were characterized by transmission electron microscopy (TEM) and high-angle annular dark-field (HAADF) scanning transmission electron microscopy (HAADF-STEM) using TEM JEOL F200.

4.3 Procedures

4.3.1 Synthesis of the photoactive monomer (3CzIPN-A)

The initial phase of the synthesis focused on obtaining a photoactive molecule modified with a triethylene glycol chain. To achieve this, two distinct synthetic pathways were explored: a one-pot synthesis, commonly employed for the substitution of IPNs at the fourth position, and a two-step approach that involves isolating the intermediate compound. Both methods successfully produced 3CzIPN-TEG **34**. These pathways were compared to determine the most efficient process, specifically aiming to identify the synthesis method that could yield the

highest amount of the desired product, facilitating future scale-up. Finally, the synthesized compound was esterified to introduce a polymerizable functionality.

4.3.1.1 One pot synthesis

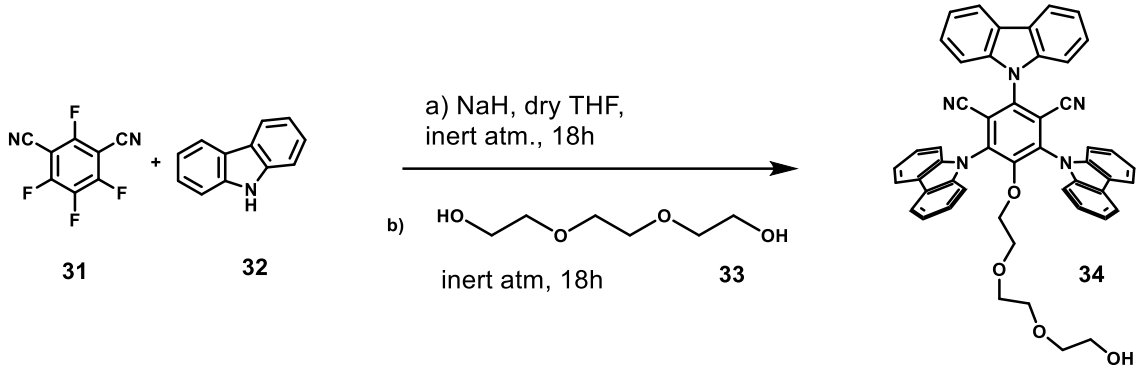

***Scheme 4.1**: Synthesis one pot of 3CzIPN-TEG.*

In a 100 mL shlenck the carbazole **32** (3.2 eq, 6.4 mmol, 1.07 g) was added and three cycles Ar/vacuum were performed. Under argon flow, 40 mL of dry THF were added and after NaH 60% (5.6 eq, 11.3 mmol, 451.2 mg of total weight and 270.8 of NaH). After 30 min tetrafluoroisophtalonitrile **31** was added (1 eq, 2 mmol, 400 mg) and left overnight under inert atmosphere. After 18h, triethylen glycol **33** (1.2 eq, 2.4 mmol, 0.3 mL) was added and stirred overnight. The solvent was then evaporated and the product **33** was isolated with an overall yield of 30% through flash chromatography (gradient DCM, DCM:EtOAc 9:1 and DCM:EtOAc 8:2). It was then characterized with ^{1}H-NMR and ^{13}C-NMR (*S.I.* 4.5).

4.3.1.2 Two steps synthesis

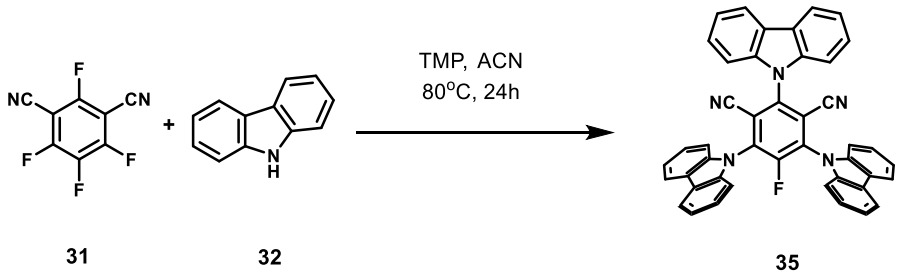

***Scheme 4.2**: Synthesis of the intermediate 3CzIPNF.*

In the first step the monofluorinated intermediate was isolated (3CzFIPN **35**).[121] Under stirring tetrafluoroisophtalonitrile **31** (1 eq, 5 mmol, 1g), tetramethyl piperidine (4.5 eq, 22.5 mmol, 3,8 mL) and carbazole **32** (3 eq, 15 mmol, 2.5g) were added in 30 mL of acetonitrile and let 24h at 80°C under reflux. The product

was isolated with flash chromatography (gradient DCM:EtOAc 4:1, 7:3, 1:1). The isolated product with a yield of 80% was characterized with ^{1}H-NMR, ^{13}C-NMR, ^{19}F-NMR (*S.I.* 4.5).

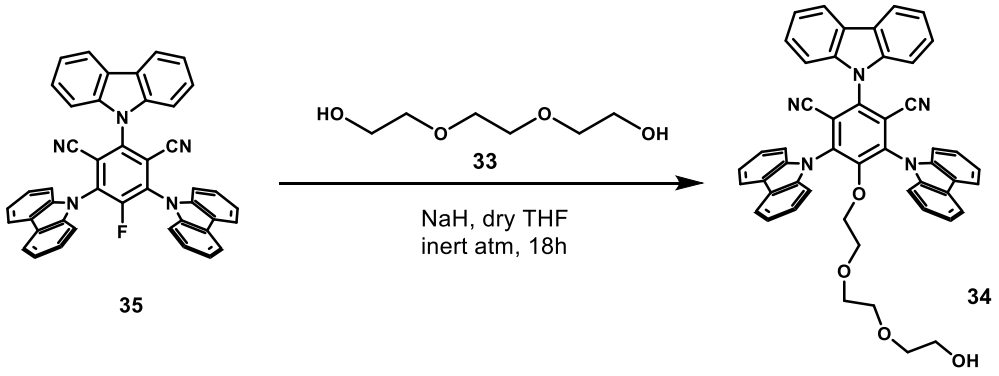

***Scheme 4.3**: Synthesis of 3CzIPN-TEG from 3CzIPNF.*

For the second step NaH 60% (1.5 eq, 5.8 mmol, 232 effective mg) was added and 3 cycles Ar/vacuum performed. Under inert atmosphere 130 mL of dry THF were put in the flask and then **33** (1.5 eq, 5.8 mmol, 0.78 mL) and **35** (1 eq, 3.9 mmol, 2.5 g). After 18h the solvent was evaporated and the product **34** isolated with flash chromatography (gradient DCM, DCM:EtOAc 9:1 and DCM:EtOAc 8:2). It was then characterized with ^{1}H-NMR and ^{13}C-NMR (*S.I.* 4.5).

4.3.1.3 Addition of polymerizable functionality

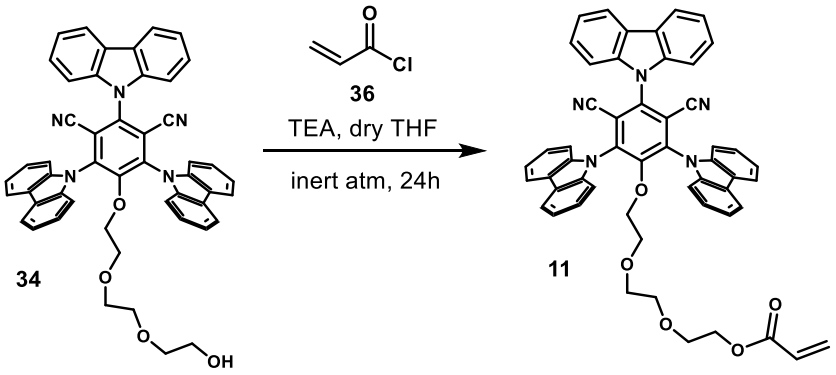

***Scheme 4.4**: Esterification of 3CzIPN-TEG with acryloyl chloride.*

Under inert atmosphere 3CzIPN-TEG **34** (1 eq, 0.3 mmol, 234 mg) was dissolved in 2 mL of dry THF. Then, triethylamine (1.2 eq, 0.36 mmol, 50 µL) was added dropwise and finally acryloyl chloride **36** (1.2 eq, 0.36 mmol, 30 µL). The reaction was stopped after 24h and extracted (adding DCM) with HCl 1M. After the

extraction the solvent was evaporated and the crude purified with flash chromatography (gradient DCM, DCM:EtOAc 9:1 and DCM:EtOAc 8:2) giving an isolated yield about 55%. The pure compound was characterized by ^{1}H-NMR, ^{13}C-NMR, lifetime measurements, absorption and emission spectra (*S.I.* 4.5 and 4.6).

4.3.1.4 Synthesis of reduced 3CzIPN-A

For characterization purposes, also a reduced version of the compound was synthesized (3czIPN-red, **12**).

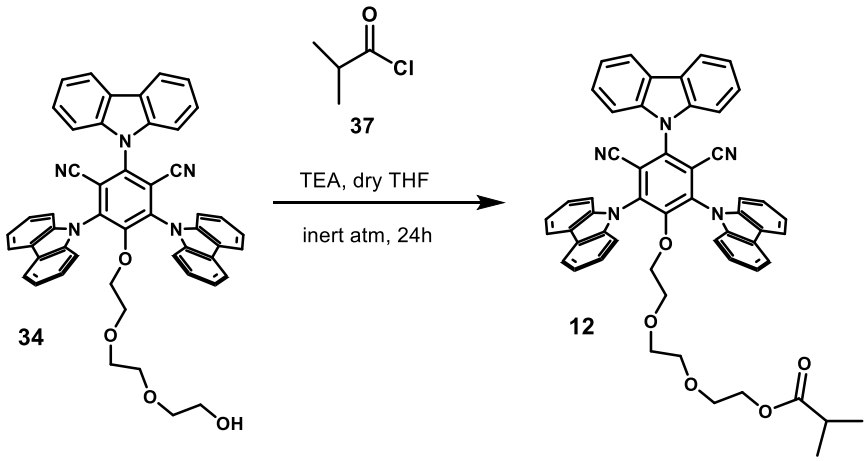

***Scheme 4.5**: Synthesis of the reduced version of the final monomer (3CzIPN-red).*

The procedure synthesis of **12** is identical to the preparation of **11** reported above replacing **36** with isobutyryl chloride **37**.

Under inert atmosphere **34** (1 eq, 0.3 mmol, 234 mg) was dissolved in 2 mL of dry THF. Then triethylamine (1.2 eq, 0.36 mmol, 50 µL) were added dropwise and finally **37** (1.2 equiv., 0.36 mmol, 38 µL). The reaction was stopped after 24h and extracted (adding DCM) with HCl 1M. After the extraction the solvent was evaporated and the crude purified with flash chromatography (gradient DCM, DCM:EtOAc 9:1 and DCM:EtOAc 8:2) giving an isolated yield about 55%. The pure compound was characterized by ^{1}H-NMR, ^{13}C-NMR, lifetime measurements, absorption and emission spectra (*S.I.* 4.5 and 4.6). This compound was specifically used for the calculation of the redox potentials with cyclic voltammetry (*S.I.* 4.7).

4.3.2 Functionalization of on SiOx Substrates

4.3.2.1 Flat surfaces

Silicon wafers were immersed in piranha solution (H_2SO_4 and H_2O_2, 3:1 v/v). After one hour, the substrates were rinsed with abundant MilliQ and EtOH, and dried under nitrogen. Cleaned oxidized wafers were placed in a desiccator for the chemical vapor deposition of (3-aminopropyl)triethoxysilane (APTES **38**, 0.3 mL). SiOx wafers were kept under vacuum for three hours in APTES atmosphere, then rinsed with MilliQ, EtOH, toluene and dried with N_2. APTES-bearing substrates (**39**) were placed in a flask with 30 mL DCM and a magnetic stirrer, where α-bromoisobutyryl bromide (BiBB **40**, 0.2 mL) and dry triethylamine (TEA, 0.2 mL) were added under nitrogen flow. The system was left stirring overnight at room temperature. The day after, the substrates with the grafted initiator (**41**) were first washed with abundant DCM, then dried and rinsed again with EtOH. Initiator-bearing wafers (**41**) were stored in a Petri dish to avoid contamination (**Scheme 2.6**).

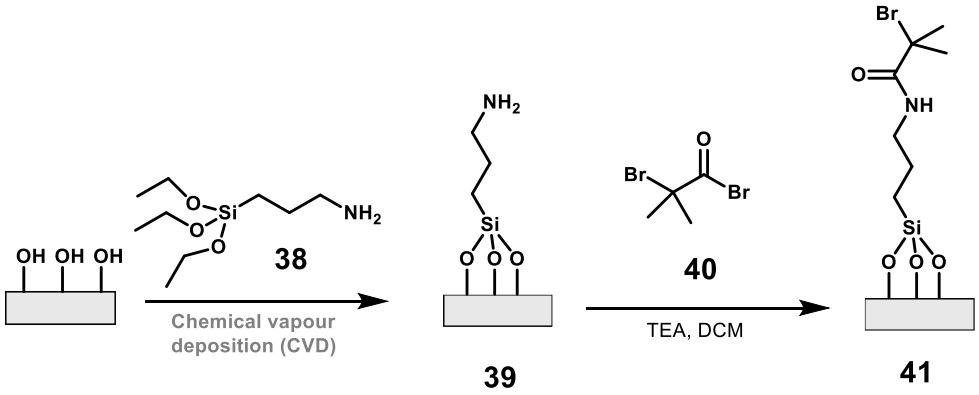

***Scheme 4.6**: Immobilization of the ATRP initiator on silicon wafers. APTES (**38**) is first attached to the oxidated surfaces via Chemical Vapour Deposition. In a second step, the amine moiety undergoes nucleophilic substitution of BiBB (**40**).*

4.3.2.2 Particles

The same procedure was applied both for microparticles (10 μm diameter) and nanoparticles (200 nm diameter).

Particles were added in a beker containing a piranha solution (H_2SO_4 and H_2O_2, 3:1 v/v). After 30 minutes the piranha solution was diluted with MilliQ water and immersed in an ice bath letting the particles to sediment. After 2h the diluted

piranha solution was removed using a Pasteur pipette and added again with MilliQ water, repeating the same procedure until the solution was no more acid (checked with a litmus paper). The particles were then transferred in a 15 mL falcon and washed one more time with water and 2 times with EtOH (~10 mL). Each centrifuge was performed at 6000 rpm for 5 minutes. After this procedure the activated particles were let under vacuum overnight to dry.

The activated SiO_2 particles (100 mg) were suspended in a vial with dry toluene (5 mL) under magnetic stirring. Under stirring, **38** (100 µL, 427 mmol) was added. The sealed vial was put under vigorous stirring for 14h at 100 °C. The suspension was transferred into a 15 mL vial and toluene was added. The mixture was centrifuged for 5 minutes at 6000 rpm and the supernatant gently removed. This operation was repeated one more time with toluene and 3 times with EtOH. The particles where then let to dry overnight.

The APTES-functionalized particles (**42**) obtained from the previous step were put in a clean vial with 5 mL of dry DCM. The solution was degassed for 30 min and, under stirring, TEA (119 µL, 854 µmol) and then **40** (106 µL, 854 µmol) was added. The reaction was stirred under inert atmosphere at room temperature for 14h. Following the same procedure, the suspension was transferred to a 15 mL falcon and washed 2 times with DCM and 3 times with EtOH (about 10 mL each wash) and then let to dry overnight (**Scheme 4.7**).

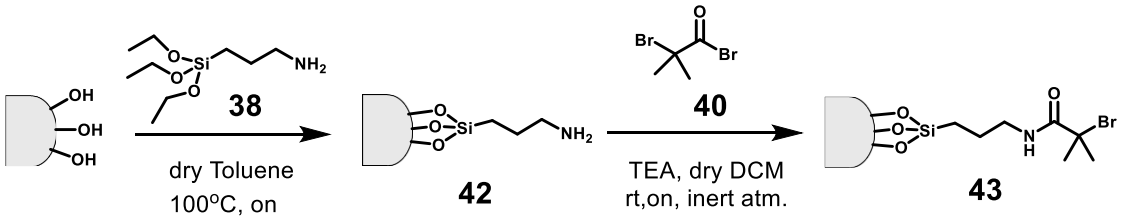

***Scheme 4.7**: Immobilization of the ATRP initiator on silica particles.*

4.3.3 Polymerizations

Polymerizations were performed in solution and from both flat substrates and particles. They all required argon atmosphere and they were carried out at 65 °C for 4h.

All polymerizations were performed using a total volume of solution of 5 mL, with DMSO as solvent and 1.25 mL (2.84 mmol) of filtered monomer (OEGA) with a solvent/monomer ratio 1:3 (v/v). As catalyst $CuBr_2$ was used and Me_6TREN as ligand ($CuBr_2$:L, 1:5). The catalyst was added from a stock solution 0.02 M prepared in DMF. The amount of catalyst added was varied in the different trials (from 15 to 1000 ppm). Performing ARGET ATRP also a reducing agent was needed. Both tin(II) 2-ethylhexanoate (commonly referred to as $Sn(Oct)_2$) and sodium ascorbate (NaAsc) were tested in different ratios with respect to copper.

For polymerizations in solution, ethyl α-bromoisobutyrate **44** (EBiB, 98%) was used as initiator with a degree of polymerization (DP) of 200. While the polymerizations from surfaces were performed in 5 mL vials, using respectively a 1 cm x 2 cm silicon substrate or 30 mg of particles.

Copolymerization between OEGA (**45**) and 3CzIPN-A (**11**) was performed both in solution and from particles adding a 5 mol% amount of **11** (0.142 mmol, 117.2 mg).

The polymerizations in solution were followed with ^{1}H-NMR and GPC in order to check the conversion and the dispersity (*Đ*) of the obtained polymers. Finally, the polymers incorporating the photocatalysts **47** were purified using 12-14 kDa dialysis membrane, for 2 days in 100% ACN and 1 day in water. The polymer was then let 2 days in the lyophilizer before use. The final material was characterized with ^{1}H-NMR, GPC, absorption and emission spectra and cyclic voltammetry. The actual incorporation of the catalyst was estimated by UV-Vis spectroscopy, using a calibration curve (*S.I.* 4.6.2).

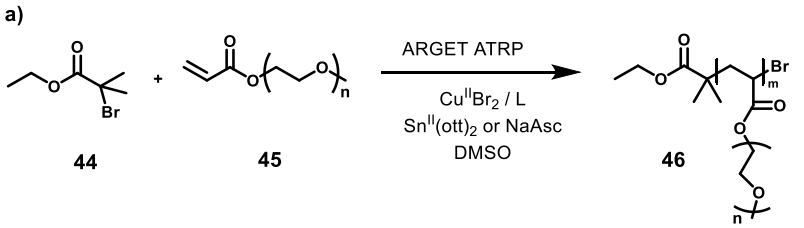

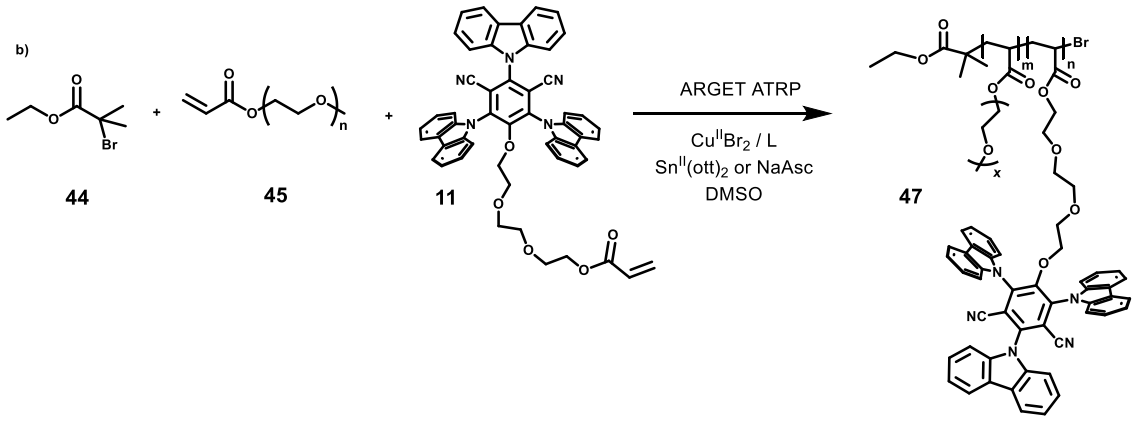

***Scheme 4.8**: ARGET ATRP in solution. a) omopolymerization of OEGA (**45**) using EBiB (**44**) as initiator. b) copolymerization of **45** and **11** using **44** as initiator.*

Differently, when spherical surfaces were functionalized with the photocatalyst-bearing polymer **49**, they were transferred in a 15 mL falcon and purified with several washes before use. Namely, 2 washes with DMSO, 2 with EtOH, 1 with MilliQ water and EDTA and 2 more with EtOH. Finally, they were dried under vacuo overnight. The amount of photocatalyst per mg of particles was estimated using an emission calibration (*S.I.* 4.6.2).

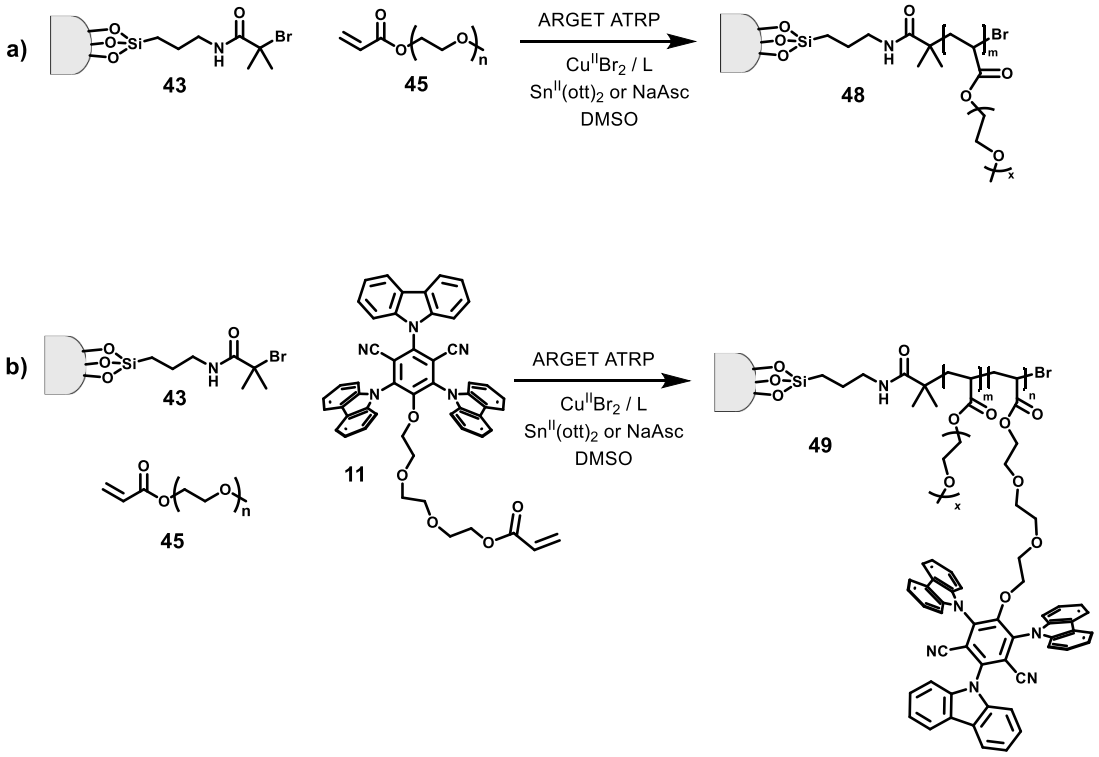

***Scheme 4.9**: grafting from ARGET ATRP from previously APTES+BiBB functionalised silicon surfaces (**43**). a) omopolymerization of OEGA (**45**). b) copolymerization of OEGA (**45**) and 3CzIPN-A (**11**).*

4.4.4 Photocatalytic tests

4.4.4.1 Giese-type addition

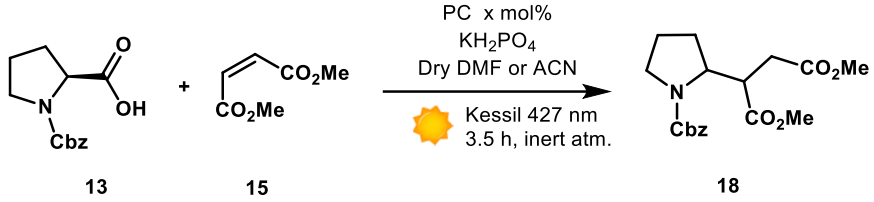

***Scheme 4.10**: Giese-type radical addition to an electron poor double bond providing the final product.*

The reaction was performed following an existing procedure[45]. An oven-dried 10 mL Schlenck flask with a glass cap and a magnetic stir bar was charged with the selected photocatalyst (variable catalyst loading from 0.5 to 5 molar %), Cbz-Pro-OH **13** (0.2 mmol, 1.0 equiv), methyl maleate **15** (0.2 mmol, 1.0 equiv), K_2HPO_4 (0.24 mmol, 1.2 equiv), and 0.5 mL of DMF or ACN. The reaction mixture was degassed by using the freeze-pump thaw technique, then irradiated with a 427 nm Kessil lamp at 25% intensity. After 3.5h, the reaction mixture was diluted with saturated aqueous $NaHCO_3$ solution and extracted with Et_2O (3 × 5 mL). The combined organic extracts were washed with water and brine, dried over Na_2SO_4 and concentrated in vacuo. Purification of the crude product by flash chromatography on silica gel afforded the desired product **18**.

When the photoactive polymer was used for the recyclability test, the DMF was evaporated and the polymer precipitated with Et_2O before the extractions. Since the polymer contained impurities such as salts and KH_2PO_4, dialysis purification of the polymer were needed before reuse.

4.4.2.4 Povarov-type reaction

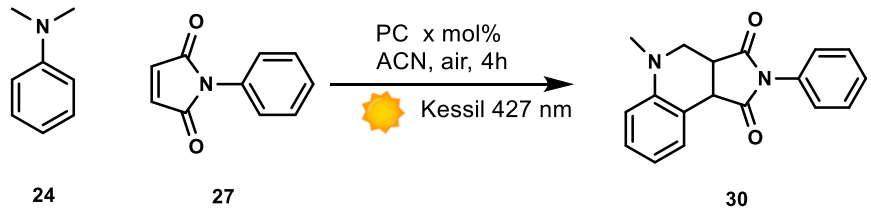

***Scheme 4.11**: Povarov-type photoreaction. [4+2] cycloaddition.*

Following and existent procedure Povarov-type reactions were performed at 0.1 mmol scale with a variable loading of the catalyst. *N*-phenylmaleimide **27** (17.3

mg, 1 eq, 0.1 mmol), was dissolved in 0.9 mL of dry ACN in a 4 mL vial. *N,N*-dimethylaniline **24** (25 µL, 2 equivalents, 0.2 mmol) was then added at the solution dropwise and under vigorous stirring at room temperature. The solution was irradiated with a 427 nm Kessil lamp at 25% intensity for 4h. The solvent was removed by pressure evaporation and the crude checked with ^{1}H-NMR in order to determine the ^{1}H-NMR yield using trimethoxy benzene as internal standard.

When the photoactive polymer was used for the recyclability test, after the evaporation of the ACN, Et_2O was added in order to precipitate the polymer and recover the product of the reaction. The precipitate polymer was then reused.

4.4.5 Photoreactions in water

Photoreaction in water was tried to test the eventual reactivity in water.

4.4.5.1 Giese-type reaction in water

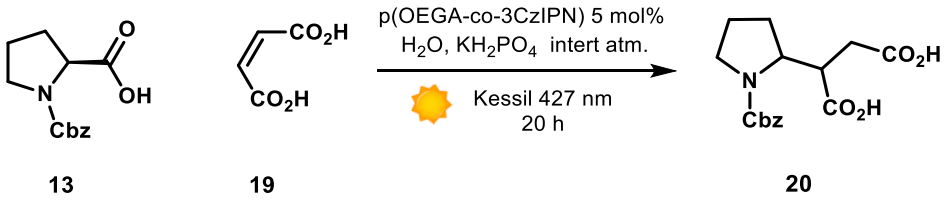

***Scheme 4.12**: Giese-type reaction in water.*

The reaction was performed following an existing procedure[45]. An oven-dried 10 mL Schlenck flask with a glass cap and a magnetic stir bar was charged with the selected photocatalyst (variable catalyst loading), Cbz-Pro-OH **13** (0.2 mmol, 1.0 equiv), maleic acid **19** (0.6 mmol, 3.0 equiv), K_2HPO_4 (0.24 mmol, 1.2 equiv), and 0.5 mL of DMF or ACN. The reaction mixture was degassed by using the freeze-pump thaw technique, then irradiated with a 427 nm Kessil lamp at 25% intensity. After 20h, the reaction mixture was added with saturated aqueous $NaHCO_3$ solution and extracted with EtOAc (3 × 5 mL). The acqueous phase was then brought to slightly acid pH adding drops of concentrated HCl. The extraction was so repeated. The combined organic extracts were dried over Na_2SO_4 and concentrated in vacuo. Purification of the crude product by inverse flash

chromatography (C18 column, gradient ACN and ACN:H_2O 1:1) on silica gel to obtain the product **20**.

Nevertheless, the recovered fractions showed just starting materials.

4.4.5.1 Toluene-pyrrole C-C coupling

This reaction followed reported procedure[122] for C-C coupling (in organic solvents) passing through the in situ formation of sulfonium salts. Since this salts can be water soluble, the reaction was performed in water.

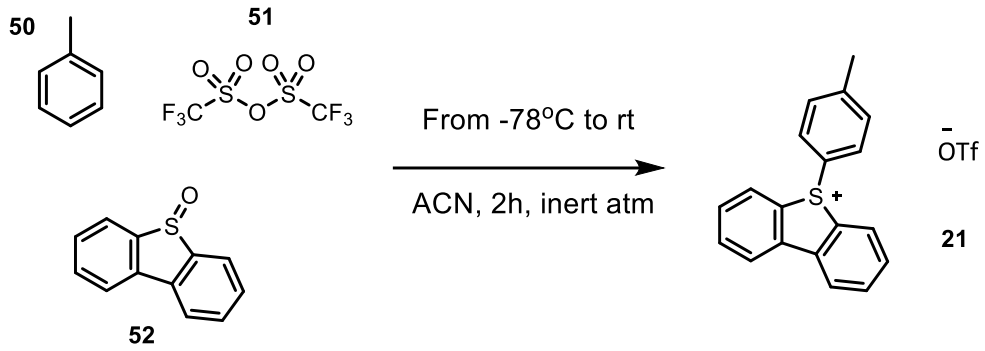

***Scheme 4.13**: Formation in situ of the water soluble sulfonium salt.*

Tf_2O **51** (1.2 equiv., 0.24 mmol, 0.4 mL) was slowly added to a stirred solution of the toluene **50** (0.2 mmol, 1 eq) and dibenzothiophene S-oxide **52** (1.1 equiv.,0.22 mmol, 44 mg) in DCM (0.1 M) at −78 °C under a nitrogen atmosphere. The resulting solution was stirred at this temperature for 15 minutes before warming to room temperature. After stirring for 2 h, the solvent was removed in vacuo. The sulfonium salt **21** was then precipitated by the addition of Et_2O. The Et_2O was then decanted off and the crude product was washed with further portions of Et_2O.

At this point the generated sulfonium salt was used for the following step.

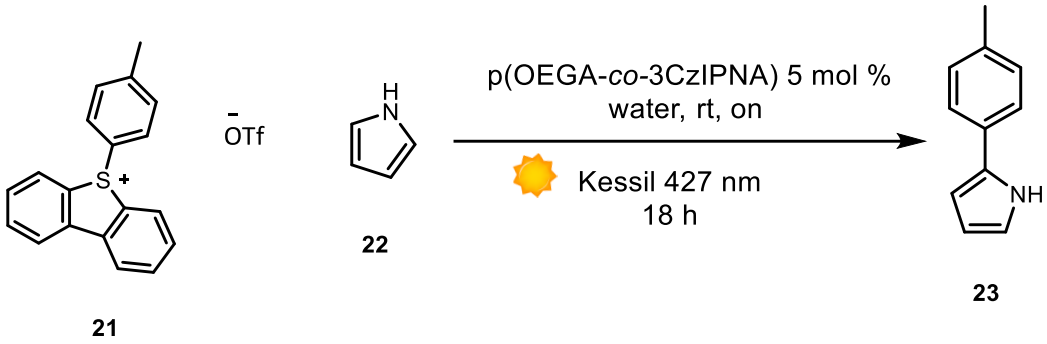

***Scheme 4.14**: second step, CH-CH coupling of toluene with the radical trap (pyrrole).*

P(OEGA-co-3CzIPN-A) (5 mol%) was then added to the reaction vial. H_2O (0.2 M) was then added followed by the pyrrole **22** (20 eq, 4 mmol, 3.9 mL). The reaction mixture was then irradiated with a Kessil lamp for 18 h before quenching with aqueous saturated $NaHCO_3$ and dilution with EtOAc. The organic layer was washed with brine, dried using Na_2SO_4, filtered, and concentrated in vacuo, to give the crude product, which was purified by column chromatography on silica gel.

4.5 NMR spectra

3CzIPN-A

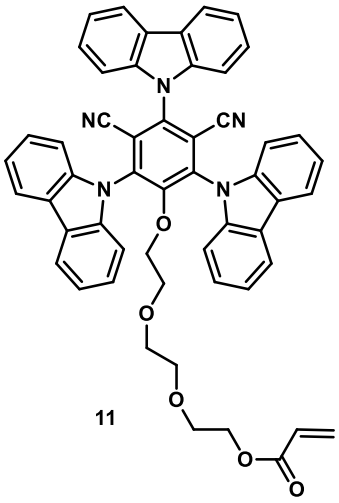

Yellow solid

^{1}H-NMR (400 MHz, CD_3CN): δ (ppm) 8.31-8.24 (m, 6H); 7.75 (d, *J*= 8 Hz, 2H); 7.70-7.61 (m, 10H), 7.50-7.42 (m, 6H), 6.30 (dd, $J_{1,trans}$=16 Hz, $J_{2,gem}$=0.2 Hz, 1H), 6.08 (dd, $J_{1,trans}$=16 Hz, $J_{2,cis}$=12 Hz, 1H), 5.83 (dd, $J_{1,cis}$=8 Hz, $J_{2,gem}$=0.2 Hz, 1H),

4.06 (m, 2H), 3.32 (t, *J*= 8Hz, 2H), 3.04 (t, *J*= 8Hz, 2H), 2.82 (t, *J*= 8Hz, 2H), 2.47 (t, *J*= 8Hz, 2H), 2.43 (t, *J*= 8Hz, 2H).

^{13}C-NMR (100 MHz, $CDCl_3$): δ (ppm) 166.1, 155.3, 140.2, 139.6, 139.0, 131.0, 128.1, 126.8, 124.5, 122.0, 121.2, 120.1, 116.4, 110.2, 109.3, 74.0, 70.0, 69.7, 69.1, 68.7, 63.3.

3CzIPN-F

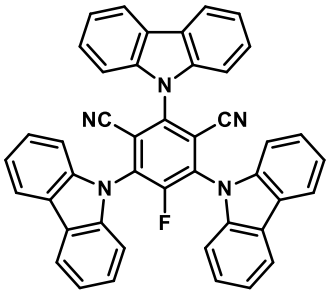

35

Yellow solid

^{1}H-NMR (400 MHz, CD_3CN): δ (ppm) 8.31-8.24 (m, 6H); 7.75 (d, *J*= 8 Hz, 2H); 7.70-7.61 (m, 10H), 7.50-7.42 (m, 6H).

^{13}C-NMR (100 MHz, $CDCl_3$): δ (ppm) 154.4, 142.8, 140.2, 139.4, 135.5, 127.2, 126.98, 127.0, 124.3, 124.0, 122.3, 122.1, 121.0, 120.2, 117.4, 110.8, 110.3.

^{19}F-NMR (376 MHz, CD_3CN): δ (ppm) -116.1 (s, 1F)

3CzIPN-TEG

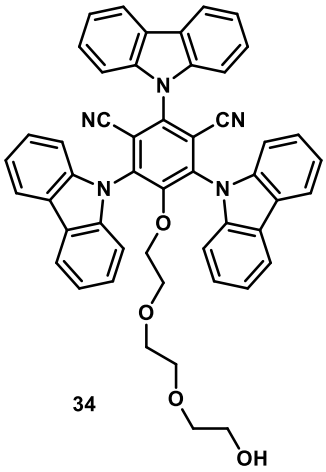

34

Yellow solid

^{1}H-NMR (400 MHz, $CDCl_3$): δ (ppm) 8.31-8.24 (m, 6H); 7.75 (d, *J*= 8 Hz, 2H); 7.70-7.61 (m, 10H), 7.50-7.42 (m, 6H), 3.41 (q, *J*= 4Hz, 2 H), 3.17 (t, *J*= 4Hz, 2H), 3.05 (t, *J*= 4 Hz, 2H), 2.81 (t, *J*= 4 Hz, 2H), 2.48 (t, *J*= 4 Hz, 2H), 2.44 (t, *J*= 4Hz, 2H).

^{13}C NMR (100 MHz, $CDCl_3$): δ (ppm) 155.1, 140.3, 139.7, 138.9, 126.8, 121.2, 121.9, 120.9, 116.5, 110.2, 109.3, 74.0, 72.0, 69.8, 69.7, 69.2, 61.6.

3CzIPN-red

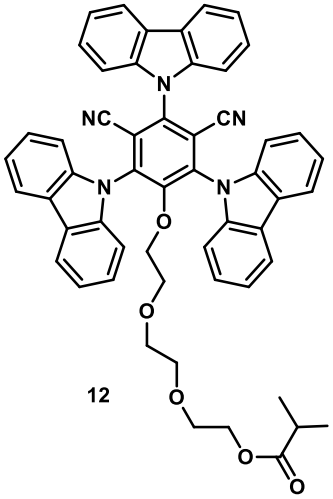

12

Yellow solid

^{1}H-NMR (400 MHz, CD_3CN): δ (ppm) 8.31-8.24 (m, 6H); 7.75 (d, *J*= 8 Hz, 2H); 7.70-7.61 (m, 10H), 7.50-7.42 (m, 6H), 4.04 (t, *J*= 8Hz, 2H), 3.34 (t, *J*= 4Hz, 2H), 2.98 (t, *J*= 4Hz, 2H), 2.86 (t, *J*= 4Hz, 2H), 2.49 (m, 5H), 1.1 (d, *J*=4Hz, 6H).

^{13}C-NMR (100 MHz, $CDCl_3$): δ (ppm)) 166.1, 155.3, 140.2, 139.6, 139.0, 126.8, 124.5, 122.0, 121.2, 120.1, 116.4, 110.2, 109.3, 74.0, 70.0, 69.7, 69.1, 68.7, 63.3, 33.9, 18.9.

Products of photoreactions:

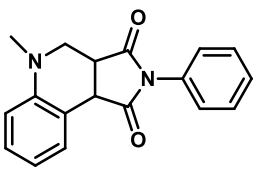

30

^{1}H-NMR (400 MHz, $CDCl_3$): δ (ppm) 7.53 (d, *J* = 7Hz, 1H), 7.46 (t, *J* = 7Hz, 2H), 7.38 (t, *J* = 7Hz, 1H), 7.28–7.23 (m, 3H), 6.92 (td, *J* = 7Hz, 1Hz, 1H), 6.76 (d, *J* = 8Hz, 1H), 4.15 (d, *J* = 9Hz, 1H), 3.63 (dd, *J* = 11, 2.7 Hz, 1H), 3.54 (ddd, *J* = 9, 4, 3Hz, 1H), 3.14 (dd, *J* = 11, 4Hz, 1H), 2.85 (s, 3H).

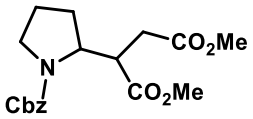

13

^{1}H-NMR (500 MHz, $CDCl_3$): δ (ppm) mixture of diastereomers and rotamers: δ 7.41- 7.29 (m, 5H), 5.21-5.08 (m, 2H), 4.31-4.28 (m, 0.55H), 4.17-4.09 (m, 0.45H), 3.69-3.64 (m, 6.8H), 3.56-3.47 (m, 0.8H), 3.37-3.33 (m, 0.8H), 3.28-3.22 (m, 0.6H), 2.81-2.70 (m, 1H), 2.54-2.29 (m, 1H), 1.95-1.72 (m, 4H).

P(OEGA-*co*-3CzIPN-A)

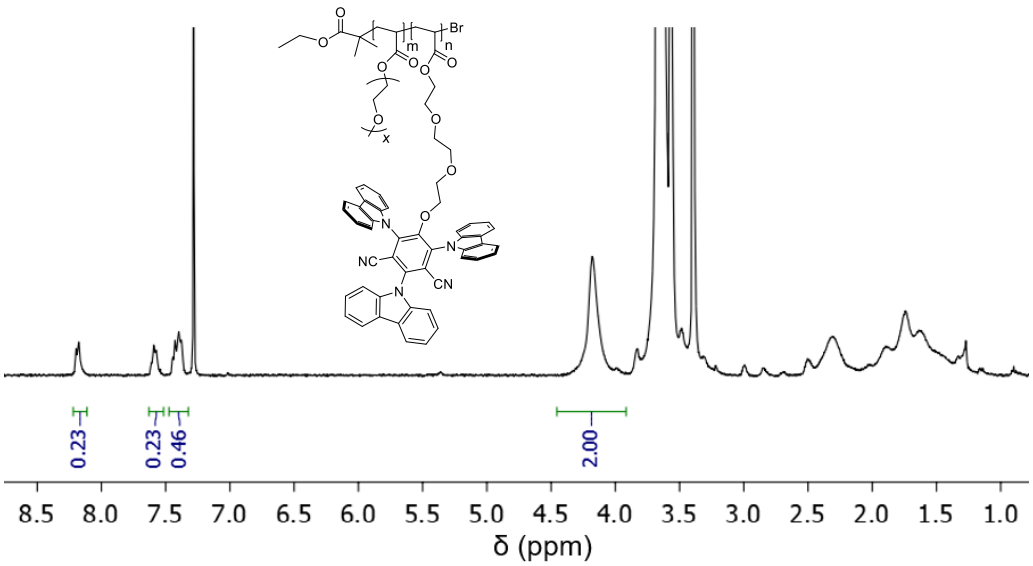

***Figure 4.1**: ^{1}H-NMR spectrum (400 MHz) of poly(OEGA-co-3CzIPN-A) in ACN. The broad singlet at 4.17 ppm correspond to the first methylene of the glycolic chain (2H), while the three multiplets from 7.4 to 8.2 ppm correspond to the 24 aromatic protons of the carbazoles. This can be used for the estimation of the degree of incorporation of the photocatalyst.*

Reaction crudes

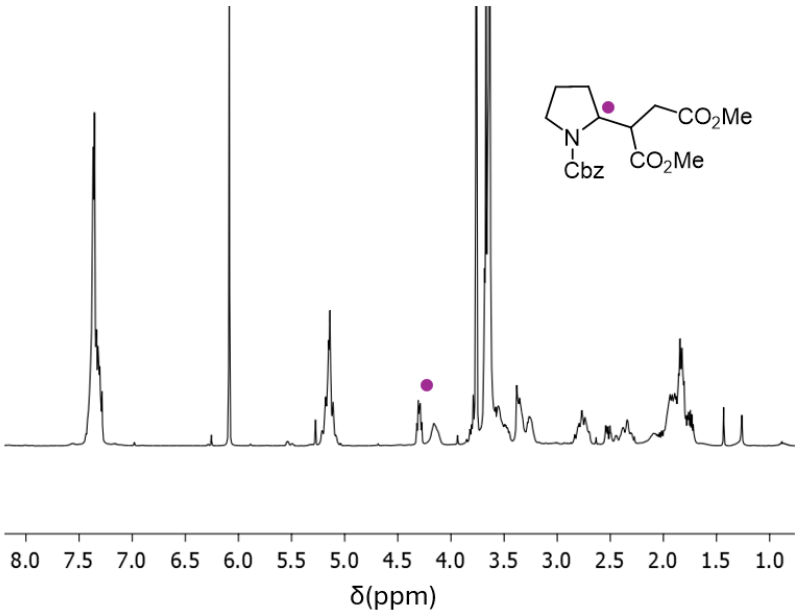

***Figure 4.2**: ^{1}H-NMR (400 MHz, $CDCl_3$) reaction crude of the Giese-type photoreaction after 3.5 h irradiation with a 427 nm Kessil lamp with the addition of rimethoxybenzene as internal standard. The highlighted proton is the diagnostic one used for the calculation of the NMR yield which correspond to the two peaks, namely the broad signal at 4.15 ppm and the multiplet at 4.30 due to the formation of the rotamers.*

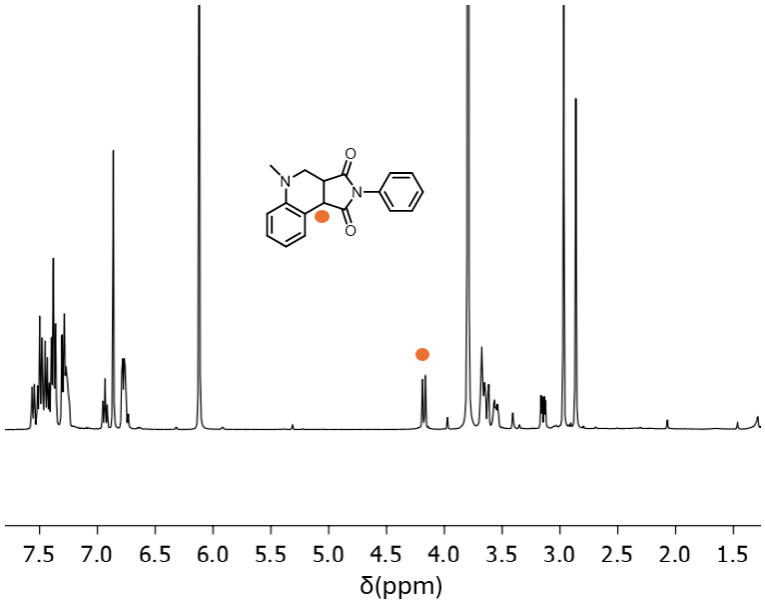

***Figure 4.3**: ^{1}H-NMR (400 MHz, $CDCl_3$) reaction crude of the Povarov-type photoreaction after 4 h irradiation with a 427 nm Kessil lamp with the addition of rimethoxybenzene as internal standard. The highlighted proton is the diagnostic one used for the calculation of the NMR yield which correspond to the doublet at 4.18 ppm.*

4.6 Absorption and emission characterizations

3CzIPN-A

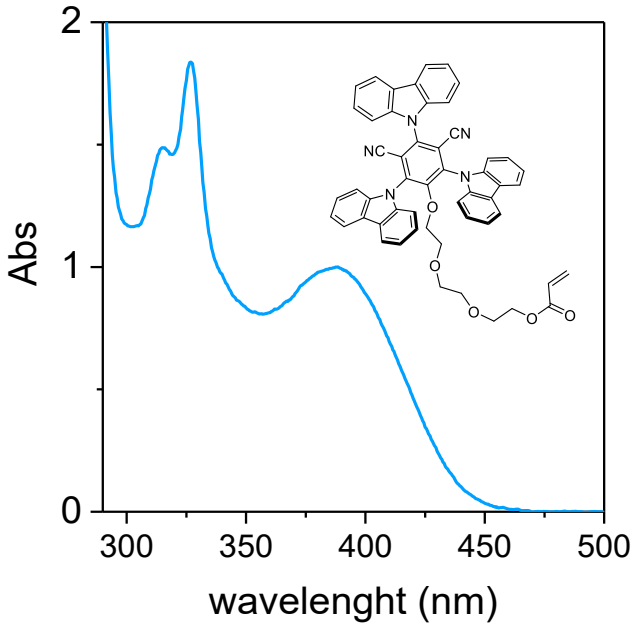

***Figure 4.4**: Absorption profile of 3CzIPN-A measured in ACN at room temperature.*

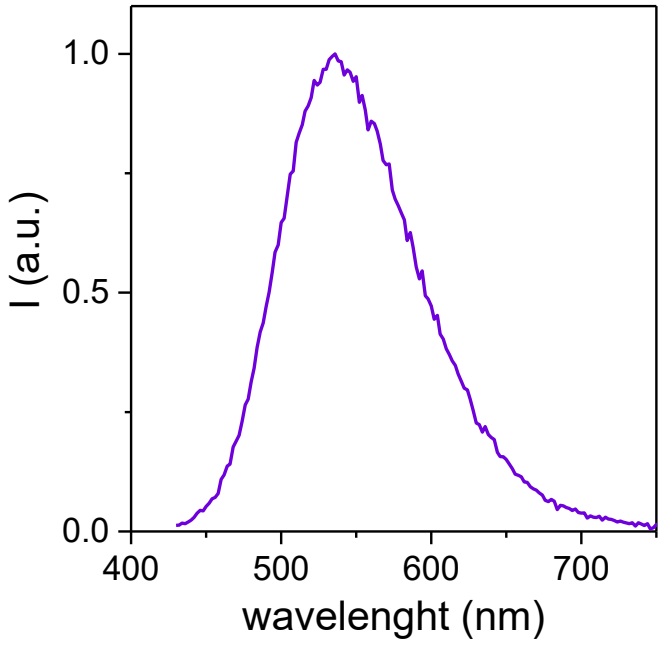

***Figure 4.5**: Emission profile of 3CzIPN-A measured in ACN at room temperature exciting at λ=415 nm.*

3CzIPN-red

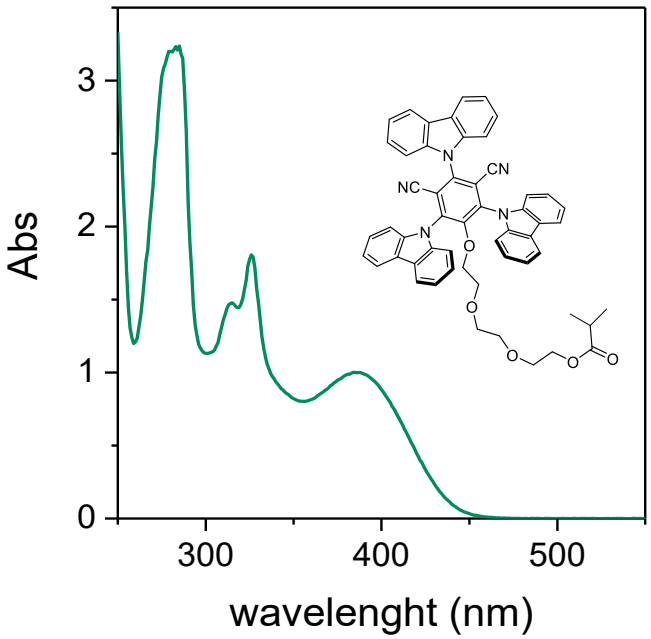

***Figure 4.6**: Absorption profile of 3CzIPN-red measured in ACN at room temperature.*

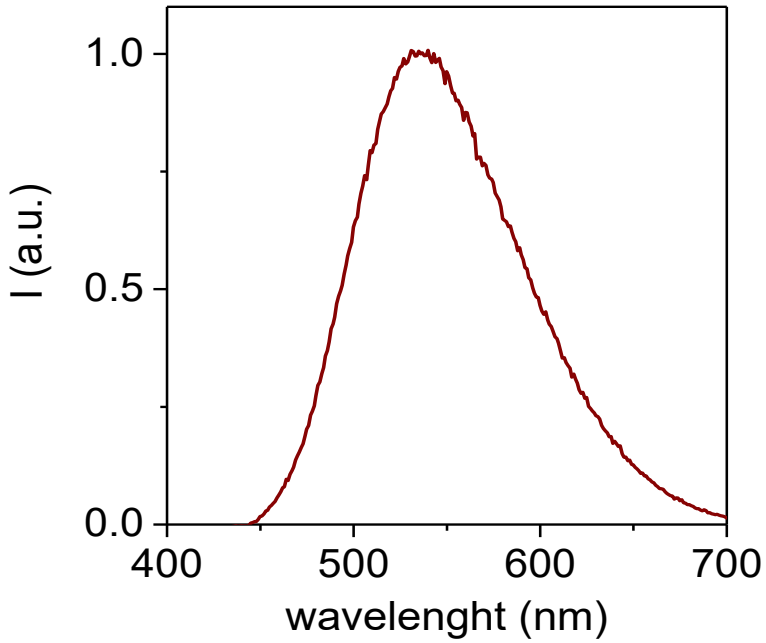

***Figure 4.7**: Emission profile of 3CzIPN-red measured in ACN at room temperature exciting at λ=415 nm.*

p(OEGA-*co*-3CzIPN)

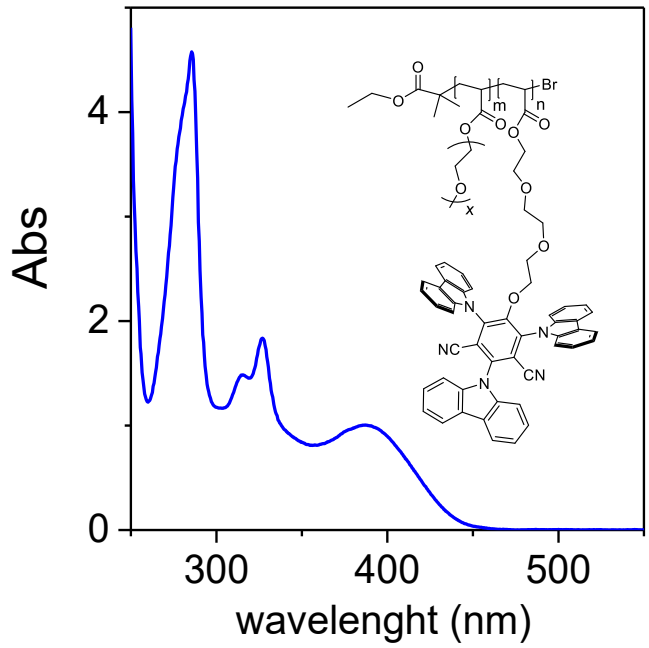

***Figure 4.8**: Absorption profile of p(OEGA-co-3CzIPN-A) measured in ACN at room temperature.*

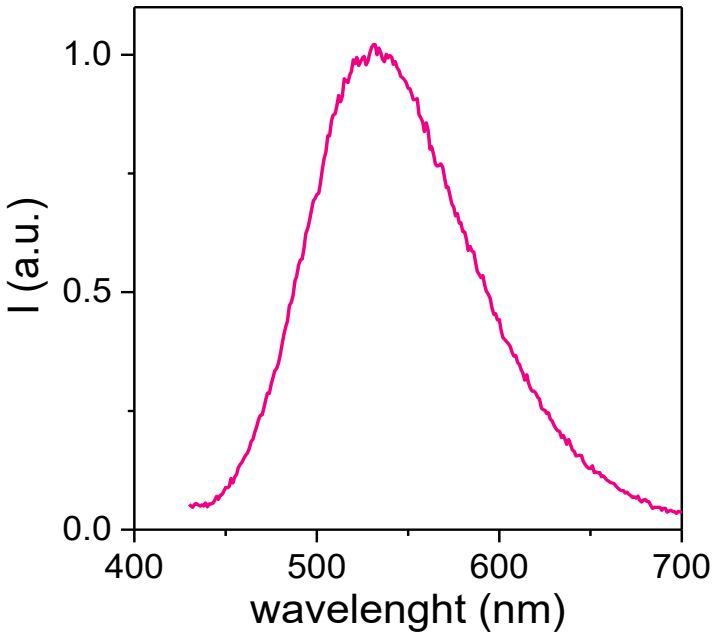

***Figure 4.9**: Emission profile of p(OEGA-co-3CzIPN-A) measured in ACN at room temperature exciting at λ=415 nm.*

4.6.1 Degradations

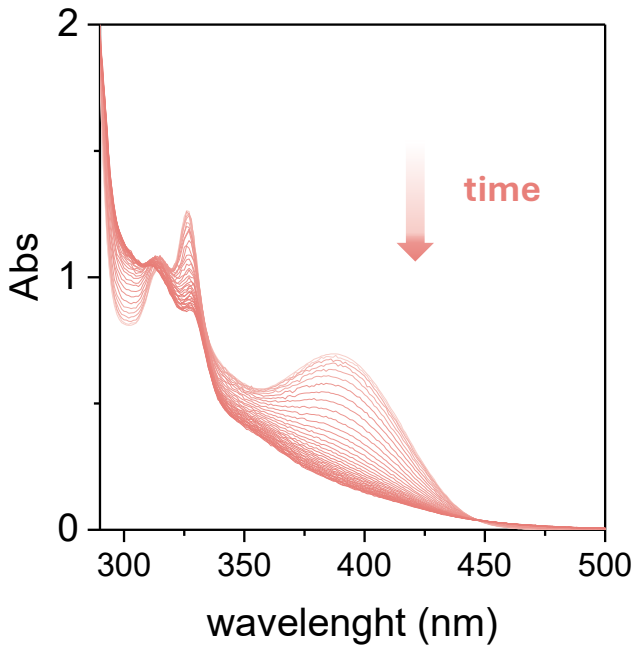

***Figure 4.10**: UV-Vis spectra of the p(OEGA-co-3CzIPN-A) degradation in ACN with Cbz-Pro-OH and HK_2PO_4 in 3h at room temperature irradiating with a 425 nm optical fibre.*

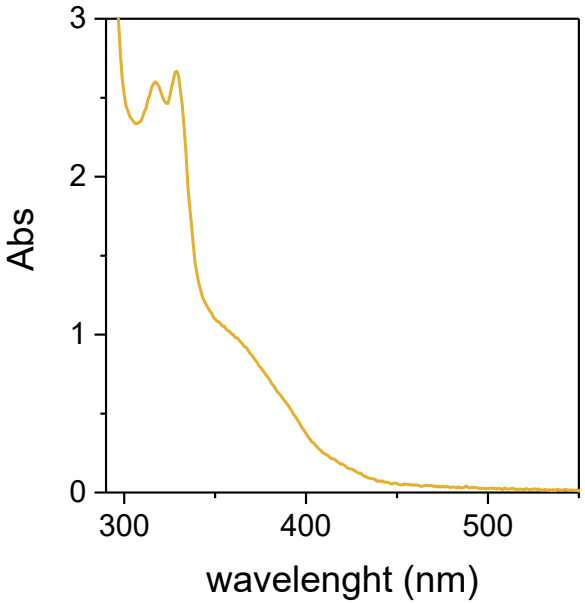

***Figure 4.11**: Absorption profile of p(OEGA-co-3CzIPN-A) in ACN after the Giese-type photoreaction in ACN. 3.5 hours of irradiation with 427 nm Kessil lamp at 25% intensity.*

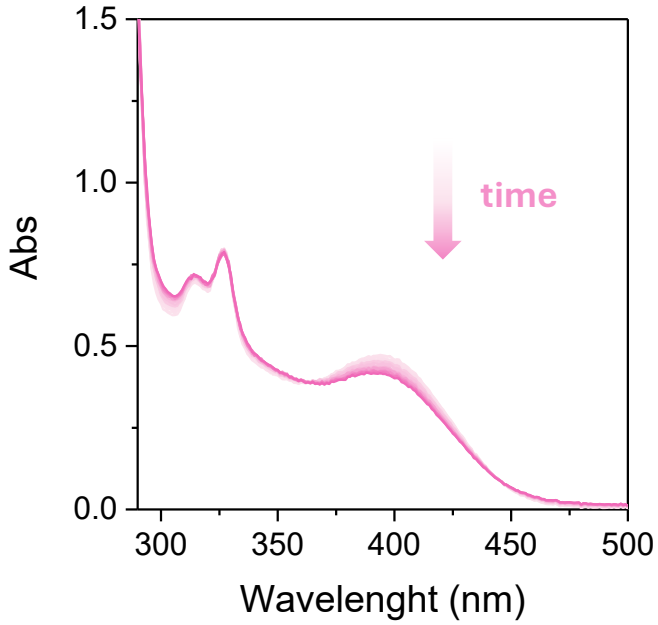

***Figure 4.12**: UV-Vis spectra of the p(OEGA-co-3CzIPN-A) degradation in ACN with HK_2PO_4 in 3h at room temperature irradiating with a 425 nm optical fibre.*

4.6.2 Calibrations

Absorption calibration

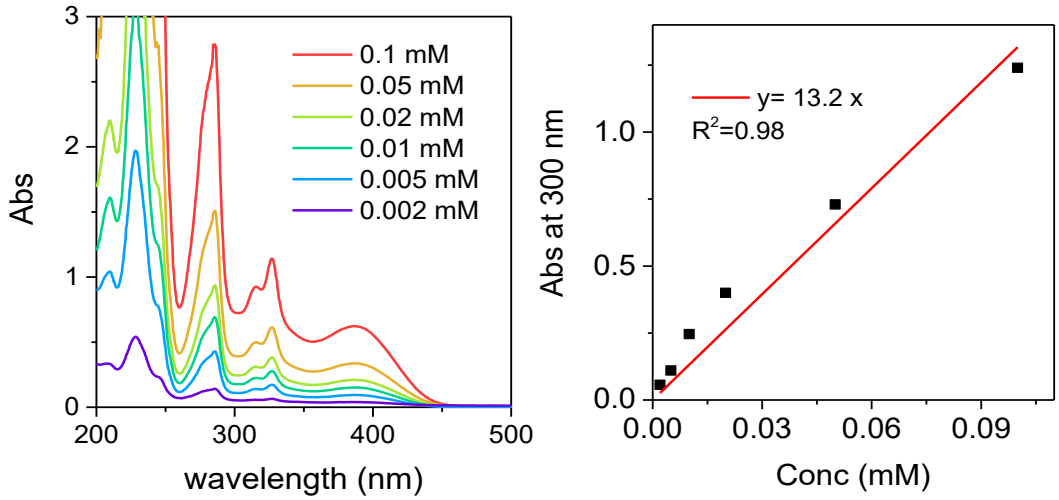

***Figure 4.13**: On the left absorption spectra at different concentrations of the monomer 3CzIPN-A in ACN at room temperature. On the right the values at 300 nm and the linear fit with the intercept fixed at 0.*

Emission calibration

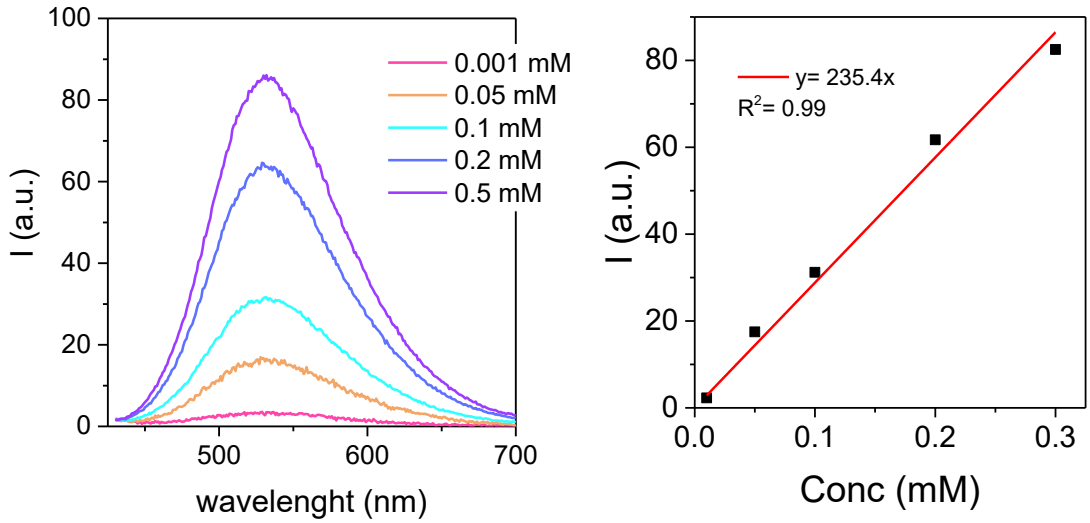

***Figure 4.14**: On the left the emission spectra at different concentration of the polymer incorporating the photocatalyst p(OEGA-co-3CzIPN-A) in DMF at room temperature exciting at 415 nm. On the right the obtained calibration line using the emission values at 525 nm and fixing the intercept at 0.*

4.6.3 Lifetime

Lifetime of both prompt and delayed fluorescence were calculated for the monomer 3CzIPN-A and the polymer p(OEGA-*co*-3CzIPN-A) exploiting their emission.

3CzIPN-A

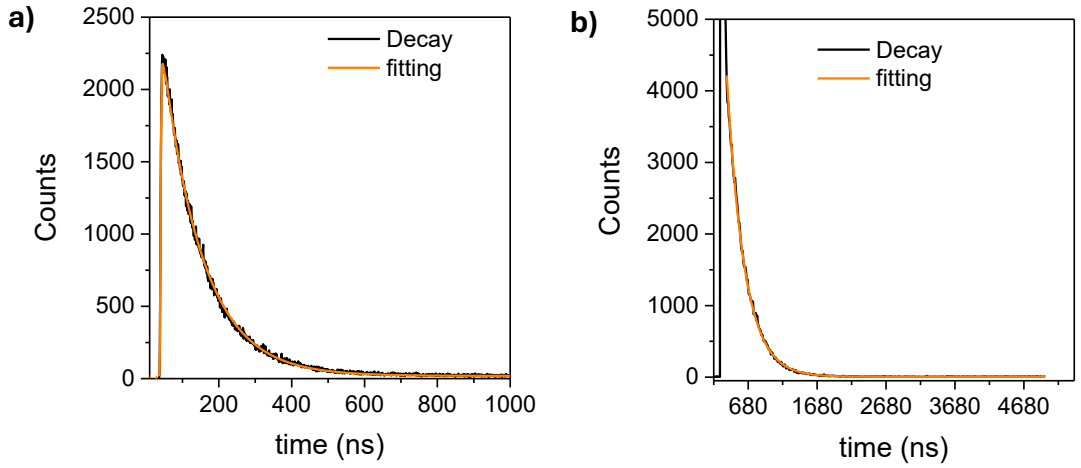

***Figure 4.15**: a) Exponential decay and fitting for lifetime measurement of direct fluorescence of 3CzIPN-A in ACN at room temperature with TCSPC technique exciting at 402 nm with a 100 ns window and 3 nm slit. The fitting showed a lifetime of 10.5 ns for the prompt fluorescence. b) Exponential decay and fitting for lifetime measurement of delayed fluorescence of 3CzIPN-A in ACN at room temperature with MCS technique exciting at 402 nm and 2.5 nm slit. The fitting gave a lifetime of 255 ns for the delayed fluorescence.*

P(OEGA-*co*-3CzIPN-A)

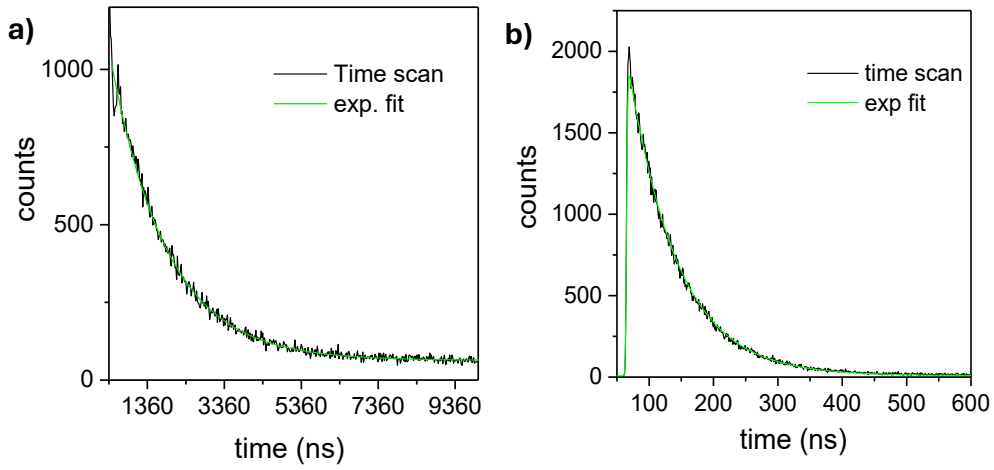

***Figure 4.16**: a) Exponential decay and fitting for lifetime measurement of direct fluorescence of p(OEGA-co-3CZIPN-A) in ACN at room temperature in inert atmosphere with TCSPC technique exciting at 402 nm with a 200 ns window and 1.1 nm slit. The fitting showed a lifetime of 14.2 ns for the prompt fluorescence. b) Exponential decay and fitting for lifetime measurement of delayed fluorescence of p(OEGA-co-3CZIPN-A) in ACN at room temperature in inert atmosphere with MCS technique exciting at 402 nm and 1.1 nm slit. The fitting gave a lifetime of 1.45 µs for the delayed fluorescence.*

4.7 CVs and redox potentials estimation

3CzIPN-A

The CV profile of the monomer 3CzIPN-A shows two reduction peaks (**Figure 4.19, left**), with the first reversible peak attributed to the photoactive moiety, while the second irreversible peak is possibly due to the acrylate function.

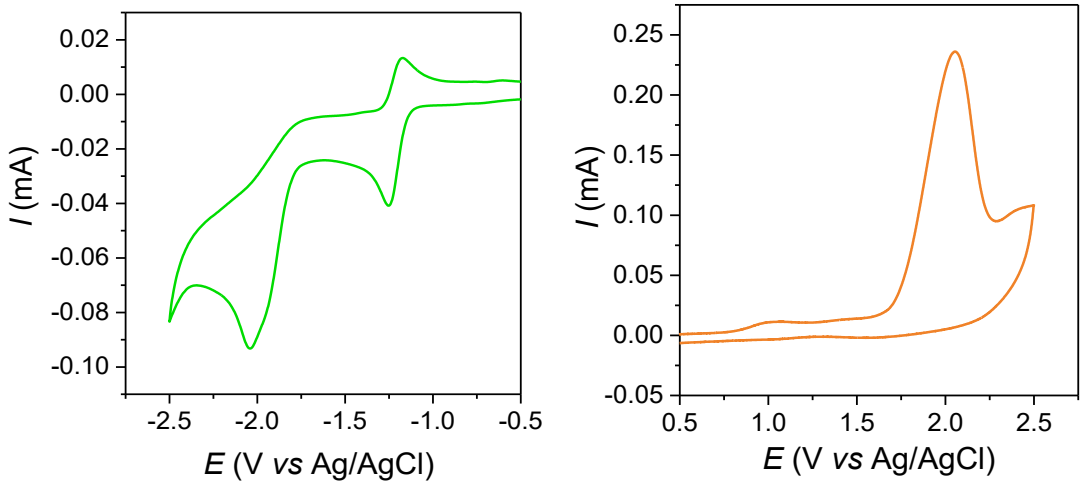

***Figure 4.17**: CV in the reduction (left) and oxidation (right) direction of a solution 0.1 mM of 3CzIPN-A in ACN using tetrabutylammonium hexafluorophosphate ($TBAPF_6$) 0.1 M as supporting electrolyte and a scan rate of 1V/s. The electrodes are described in Section 4.2: Instruments.*

3CzIPN-red

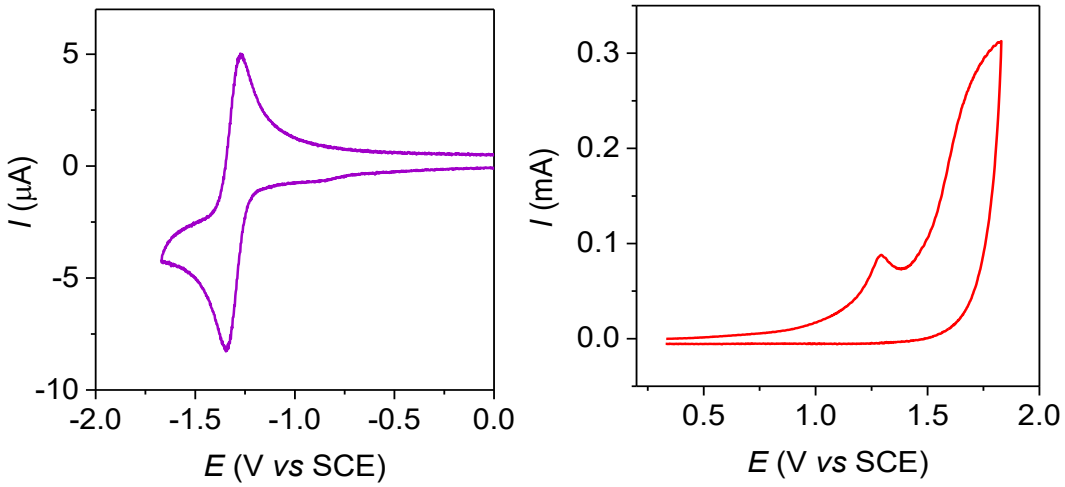

***Figure 4.18**: CV in the reduction (left) and oxidation (right) directionof a solution 0.1 mM 3CzIPN-red in ACN using tetraethylammonium tetrafluoroborate (TEATFB) 0.1 M as supporting electrolyte and a scan rate of 1V/s. The electrodes are described in Section 4.2: Instruments.*

Ferrocene (Fc) was added at the end of the CV experiment as an internal standard, to refer all potentials to the saturated calomel electrode (SCE), considering that $E°(Fc^+/Fc)$ = 0.391 V *vs* SCE in ACN. The Rhem Weller formalism was then used to estimate the redox potentials in the excited state, by calculating the intersection points of the normalized absorption and emission spectra (**Figure 4.21**) that was then converted in Volt to find the $E_{0,0}$.

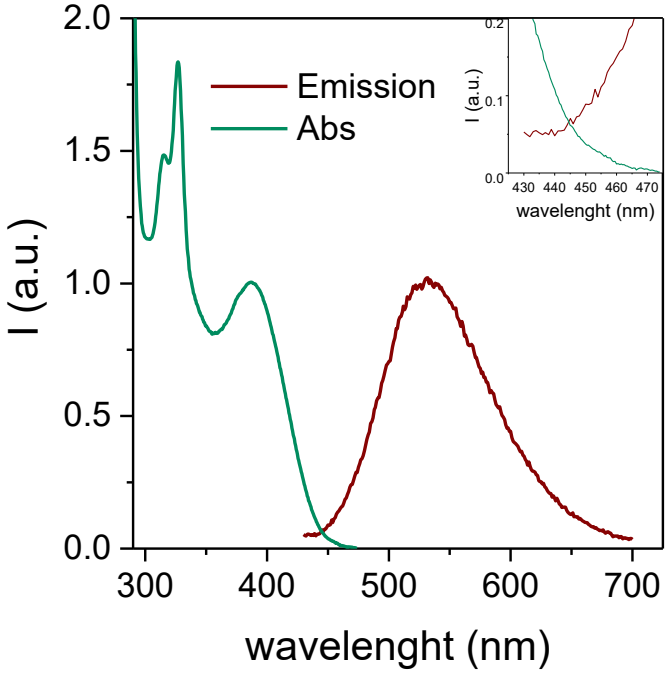

***Figure 4.19**: Intersection point of the normalized spectra resulting in the crossing point at 445 nm. Converting results in $E_{0,0}$= 2.74 V.*

From the CVs it was calculated that E_p ($PC^{\bullet+}$/PC) = 1.28 V and $E_{1/2}$ (PC/$PC^{\bullet-}$) = 1.30 V, yielding E_p ($PC^{\bullet+}$/PC*) = -1.46 V and $E_{1/2}$ (PC/$PC^{\bullet-}$) = 1.44 V.

The same procedure was followed for calculating the redox potentials of the copolymer p(OEGA-*co*-3CzIPN-A).

p(OEGA-*co*-3CzIPN-A)

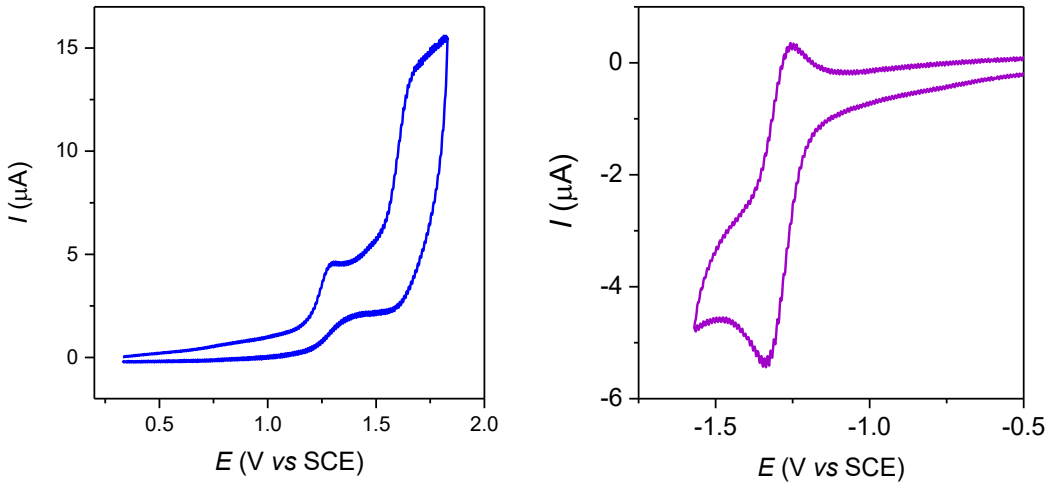

***Figure 4.20**: CV in the reduction (left) and oxidation (right) direction of a solution 0.1 mM 3CzIPN-red in ACN using TEATFB 0.1 M as supporting electrolyte and a scan rate of 1V/s. The electrodes are described in Section 4.2: Instruments.*

The redox potentials in the excited state were then estimated thanks to the crossing point of the absorption and emission spectra (**Figure 4.23**).

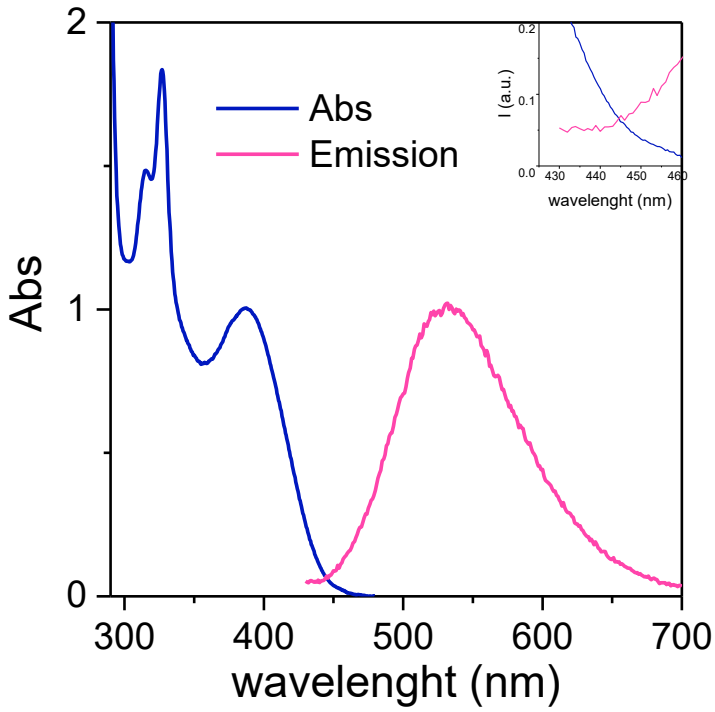

***Figure 4.21**: Intersection point of the normalized spectra resulting in the crossing point at 445 nm. Converting results in $E_{0,0}$= 2.74.*

4.8 Polymer conversion

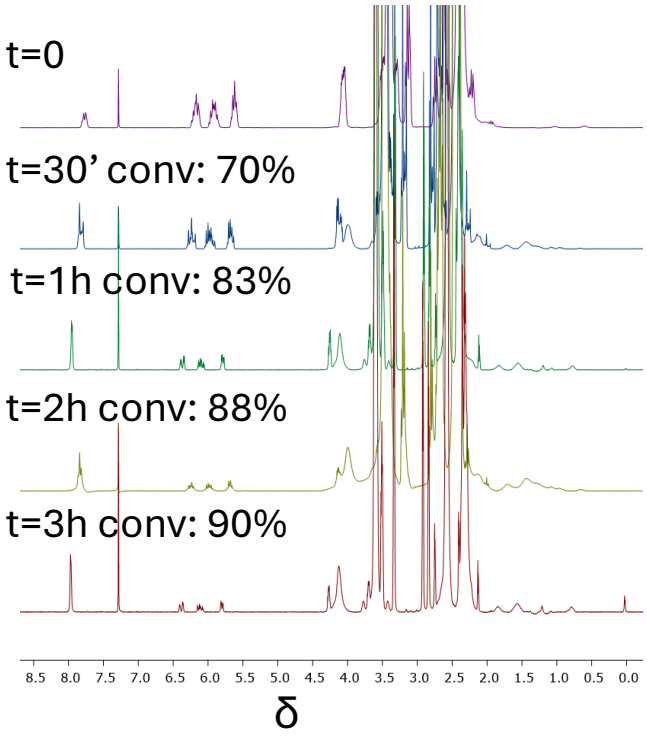

***Figure 4.22**: ^{1}H-NMR spectra (400 MHz, $CDCl_3$) of the reaction mixture at different times. The signal used as internal standard is the DMF signal at 8.0 ppm and for the polymer the decrease of the double bond signals were monitored. Namely the peaks at 5.85, 6.10 and 6.40 ppm each corresponding to one proton.*

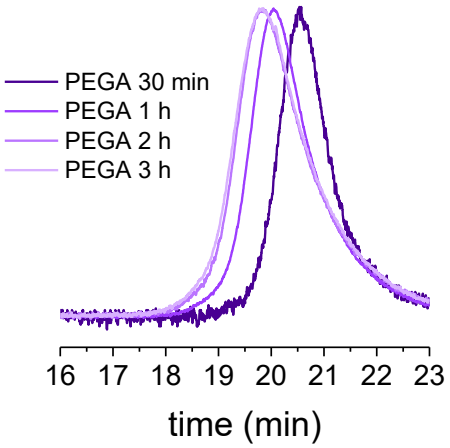

***Figure 4.23**: GPC traces of the reaction mixture at different times showing a final dispersity (Đ) of 1.2.*

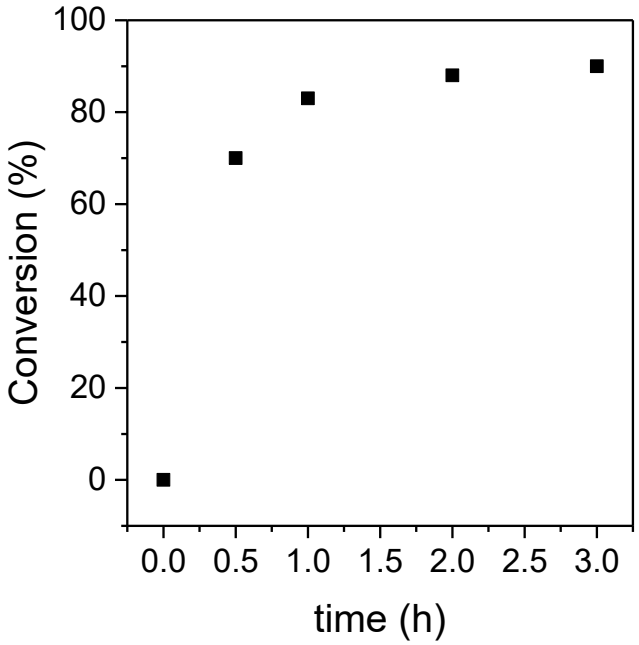

***Figure 4.24**: ^{1}H-NMR conversion vs time of the polymerization in solution using $CuBr_2$ 26 mM and NaAsc 13 mM in DMSO with a 2 vol% of water reported in section 2.6.2 (Results and discussion).*

4.9 Particles

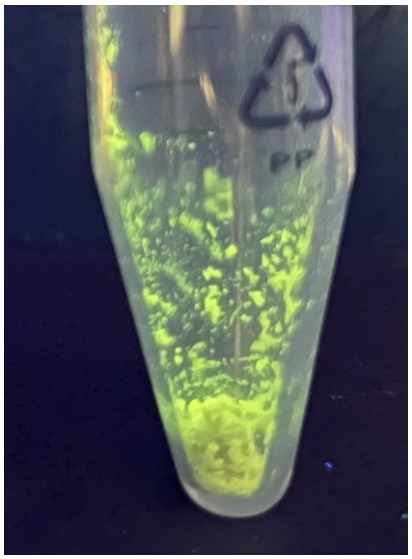

***Figure 4.25**: Picture of photoactive particles under UV light (365 nm).*

TGA of 200 nm particles with PEGA brush shell

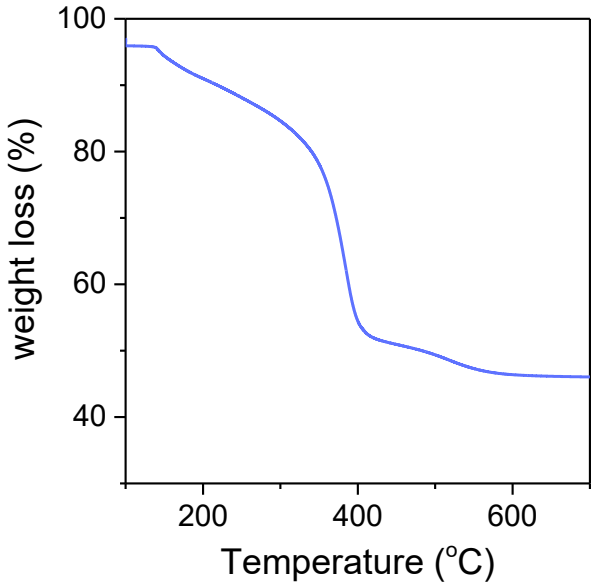

***Figure 4.26**: TGA of the first trial of functionalization with PEGA of 200 nm diameter SiO_2 particles showing a weight loss of around 50%.*

TGA of 10 µm particles with p(OEGA-*co*-3CzIPN-A) brush shell

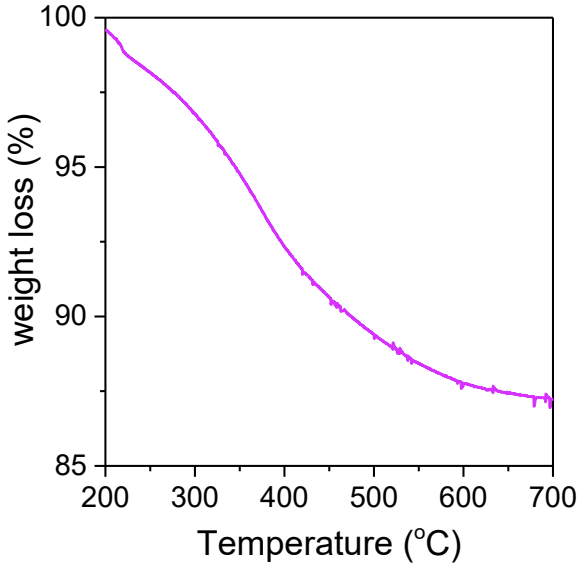

***Figure 4.27**: TGA of 10 µm diameter silica particles functionalized with p(OEGA-co-3CzIPN-A) brush shell before the optimized conditions from surface showing around 13% of weight loss.*

SEM pictures of 200 nm particles

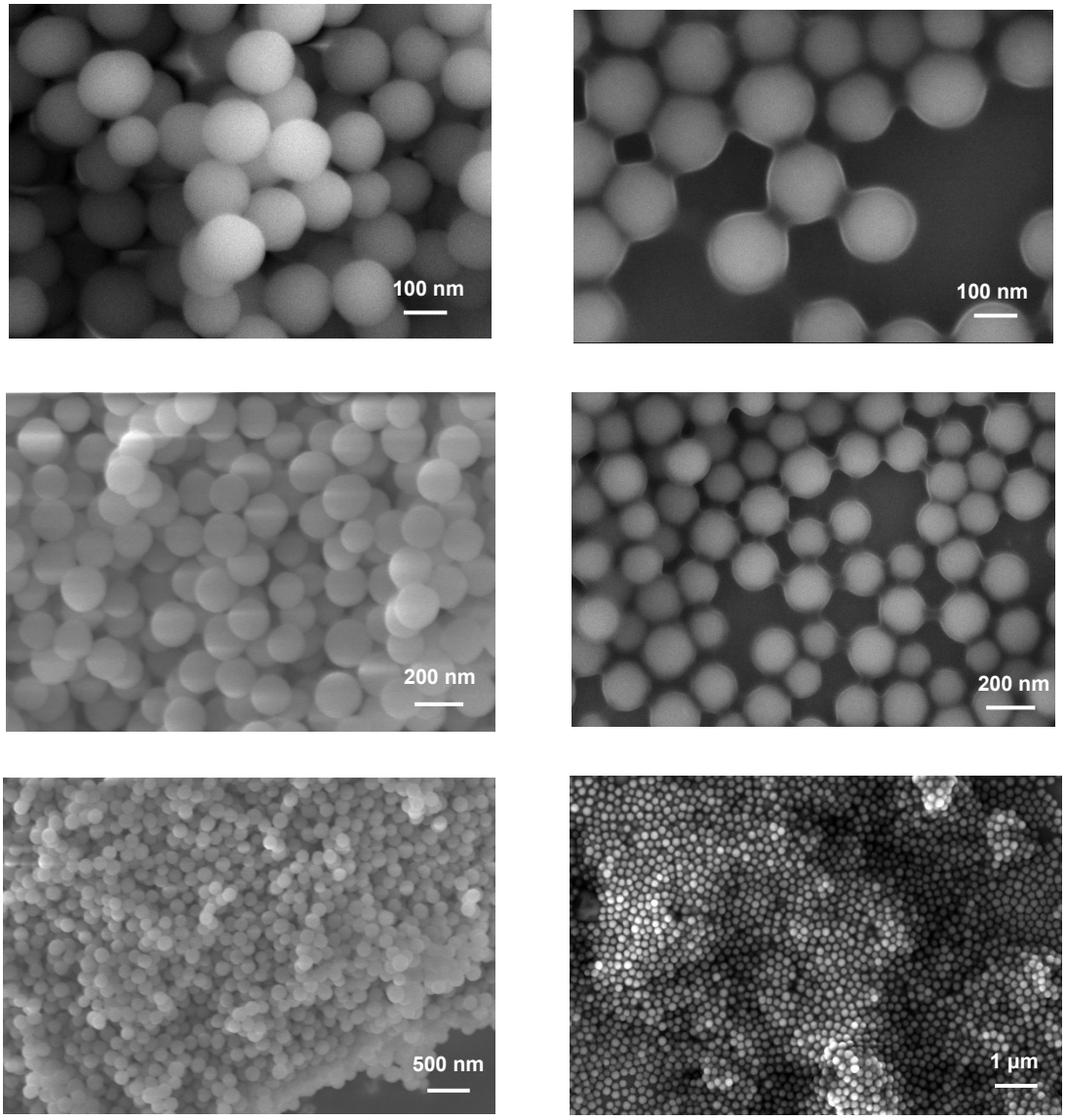

***Figure 4.28**: On the left column the SEM pictures of the 200 nm bare silica particles (before functionalization). On the right column the 200 nm silica particles showing the polymer shell after functionalization.*

TEM pictures of 200 nm particles

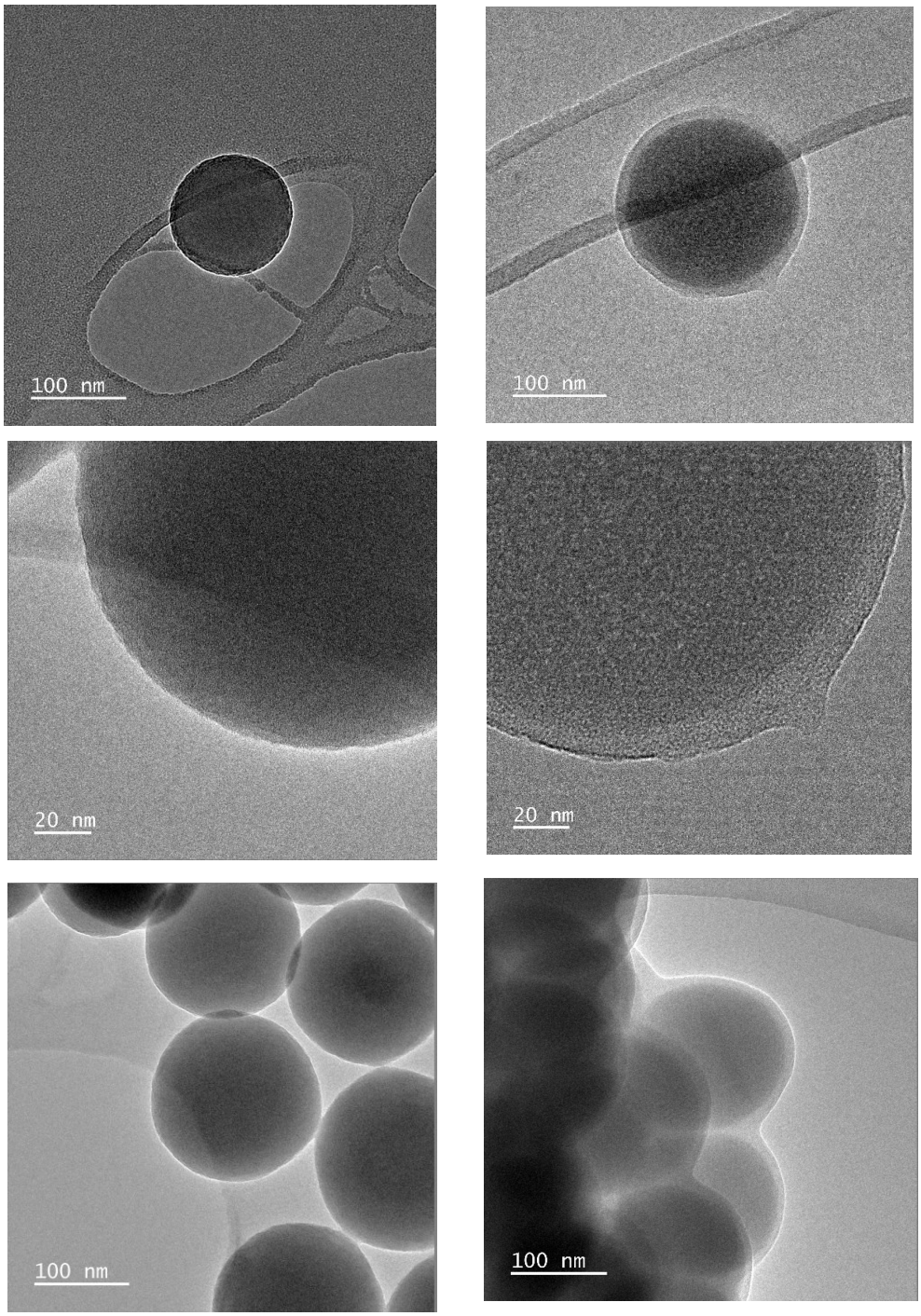

***Figure 4.29**: On the left column the TEM pictures of the 200 nm bare silica particles (before functionalization). On the right column the 200 nm silica particles showing the polymer shell after functionalization.*

STEM pictures of 200 nm particles

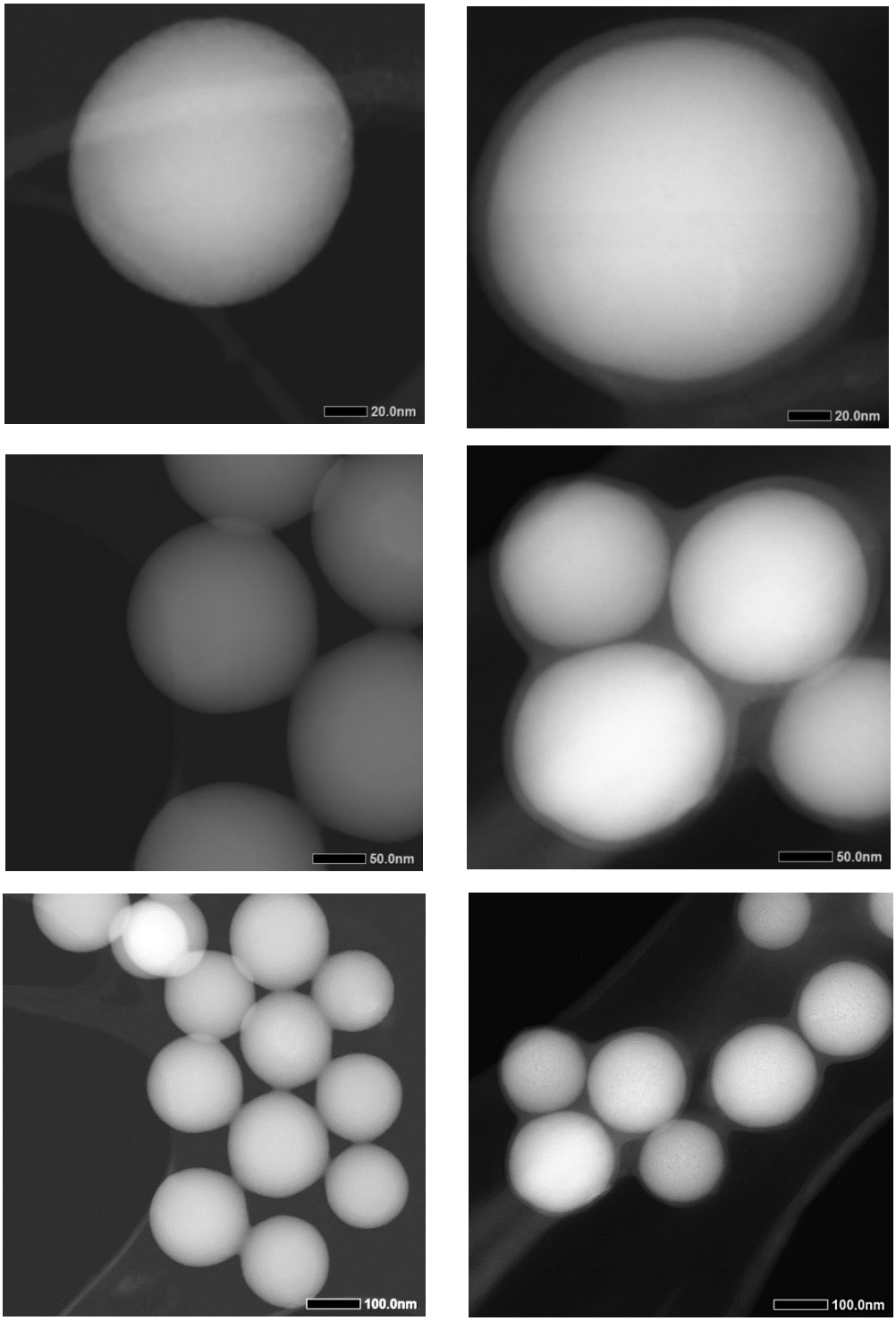

***Figure 4.30**: On the left column the STEM pictures of the 200 nm bare silica particles (before functionalization). On the right column the 200 nm silica particles showing the polymer shell after functionalization.*

References

[1] L. Buglioni, F. Raymenants, A. Slattery, S. D. A. Zondag, T. Noël, *Chemical Reviews* **2022**, *122*, 2752–2906.

[2] B. König, *European Journal of Organic Chemistry* **2017**, *2017*, 1979–1981.

[3] A. B. Beeler, *Chemical Reviews* **2016**, *116*, 9629–9630.

[4] Giacomo Ciamician, *Bull. Soc. Chim. Fr.* **1908**, *3–4*, I–XXVII.

[5] A. Albini, V. Dichiarante, *Photochemical and Photobiological Sciences* **2009**, *8*, 248–254.

[6] Juan M. Coronado, in *Design of Advanced Photocatalytic Materials for Energy and Environmental Applications*, Springer, London, London, **2013**, pp. 1–4.

[7] S. Li, Z. Hao, K. Wang, M. Tong, Y. Yang, H. Jiang, Y. Xiao, F. Zhang, *Chemical Communications* **2020**, *56*, 11243–11246.

[8] Y. Y. Loh, K. Nagao, A. J. Hoover, D. Hesk, N. R. Rivera, S. L. Colletti, I. W. Davies, D. W. C. Macmillan, *Science* **2017**, *358*, 1182–1187.

[9] S. D. Halperin, D. Kwon, M. Holmes, E. L. Regalado, L. C. Campeau, D. A. Dirocco, R. Britton, *Organic Letters* **2015**, *17*, 5200–5203.

[10] H. H. Jaffe, A. L. Miller, *Journal of Chemical Edducation* **1966**, *43*, 469–473.

[11] J. M. Luis, D. M. Bishop, B. Kirtman, *Journal of Chemical Physics* **2004**, *120*, 813–822.

[12] P.A.M. Dirac, in *The Quantum Theory of the Electron*, **1928**, pp. 610–624.

[13] H. D. Roth, *History of photochemistry* **1988**, *32*, 1–20.

[14] H. D. Roth, *Angewandte Chemie International Edition* **1989**, *28*, 1193–1207.

[15] M. Fréneau, N. Hoffmann, *Journal of Photochemistry and Photobiology C: Photochemistry Reviews* **2017**, *33*, 83–108.

[16] J. Zheng, X. Dong, T. P. Yoon, *Organic Letters* **2020**, *22*, 6520–6525.

[17] J. Zhang, X. Liu, R. Blume, A. Zhang, R. Schlögl, S. S. Dang, *Science* **2008**, *322*, 73–77.

[18] C. K. Prier, D. A. Rankic, D. W. C. MacMillan, *Chemical Reviews* **2013**, *113*, 5322–5363.

[19] M. A. Ischay, M. E. Anzovino, J. Du, T. P. Yoon, *Journal of the American Chemical Society* **2008**, *130*, 12886–12887.

[20] J. W. Tucker, C. R. J. Stephenson, *Journal of Organic Chemistry* **2012**, *77*, 1617–1622.

[21] K. Teegardin, J. I. Day, J. Chan, J. Weaver, *Organic Process Research & Development* **2016**, *20*, 1156–1163.

[22] H. Huang, X. Li, C. Yu, Y. Zhang, P. S. Mariano, W. Wang, *Angewandte Chemie* **2017**, *129*, 1522–1527.

[23] Z. Li, H. Song, R. Guo, M. Zuo, C. Hou, S. Sun, X. He, Z. Sun, W. Chu, *Green Chemistry* **2019**, *21*, 3602–3605.

[24] D. A. Nicewicz, T. M. Nguyen, *ACS Catalysis* **2014**, *4*, 355–360.

[25] A. Joshi-Pangu, F. Lévesque, H. G. Roth, S. F. Oliver, L. C. Campeau, D. Nicewicz, D. A. DiRocco, *Journal of Organic Chemistry* **2016**, *81*, 7244–7249.

[26] D. Ravelli, D. Dondi, M. Fagnoni, A. Albini, *Chemical Society Reviews* **2009**, *38*, 1999–2011.

[27] Z. Y. Yu, J. N. Zhao, F. Yang, X. F. Tang, Y. F. Wu, C. F. Ma, B. Song, L. Yun, Q. W. Meng, *RSC Advances* **2020**, *10*, 4825–4831.

[28] M. A. Bryden, E. Zysman-Colman, *Chemical Society Reviews* **2021**, *50*, 7587–7680.

[29] B. P. A M D irac, S. John, *The Quantum Theory o f the Emission and Absorption of Radiation*, **n.d.**

[30] L. Buzzetti, G. E. M. Crisenza, P. Melchiorre, *Angewandte Chemie* **2019**, *131*, 3768–3786.

[31] L. Capaldo, D. Ravelli, *European Journal of Organic Chemistry* **2017**, *2017*, 2056–2071.

[32] F. Juliá, T. Constantin, D. Leonori, *Chemical Reviews* **2022**, *122*, 2292–2352.

[33] F. Strieth-Kalthoff, F. Glorius, *Chem* **2020**, *6*, 1888–1903.

[34] T. Förster, *Annalen der Physik* **1948**, *437*, 55–75.

[35] F. Strieth-Kalthoff, M. J. James, M. Teders, L. Pitzer, F. Glorius, *Chemical Society Reviews* **2018**, *47*, 7190–7202.

[36] W. R. Algar, N. Hildebrandt, S. S. Vogel, I. L. Medintz, *Nature Methods* **2019**, *16*, 815–829.

[37] Y. Zhang, T. S. Lee, J. L. Petersen, C. Milsmann, *Journal of the American Chemical Society* **2018**, *140*, 5934–5947.

[38] T. Bortolato, G. Simionato, M. Vayer, C. Rosso, L. Paoloni, E. M. Benetti, A. Sartorel, D. Lebœuf, L. Dell'Amico, *Journal of the American Chemical Society* **2023**, *145*, 1835–1846.

[39] Y. Zhang, T. S. Lee, J. M. Favale, D. C. Leary, J. L. Petersen, G. D. Scholes, F. N. Castellano, C. Milsmann, *Nature Chemistry* **2020**, *12*, 345–352.

[40] M. Bouzrati-Zerelli, N. Guillaume, F. Goubard, T. T. Bui, S. Villotte, C. Dietlin, F. Morlet-Savary, D. Gigmes, J. P. Fouassier, F. Dumur, J. Lalevée, *New Journal of Chemistry* **2018**, *42*, 8261–8270.

[41] M. A. Bryden, E. Zysman-Colman, *Chemical Society Reviews* **2021**, *50*, 7587–7680.

[42] T. Cardeynaels, M. K. Etherington, S. Paredis, A. S. Batsanov, J. Deckers, K. Stavrou, D. Vanderzande, A. P. Monkman, B. Champagne, W. Maes, *Journal of Materials Chemistry C* **2022**, *10*, 5840–5848.

[43] J. Luo, J. Zhang, *ACS Catalysis* **2016**, *6*, 873–877.

[44] H. Uoyama, K. Goushi, K. Shizu, H. Nomura, C. Adachi, *Nature* **2012**, *492*, 234–238.

[45] J. Mateos, F. Rigodanza, A. Vega-Peñaloza, A. Sartorel, M. Natali, T. Bortolato, G. Pelosi, X. Companyó, M. Bonchio, L. Dell'Amico, *Angewandte Chemie* **2020**, *132*, 1318–1328.

[46] E. Speckmeier, T. G. Fischer, K. Zeitler, *Journal of the American Chemical Society* **2018**, *140*, 15353–15365.

[47] A. Vega-Peñaloza, J. Mateos, X. Companyó, M. Escudero-Casao, L. Dell'Amico, *Angewandte Chemie - International Edition* **2021**, *60*, 1082–1097.

[48] M. Melchionna, P. Fornasiero, *ACS Catalysis* **2020**, *10*, 5493–5501.

[49] Y. Murase, in *Encyclopedia of Polymeric Nanomaterials*, Springer Berlin Heidelberg, Berlin, Heidelberg, **2015**, pp. 1859–1864.

[50] C. W. Pester, H. A. Klok, E. M. Benetti, *Macromolecules* **2023**, *56*, 9915–9938.

[51] D. Y. Joh, A. M. Hucknall, Q. Wei, K. A. Mason, M. L. Lund, C. M. Fontes, R. T. Hill, R. Blair, Z. Zimmers, R. K. Achar, D. Tseng, R. Gordan, M. Freemark, A. Ozcan, A. Chilkoti, *Proceedings of the National Academy of Sciences of the United States of America* **2017**, *114*, E7054–E7062.

[52] E. M. Benetti, N. D. Spencer, *Helvetica Chimica Acta* **2019**, *102*, DOI 10.1002/hlca.201900071.

[53] O. Azzaroni, *Journal of Polymer Science, Part A: Polymer Chemistry* **2012**, *50*, 3225–3258.

[54] W. J. Brittain, S. Minko, *Journal of Polymer Science, Part A: Polymer Chemistry* **2007**, *45*, 3505–3512.

[55] I. Luzinov, D. Julthongpiput, H. Malz, J. Pionteck, V. V. Tsukruk, *Macromolecules* **2000**, *33*, 1043–1048.

[56] J. O. Zoppe, N. C. Ataman, P. Mocny, J. Wang, J. Moraes, H. A. Klok, *Chemical Reviews* **2017**, *117*, 1105–1318.

[57] N. Cheng, A. A. Brown, O. Azzaroni, W. T. S. Huck, *Macromolecules* **2008**, *41*, 6317–6321.

[58] O. Azzaroni, A. A. Brown, W. T. S. Huck, *Angewandte Chemie - International Edition* **2006**, *45*, 1770–1774.

[59] A. Halperin, *Langmuir* **1999**, *15*, 2525–2533.

[60] T. Wu, K. Efimenko, P. Vlěek, V. Šubr, J. Genzer, *Macromolecules* **2003**, *36*, 2448–2453.

[61] T. Wu, K. Efimenko, J. Genzer, *Journal of the American Chemical Society* **2002**, *124*, 9394–9395.

[62] G. Liu, H. Cheng, L. Yan, G. Zhang, *Journal of Physical Chemistry B* **2005**, *109*, 22603–22607.

[63] Z. Ding, C. Chen, Y. Yu, S. de Beer, *Journal of Materials Chemistry B* **2022**, *10*, 2430–2443.

[64] R. Whitfield, N. P. Truong, D. Messmer, K. Parkatzidis, M. Rolland, A. Anastasaki, *Chemical Science* **2019**, *10*, 8724–8734.

[65] S. Edmondson, V. L. Osborne, W. T. S. Huck, *Chemical Society Reviews* **2004**, *33*, 14–22.

[66] N. Corrigan, K. Jung, G. Moad, C. J. Hawker, K. Matyjaszewski, C. Boyer, *Progress in Polymer Science* **2020**, *111*, DOI 10.1016/j.progpolymsci.2020.101311.

[67] S. Perrier, *Macromolecules* **2017**, *50*, 7433–7447.

[68] J. Nicolas, Y. Guillaneuf, C. Lefay, D. Bertin, D. Gigmes, B. Charleux, *Progress in Polymer Science* **2013**, *38*, 63–235.

[69] M. Hartlieb, *Macromolecular Rapid Communications* **2022**, *43*, DOI 10.1002/marc.202100514.

[70] K. Matyjaszewski, *Macromolecules* **2012**, *45*, 4015–4039.

[71] J.-S. Wang, K. Matyjaszewski, *Journal of the American Chemical Society* **1995**, *117*, 5614–5615.

[72] M. Kato, M. Kamigaito, M. Sawamoto, T. Higashimura, *Macromolecules* **1995**, *28*, 1721–1723.

[73] P. Krys, K. Matyjaszewski, *European Polymer Journal* **2017**, *89*, 482–523.

[74] X. Pan, M. Fantin, F. Yuan, K. Matyjaszewski, *Chemical Society Reviews* **2018**, *47*, 5457–5490.

[75] B. Shi, H. Zhang, Y. Liu, J. Wang, P. Zhou, M. Cao, G. Wang, *Macromolecular Rapid Communications* **2019**, *40*, DOI 10.1002/marc.201900547.

[76] P. Krys, Y. Wang, K. Matyjaszewski, S. Harrisson, *Macromolecules* **2016**, *49*, 2977–2984.

[77] D. Konkolewicz, K. Schröder, J. Buback, S. Bernhard, K. Matyjaszewski, *ACS Macro Letters* **2012**, *1*, 1219–1223.

[78] P. Chmielarz, M. Fantin, S. Park, A. A. Isse, A. Gennaro, A. J. D. Magenau, A. Sobkowiak, K. Matyjaszewski, *Progress in Polymer Science* **2017**, *69*, 47–78.

[79] W. Jakubowski, K. Min, K. Matyjaszewski, *Macromolecules* **2006**, *39*, 39–45.

[80] Y. Kwak, K. Matyjaszewski, *Polymer International* **2009**, *58*, 242–247.

[81] K. Min, H. Gao, K. Matyjaszewski, *Macromolecules* **2007**, *40*, 1789–1791.

[82] N. V. Tsarevsky, W. Jakubowski, *Journal of Polymer Science, Part A: Polymer Chemistry* **2011**, *49*, 918–925.

[83] M. Horn, K. Matyjaszewski, *Macromolecules* **2013**, *46*, 3350–3357.

[84] G. Gazzola, I. Filipucci, A. Rossa, K. Matyjaszewski, F. Lorandi, E. M. Benetti, *ACS Macro Letters* **2023**, *12*, 1166–1172.

[85] B. Zhu, S. Edmondson, *Polymer* **2011**, *52*, 2141–2149.

[86] T. Zhang, E. M. Benetti, R. Jordan, *ACS Macro Letters* **2019**, *8*, 145–153.

[87] N. Akkilic, W. M. de Vos, in *Switchable and Responsive Surfaces and Materials for Biomedical Applications*, Elsevier, **2015**, pp. 119–146.

[88] F. Adeli, F. Abbasi, P. Ghandforoushan, H. E. Külahlı, M. Meran, F. Abedi, A. Ghamkhari, S. Afif, *Nano Today* **2023**, *53*, 102010.

[89] E. M. Benetti, E. Reimhult, M. Schroffenegger, N. S. Leitner, G. Morgese, S. N. Ramakrishna, M. Willinger, *ACS Nano* **2020**, *14*, 12708–12718.

[90] M. Krishnamoorthy, S. Hakobyan, M. Ramstedt, J. E. Gautrot, *Chemical Reviews* **2014**, *114*, 10976–11026.

[91] S. Liang, N. M. Neisius, S. Gaan, *Progress in Organic Coatings* **2013**, *76*, 1642–1665.

[92] A. Farrukh, A. Akram, A. Ghaffar, S. Hanif, A. Hamid, H. Duran, B. Yameen, *ACS Applied Materials & Interfaces* **2013**, *5*, 3784–3793.

[93] T. Osako, A. Ohtaka, Y. Uozumi, in *Catalyst Immobilization*, Wiley, **2020**, pp. 325–368.

[94] A. C. Comely, S. E. Gibson (née Thomas), N. J. Hales, *Chemical Communications* **2000**, 305–306.

[95] D. E. Bergbreiter, J. Tian, C. Hongfa, *Chemical Reviews* **2009**, *109*, 530–582.

[96] N. Toshima, M. Ohtaki, T. Teranishi, *Reactive Polymers* **1991**, *15*, 135–145.

[97] K. Hyun, Y. Park, S. Lee, J. Lee, Y. Choi, S. Shin, H. Kim, M. Choi, *Angewandte Chemie International Edition* **2021**, *60*, 12482–12489.

[98] J. Heuer, C. T. J. Ferguson, *Nanoscale* **2022**, *14*, 1646–1652.

[99] R. Liu, S.-C. Cheng, Y. Xiao, K.-C. Chan, K.-M. Tong, C.-C. Ko, *Journal of Catalysis* **2022**, *407*, 206–212.

[100] X. Li, Y. Li, Y. Huang, T. Zhang, Y. Liu, B. Yang, C. He, X. Zhou, J. Zhang, *Green Chemistry* **2017**, *19*, 2925–2930.

[101] W. Li, L. Li, G. Cui, Y. Bai, X. Xiao, Y. Li, L. Yan, *Chemistry – An Asian Journal* **2017**, *12*, 392–396.

[102] J. J. Lessard, G. M. Scheutz, A. B. Korpusik, R. A. Olson, C. A. Figg, B. S. Sumerlin, *Polymer Chemistry* **2021**, *12*, 2205–2209.

[103] C. Boussiron, M. Le Bechec, J. Sabalot, S. Lacombe, M. Save, *Polymer Chemistry* **2021**, *12*, 134–147.

[104] A. B. Korpusik, Y. Tan, J. B. Garrison, W. Tan, B. S. Sumerlin, *Macromolecules* **2021**, *54*, 7354–7363.

[105] W. Wu, B. Liu, *Materials Horizons* **2022**, *9*, 99–111.

[106] C. Yang, R. Li, K. A. I. Zhang, W. Lin, K. Landfester, X. Wang, *Nature Communications* **2020**, *11*, 1239.

[107] W.-J. Yoo, S. Kobayashi, *Green Chem.* **2014**, *16*, 2438–2442.

[108] T. Kuckhoff, R. C. Brewster, C. T. J. Ferguson, A. G. Jarvis, *European Journal of Organic Chemistry* **2023**, *26*, DOI 10.1002/ejoc.202201412.

[109] T. Kuckhoff, J. Heuer, R. Li, K. A. I. Zhang, K. Landfester, C. T. J. Ferguson, *RSC Applied Polymers* **2024**, *2*, 155–162.

[110] B. Hunter, J. L. Sacco, K. Katterle, J. Kirigo, T. K. Wood, E. W. Gomez, C. W. Pester, *European Polymer Journal* **2024**, *213*, DOI 10.1016/j.eurpolymj.2024.113090.

[111] S. Shanmugam, J. Xu, C. Boyer, *Macromolecules* **2016**, *49*, 9345–9357.

[112] C. S. Gill, W. Long, C. W. Jones, *Catalysis Letters* **2009**, *131*, 425–431.

[113] A. P. Schaap, A. L. Thayer, E. C. Blossey, D. C. Neckers, *Journal of the American Chemical Society* **1975**, *97*, 3741–3745.

[114] J. Heuer, T. Kuckhoff, R. Li, K. Landfester, C. T. J. Ferguson, *ACS Applied Materials and Interfaces* **2022**, DOI 10.1021/acsami.2c17607.

[115] L. Kuang, J. Goins, W. Zheng, P. Eduafo, H. Ma, M. Posewitz, D. T. Wu, H. Liang, *Chemistry of Materials* **2019**, *31*, 4657–4672.

[116] K. Bell, S. Freeburne, M. Fromel, H. J. Oh, C. W. Pester, *Journal of Polymer Science* **2021**, *59*, 2844–2853.

[117] R. Li, J. Heuer, T. Kuckhoff, K. Landfester, C. T. J. Ferguson, *Angewandte Chemie - International Edition* **2023**, *62*, DOI 10.1002/anie.202217652.

[118] S. Freeburne, J. L. Sacco, E. W. Gomez, C. W. Pester, *Macromolecular Chemistry and Physics* **2023**, *224*, DOI 10.1002/macp.202300283.

[119] S. Freeburne, C. W. Pester, *Polymer Chemistry* **2024**, DOI 10.1039/d4py00313f.

[120] C. T. J. Ferguson, K. A. I. Zhang, *ACS Catalysis* **2021**, *11*, 9547–9560.

[121] K. Yasukawa, K. Shota;Okinaka, T. Ogiwara, T. Shiomi, *Compound, Material for Organic Electroluminescence Element, Organic Electroluminescence Element, and Electronic Device*, **2022**.

[122] M. H. Aukland, M. Šiaučiulis, A. West, G. J. P. Perry, D. J. Procter, *Nature Catalysis* **2020**, *3*, 163–169.

[123] P. P. Singh, J. Singh, V. Srivastava, *RSC Advances* **2023**, *13*, 10958–10986.

[124] V. Srivastava, P. K. Singh, A. Srivastava, P. P. Singh, *RSC Advances* **2021**, *11*, 14251–14259.

[125] H. Deol, G. Singh, M. Kumar, V. Bhalla, *The Journal of Organic Chemistry* **2020**, *85*, 11080–11093.

[126] J. Zhou, L. Mao, M.-X. Wu, Z. Peng, Y. Yang, M. Zhou, X.-L. Zhao, X. Shi, H.-B. Yang, *Chemical Science* **2022**, *13*, 5252–5260.

[127] S. Lerch, L.-N. Unkel, P. Wienefeld, M. Brasholz, *Synlett* **2014**, *25*, 2673–2680.

[128] T. Bortolato, S. Cuadros, G. Simionato, L. Dell'Amico, *Chemical Communications* **2022**, *58*, 1263–1283.

[129] D. Phillips, R. C. Drake, D. V. O'Connor, R. L. Christensen, *Instrumentation Science & Technology* **1985**, *14*, 267–292.

[130] M. Lawton, R. C. Bolden, M. J. Shaw, *Journal of Physics E: Scientific Instruments* **1976**, *9*, 686–690.

[131] R. Ishimatsu, S. Matsunami, K. Shizu, C. Adachi, K. Nakano, T. Imato, *The Journal of Physical Chemistry A* **2013**, *117*, 5607–5612.

[132] T. Nakagawa, S.-Y. Ku, K.-T. Wong, C. Adachi, *Chemical Communications* **2012**, *48*, 9580.

[133] S. Youn Lee, T. Yasuda, H. Nomura, C. Adachi, *Applied Physics Letters* **2012**, *101*, 093306.

[134] X. Yin, Y. He, X. Wang, Z. Wu, E. Pang, J. Xu, J. Wang, *Frontiers in Chemistry* **2020**, *8*, DOI 10.3389/fchem.2020.00725.

[135] E. Speckmeier, T. G. Fischer, K. Zeitler, *Journal of the American Chemical Society* **2018**, *140*, 15353–15365.

[136] N. Bortolamei, A. A. Isse, V. B. Di Marco, A. Gennaro, K. Matyjaszewski, *Macromolecules* **2010**, *43*, 9257–9267.

[137] E. P. Lyra, C. L. Petzhold, L. M. F. Lona, *Chemical Engineering Journal* **2019**, *364*, 186–200.

[138] N. V. Tsarevsky, T. Pintauer, K. Matyjaszewski, *Macromolecules* **2004**, *37*, 9768–9778.

[139] M. Fantin, A. A. Isse, A. Gennaro, K. Matyjaszewski, *Macromolecules* **2015**, *48*, 6862–6875.

[140] Q. Wei, P. Kleine, Y. Karpov, X. Qiu, H. Komber, K. Sahre, A. Kiriy, R. Lygaitis, S. Lenk, S. Reineke, B. Voit, *Advanced Functional Materials* **2017**, *27*, DOI 10.1002/adfm.201605051.

[141] A. Vega-Peñaloza, J. Mateos, X. Companyó, M. Escudero-Casao, L. Dell'Amico, *Angewandte Chemie International Edition* **2021**, *60*, 1082–1097.

[142] H. M. Ko, C. W. Lee, M. S. Kwon, *ChemCatChem* **2023**, *15*, DOI 10.1002/cctc.202300661.

[143] S. Grotjahn, B. König, *Organic Letters* **2021**, *23*, 3146–3150.

[144] K. Donabauer, M. Maity, A. L. Berger, G. S. Huff, S. Crespi, B. König, *Chemical Science* **2019**, *10*, 5162–5166.

[145] W. Jakubowski, K. Min, K. Matyjaszewski, *Macromolecules* **2006**, *39*, 39–45.

[146] S. Hansson, E. Östmark, A. Carlmark, E. Malmström, *ACS Applied Materials and Interfaces* **2009**, *1*, 2651–2659.

[147] J. J. Keating, A. Lee, G. Belfort, *Macromolecules* **2017**, *50*, 7930–7939.

[148] P. Pavan, F. Lorandi, F. De Bon, A. Gennaro, A. A. Isse, *ChemElectroChem* **2021**, *8*, 2450–2458.